THE UNIVERSITY OF CHICAGO

PROPERTIES AND DYNAMICS OF DRIVEN OPTICAL MATTER

A DISSERTATION SUBMITTED TO
THE FACULTY OF THE DIVISION OF THE PHYSICAL SCIENCES
IN CANDIDACY FOR THE DEGREE OF
DOCTOR OF PHILOSOPHY

DEPARTMENT OF CHEMISTRY

BY
PATRICK EDWARD POPPE FIGLIOZZI

CHICAGO, ILLINOIS
AUGUST 2017

TABLE OF CONTENTS

LIST OF FIGURES

LIST OF TABLES

ACKNOWLEDGMENTS

I have spent pretty much my entire life as a student up until this point. This thesis represents a culmination of all the knowledge, skills, and experiences I have gained up so far. By no means did I complete this degree without the help of teachers, mentors, friends, and loved ones. I would like to acknowledge just a fraction of the people who supported me.

First and foremost I would like to thank my advisor Norbert Scherer who has been a great mentor during the course of my career as a graduate student here at University of Chicago. Norbert is by far the smartest person I have had the pleasure of working with and he has a propensity of thinking of new perspectives about any research project or experiment. Norbert's mentor-ship has lead me to not only think critically about scientific problems but also gave me the opportunity to explore avenues of research direction that are not directly related to the projects at hand. I am grateful that Norbert's style of mentor-ship is not rooted in forcing research projects in a specific direction which has allowed me to learn new skills and develop new approaches to solve scientific problems. I appreciate the patience Norbert has for allowing me to spend the time to do experiments and analysis in as rigorous way as possible. Under Norbert's guidance, the research, analysis, and science that I was able to complete during my dissertation was beyond my expectations for myself.

I want to acknowledge other University of Chicago faculty that have guided me through my chemistry Ph.D. Stuart Rice has offered thoughtful insight into how to model the plethora of experiments that I presented at our subgroup meetings over the past 7 years. I also have the pleasure of having Stuart Rice on my dissertation committee and I am thankful that he can see the culmination of my research that he helped me achieve. Suriyanarayanan Vaikuntanathan has also been a very valuable collaborator also offering theoretical insights of how to model my experiments and I am very glad that he is also able to participate on my dissertation committee.

Of course the is a plethora of other scientists, graduate students, and post-docs that have taught me so much through collaboration during the course of my Ph.D. There is number

of former labmates that I want to acknowledge for helping me become a better scientist and counseled me during the time we overlapped sharing the lab. In lab my first two years, Yihan Lin was my lifeline that I would always ask for help from and while he wouldn't often show his sense of humor, he was actually very funny. Thomas Spears always helped me with a physics or laser question and I always admired his passion for science. Zsolt Terdik was the one who taught me "hello world" and led me down the path of learning how to program which, as he would say, "saves you boatloads of time." Working with Ye Tian was always a joy and I very much enjoyed her company when I would make trips to Minnesota. I am very indebted to Justin Jureller who taught me how to align a laser and had a knack for finding any piece of equipment in the lab. The incredibly gifted Toan Huynh taught me photo lithography and how to design good experiments but remains the friend that I have enjoyed the most spicy Harold's chicken with. Mattie Renn taught me all the biology I know and I enjoyed working with her to perpetuate the Hassan Poorjasem lab meme. I very much enjoyed having Charlie Wright as an office-mate who I talked with about science, grad school, or life and enjoyed the the few times we were able to escape and hang out outside of lab. Klevin Lo had the misfortune of being on the butt end of our lab banter but was always a good sport about it and now gets to brag about making millions as investment banker. The board game addict Matthew Daddysman really pulled the group together for his (almost) monthly board games nights but also remains as one of my good friends in grad school whom I will remember enjoying Harold's chicken and infinite sushi with probably more often than what is considered "healthy." The world's most productive post-doc (now professor), Zijie Yan, constructed the foundation of the research in this thesis and was extremely helpful in getting started on performing experiments with optically trapped nanoparticles. Raman Shah remains to be one of my good friends who I always enjoyed talking with about science, grad school, hobbies and life and I appreciated him organizing trips to go "deagle-ing" at the gun range especially after a quarter of TAing experimental p-chem. The experimental work in this thesis wouldn't have gone anywhere without the collaboration of Nishant Sule who on

his own accord decided to use his ED-LD method to simulate my experiments which allowed us to create a much more complete story of the driven optical matter systems. I appreciate the collaboration of Stas Burov who had a theory for any experiment and was able to turn our failures from investigating lubrication forces to the success of the correcting particle tracking errors. I enjoyed sharing an office with Srividya Iyer-Biswas who find creative ways to boost moral by organizing events outside of lab. I also want to thank Yuval Yifat, Nolan Shepherd, Curtis Peterson, Alan Selewa, Tom Kuntz, Delphine Coursault, Uttam Manna for supporting me in science and providing and intellectually stimulating and happy environment to work in.

I wouldn't have made it through this program without the support of friends I have made at University of Chicago, from college, and from home. Dmitriy Dolzhnikov, John Savage, Erik Hoy, Andrew Sand, and Wayne Lau for being officemates, study buddies, and friends from the extra large Chemistry grad student class of 2010. I remember fondly the days spent in the large "office" in the bottom of Kent Laboratory working on impossible problem sets, however, I remember even more fondly the times we were not. I am very grateful to become friends with Zack Hund who helped motivate me to succeed during my first couple years of grad school and I always admire his tenacity and his laser focus that he has on his goals in life; Zack, you are one of my best friends in Chicago and I am proud to have mentored you into the world of craft beer. I had the pleasure of living with one of my other best friends, Patrick O'Kane, for most of my grad school career; Patrick is one of the nicest people I know and I always enjoyed his company at every beer festival, every music festival, or just drinking whiskey and watching Rick and Morty. Alexei Ten is my beer release friend and enjoyed traveling around Chicago to collect and try all the rare beers no matter rain, sleet, or snow (mostly rain though). I am happy that I got to pilot the happy hour beer cart for two years with Charles "200 lbs of pure muscle" Heffern and I enjoyed discovering all the tasty craft beers with him. I am pleased to have become friends with Chef Grant Langlois and Traci Beilharz who would make delicious food for Sara and I to enjoy. Andrew Valentine, Chris

Hansen, Matt Kurley, Lindsey Szymczak, Stephen Pearson, Nicole James, EW Malachowsky, Christine Simmons, and Lendi Hubbard for being great friends that I met in Chicago and remain great friends of mine.

Of course I would not be here without the love and support from my family. My stepmother, Terri Hitt, has always cared for me like I was her own child and I really appreciate her support. I very lucky to have the support of my younger sister Jenn who I am very proud of her accomplishments during my time here in Chicago. To Mom and Dad, thank you for your unwavering support and giving me every opportunity to succeed in school, in health, and in life. I can never repay the sacrifices they have made to raise and support me.

Finally, I want to thank my girlfriend Sara Gehrdes. Meeting you has given me so much joy in my life. I grateful for the support you have given me when I am sad, angry, or sick. You always believed in me no matter how difficult things may seem and I love you with all of my heart.

ABSTRACT

To date investigations of the dynamics of driven colloidal systems have focused on hydrodynamic interactions and often employ optical (laser) tweezers for manipulation. However, the optical fields that provide confinement and drive also result in electrodynamic interactions that are generally neglected. We address this issue with a detailed study of 150-nm Ag nanoparticles electrodynamically interacting in an optical ring vortex trap using 150-nm diameter Ag nanoparticles. We term the resultant electrodynamically interacting nanoparticles a driven optical matter system. First, the instrument used to create driven optical matter is described with special attention to optimizing the components that create the optical ring vortex. Next, we explore a systematic study of the electrodynamical interactions of driven optical matter using experimental and simulation methods We determined the nature of optical ring vortex gives rise to increased fluctuations of interparticle separation that should not be neglected in any optically driven colloidal system. Then, we use driven optical matter to test various kinetic models in a non-equilibrium barrier crossing experiment. We show that one can easily misinterpret dynamics from barrier crossing models through experiment and simulation where no barrier is present. Afterwards, barrier crossing in driven optical matter is explored in a system where the barrier is not fixed at one location but moves with the particles. This "particle passing" process also involves a 2-dimensional reaction coordinate that modulates as a pair of particles is driven around the optical ring vortex. Finally, localization errors that result from particle tracking are explored and a new method for correcting those errors, the SPIFF algorithm, is presented.

CHAPTER 1

INTRODUCTION

Chemistry is the study of the composition, structure, and properties of matter [1]. There are many aspects of studying matter such as studying the structure of matter using spectroscopic techniques [2–5], determining how to combine matter in specific ways to create new matter such as in organic synthesis [6, 7], or examine the physical properties of matter [8]. The properties of matter are governed by the atoms and molecules that it is constructed from, and while techniques exist such as Scanning Tunneling Microscopy (STM) [9] or Atomic Force Microscopy (AFM) [10] that visualize the arrangement of atoms or molecules these techniques are not fast enough to capture the movement of matter on the smallest scale. In fact established theories [11] in chemical kinetics model the motion and interactions of these atoms without ever actually being able to visualize the reactions that are taking place. A common theoretical technique to model the motion of molecules is to use molecular dynamics (MD) [12] to simulate the movement of the molecules at the molecular scale. However, limitations on computer power prevent simulating many interacting molecules and might require making approximations such as coarse graining molecular interactions [13, 14] or imparting artificial potentials [15–17] to guide molecular motion in order to study the phenomena of interest. Indeed, being able to visualize molecules interacting would allow us to give experimental validation to simulations and modeling.

While being able to visualize the movement of molecules in matter has not be fully realized experimentally, one can imagine constructing a model system that is serves as an analog of a molecular system that can be visualized in order to test various theories of molecular dynamics and reactivity. Ideally, this model system would contain components that are large enough to see with faster sampling techniques but would still retain the properties of molecules such as thermal motion and intermolecular interactions. Optical matter [18, 19] is a model system that possess properties that are akin to those seen in atoms/molecules but the constituents of optical matter can be visualized using conventional

optical microscopy methods. Optical matter is a structure of small particles (microscale particles) interacting in the presence of a strong electromagnetic field. This thesis presents several studies of the properties of optical matter and the creation of optical matter models of driven nonequilibrium systems through the use of exotic electromagnetic fields. In particular, driven optical matter is used to validate molecular kinetic models of barrier crossing process under nonequilibrium conditions.

1.1 Optical Matter

Optical matter is created from a combination of optical trapping and optical binding between microscopic particles. Optical trapping is a technique where a focused laser is used to manipulate microscopic particles by exploiting the momentum property of light (electromagnetic radiation) [20, 21]. The concept of a photon, *i.e.* a single packet of electromagnetic radiation, was discovered gradually in the early 20th century by Albert Einstein and Max Planck. Einstein showed in 1909 [22] and 1916 [23] that the energy quanta of electromagnetic radiation must also carry momentum, $p = h/\lambda$, where h is Planck's constant and λ is the wavelength of light. In 1923 the momentum property of light was first observed by Compton [24] examining the change in the wavelength of X-rays due to imparting momentum on an electron. Normally the momentum in a photon is too small to affect large objects; however, it was discovered in 1970 that that the momentum from light could be transferred to microscopic dielectric particles by using a focused Gaussian laser beam [20, 25]. To successfully trap particles in 3D two optical forces need to be balanced, the scattering force and the gradient force (Figure 1.1a). The scattering force arises from photons that are scattered or absorbed by the dielectric particle and applies a force pushing the particle in the direction of the electric field. In the ray-optics description of the gradient force, photons that refract through the dielectric particle impart the change of the photon momentum on the dielectric particle in the direction of the highest intensity of the laser light (Figure 1.1b). This ray-optics description works well to describe the forces acting on a dielectric particle larger than

the wavelength of laser light and it was often thought for a long time that metallic particles could not be optically trapped due to the scattering force would overpower the non-existent gradient force.

However, it has been shown that metal nanoparticles much smaller than the wavelength of light are able to be optically trapped as well [26]. While the scattering force remains large for metal nanoparticles the nature of the gradient force is different than the ray optics description because light cannot pass through a metal nanoparticle at the wavelengths used for trapping. For light incident on a metal particle the gradient force is characterized as, $F_{\text{grad}}(\boldsymbol{r}) = \frac{1}{2\epsilon_0} Re\{\alpha\} \nabla I(\boldsymbol{r})$ where ϵ_0 is the vacuum permittivity, α is the polarizability of the material, $I(\boldsymbol{r})$ is the intensity of the electric field at position $\boldsymbol{r}$ [27]. The repulsive optical force comes from both scattering and absorption of light off the metal nanoparticle and is defined as $F_{\text{rp}}(\boldsymbol{r}) = \frac{n_{\text{m}}}{c} \sigma_{\text{ext}} \langle S(\boldsymbol{r}) \rangle$ where n_{m} is the refractive index of the metal, c is the speed of light in a vacuum, σ_{ext} is the particle extinction cross section $\sigma_{\text{ext}} = \sigma_{\text{abs}} + \sigma_{\text{scat}}$, and $S(\boldsymbol{r})$ is the Poynting vector of the incident light [27]. When these forces are balanced then the metallic particle is trapped in the laser light.

Optical trapping is not just limited to using Gaussian shaped traps. Other beam shapes (*e.g.* Bessel beams, vortex beams, ring traps, etc.) are readily produced using active or passive optical devices [28]. For example, diffractive optical elements (DOE) can be used to trap particles with different shaped electromagnetic fields [29–35]. The simplest DOE is a transmission diffraction grating that will produce (at least) 3 unique beams. In general, DOEs are constructed from a flat piece of glass and using lithography to etch a custom pattern into the glass [29]. When light passes through the DOE the phase of the light will be altered according to the pattern etched into the surface, *i.e.* light that travels through the parts of the glass that have been etched will have a shorter path length and different phase than light that travels through glass that is not etched [36]. The pattern etched into the glass surface and the etching depth will have an affect on the light field traveling through the DOE and the spatial phase change of the light after the DOE. When the etching depth

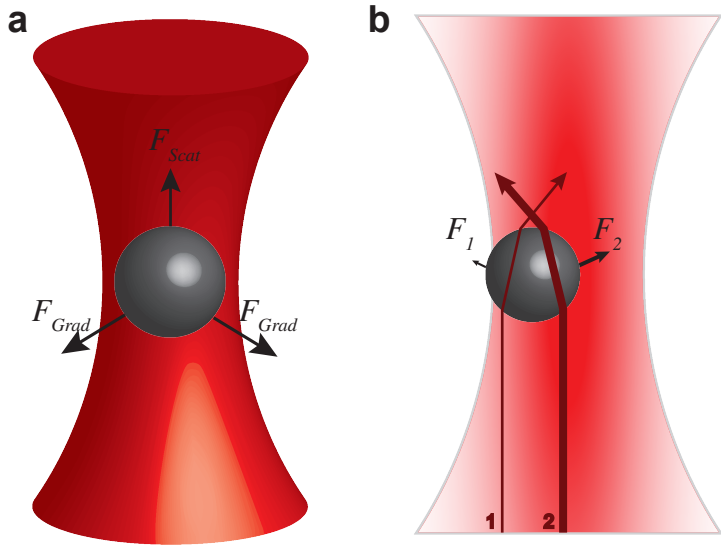

Figure 1.1: (a) Schematic of optically trapping a particle with a laser showing the competing forces acting on the particle. The scattering force F_{Scat} aligned with the laser propagation is balanced by the gradient forces F_{Grad} pulling the particle towards the center of the beam waist. (b) A diagram that shows how the gradient forces arise in a dielectric trapped particle. The refraction of light of lower intensity (red arrow marked 1) applies a smaller force (F_1) due to the change of its momentum compared to the larger intensity light (red arrow marked 2) which applies a larger force (F_2) towards the high intensity region in the beam.

is 0.5λ then the portion of an optical beam going through the etched parts of the DOE will be completely out of phase compared the rest of the beam. Etching glass is not the only way to create a DOE. Liquid crystals have been shown to change the phase of light based on their orientation with respect to the incident field [37]. Arrays of liquid crystal cells (similar to a liquid crystal display) have been used to create devices, known as spatial light modulators (SLM), where the liquid crystal in each pixel of the array can be tuned to change the phase of light between 0 and 2π arbitrarily [38]. Because the liquid crystals in a SLM control the phase of light between 0 and 2π in each pixel, they can be used not only for producing diffraction patterns from two π-shifted phase profiles (*i.e.* a binary phase pattern or mask), but can also apply smoothly varying spatial phase functions on the incident field. In this way, a SLM can change the phase profile of a laser that are not easily producible on an etched DOE (*i.e.* etching produces discrete phase shifts). Slowly varying spatial phase gradients have been used in creating all kinds of exotic optical traps such as optical line

traps, optical line barriers, and optical vortices [39].

One of the consequences of optically trapping objects with spatially coherent laser light is that electromagnetic (EM) radiation is scattered in all different directions after hitting the object. This scattered EM field has the same wavelength as the incident EM field but due to the different paths of scattered light versus the incident light, the EM field scattered off a particle would have a different phase than the incident EM field. As expected, the scattered light field and incident light fields interfere to shape the electromagnetic radiation around each particle. The shaping of the EM radiation of the incident and scattered fields around a trapped particle leads to "optical binding" [18, 40, 41], *i.e.* the creation of potential energy wells around particles due to the interference of the incident and scattered fields. "Optical binding" was first discovered in 1989 by Burns *et. al.* [40] who found that dielectric particles will arrange themselves in an optical trap with separations of roughly integral multiples of the wavelength of the incident optical field. The strength and orientation of optical binding depends on the polarization and the wavelength of the trapping field. Particles will optically bind to one another at distances of roughly one wavelength where binding sites perpendicular to the polarization of the incident field have stronger binding than sites parallel to the incident field. The electrodynamic interactions between a pair of metal particles in an optical trap can be calculated from Maxwell's equations using the finite-difference time-domain (FDTD) method [42]. Figure 1.2 shows the potential energy surface of a second 150 nm Ag nanoparticle near a Ag nanoparticle located at the origin when illuminated with an 800 nm plane wave. The strongest electrodynamic interaction for a pair of Ag nanoparticles is the near-field interaction aligned in the direction of the polarization at $\sim$150 nm separation (-150 nm and $+150$ nm in the x direction in Figure 1.2). However, the optical binding interaction (a far-field electrodynamic interaction) can be seen in Figure 1.2 at ± 600 nm in y while weaker optical binding sites are at ± 600 nm in x.

Later in 1990, Burns coined the term "optical matter" [18] to describe several particles in an optical trap that interact through optical binding. The strength of optical binding

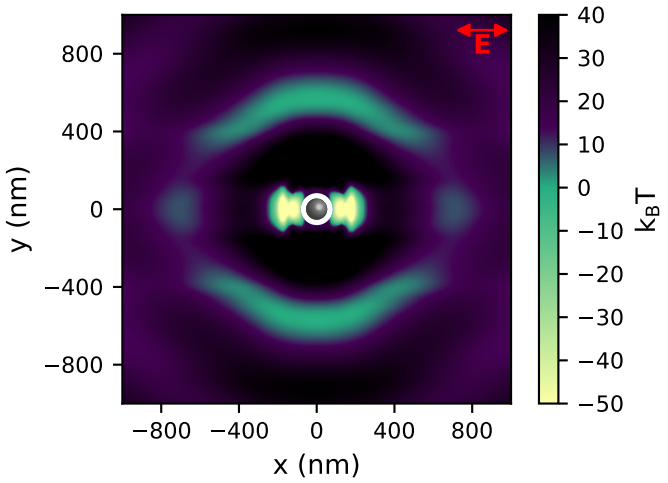

Figure 1.2: The potential energy of a second 150 nm Ag metal nanoparticle near a metal particle at the origin calculated from Maxwell's equations. The particle at the origin is trapped with 800 nm light with a surrounding medium of water. The polarization of the electromagnetic field incident on the metal nanoparticle is horizontal in the image.

amplifies when there are more particles in succeeding binding locations which causes the movement of one bound particle to affect all other particles bound to it [19]. Optical matter created from metal nanoparticles have the strongest optical binding interactions because of the large scattering cross-sections and hence scattering of the trapping electromagnetic field [43]. "Optical matter" composed of optically bound metal particles behave very similar to atoms/molecules as they can form different structures in the light field [44] or they can "react" to form new structures based on initial conditions and the type of electric field used [45]. However, the research done on optical matter thus far has mostly been of static structures, *i.e.* looking at the structure of optical matter in different EM fields, and not how optical matter moves in driven EM fields. In Chapter 3 we will examine the properties of optical matter being driven in a shaped EM field while in Chapter 4 and 5 we examine kinetics of barrier crossing processes in driven optical matter systems.

1.2 Kinetics

The kinetics of barrier crossing phenomena are of fundamental importance in Physics, Chemistry, and Biology [46–54]. Studies of barrier crossing in Chemistry typically obtain the rate at which molecules react to form products by surmounting an activation energy (or free energy) barrier. The Arrhenius equation, $k = Ae^{-E_a/(RT)}$, first proposed by Svante Arrhenius in 1889, was used to model the rate of reactions and determine size of the energy barrier the reactants must cross to form products [11]. However, the Arrhenius equation does not account for reactions where reactive intermediates are involved in the kinetics of converting a reactant to a product [55]. Additionally, the physical meaning of the two parameters in the Arrhenius equation, namely the pre-exponential factor (A) and the activation energy (E_a), were not understood since it was derived as an empirical model. The development of statistical thermodynamics and the concept of the potential energy surface spurred the creation of Transition state theory (TST) [56–58]. TST treats a chemical reaction as a process that surmounts a potential energy barrier where the transition state at the barrier top separates reactants from products. The transition state is in a quasi-equilibrium with the molecules on the reactants side of the energy landscape. The Eyring-Polanyi equation [56, 57], $k = \frac{k_B T}{h} e^{-\frac{\Delta G^\ddagger}{RT}}$ is a statistical thermodynamic result derived from TST that relates free energy of activation, $\Delta G^\ddagger$, the statistical movement of the molecules in $\frac{k_B}{h}$ where h is Planck's constant. Transition state theory describes barrier crossing dynamics in the gas phase for frictionless conditions, while Kramers theory is appropriate in frictionally damped environments such as solution [48, 59, 60]. In Kramers theory a parabolic barrier is crossed in a diffusive manner in a canonical ensemble (at equilibrium) where the barrier height $>k_B T$. Kramers theory has been extended to describe the kinetics of barrier crossing when a force or load is applied by changing the equilibrium potential energy landscape with an increasing tilt towards the products which represents the applied force [61]. This extension of Kramers theory provides a relationship between the applied force on a molecule and its rate of mechanical rupture [54, 62]. However, Kramers theory is strictly an equilibrium description

of barrier crossing so caution should be used when extending Kramers theory to included nonequilibrium conditions. We explore several nonequilibrium optical matter systems and discuss the complications of modeling nonequilibrium systems using theories extended from equilibrium ideas in Chapter 4 and 5.

1.3 Particle Tracking Methods

Tracking the dynamics of and positions in particles is necessary for research in physics and biology. For example, metal nanoparticles have been used to tag and track transport of microtubules [63, 64], and microparticles (from 0.1 µm–2 µm diameter) have been used to probe the strength and range of hydrodynamic interactions [65–68]. In these examples many and other applications, accurate tracking of spherical or circularly shaped features in microscopy data was an important aspect of the research. Methods have been developed to precisely locate the center of circular features in a digitized image with sub-pixel accuracy. Typically these methods are executed as part of a software package that analyzes each frame of the digital image. Some of this software comes in a commercial package like Imaris or Diatrack [69] while open source packages (*e.g.* incorporated in ImageJ [70]) exist that use the most popular particle tracking algorithms [71–73]. The most accurate method of localizing the particle's center in a digitized image is to fit each feature with a Gaussian using a nonlinear least-squares algorithm [74]. However, this method is quite slow as it requires numerical iteration on each particle in the frame to determine the optimal parameters. Faster localization methods are often preferred especially if real time tracking is necessary for the experiment. By far the most popular method of particle tracking is the method first proposed by Crocker and Grier (CG) in 1996 [71]. The CG method is so widely used because it is very fast and only requires calculating the center of each particle using the weighted intensities of the pixels that make up each particle (*i.e.* its center of mass). While the CG method works adequately for images with good signal to noise and well defined particles, it performs poorly when particles become very small ($\sim$1–2 pixels in diameter) or multiple particles are

in close proximity causing a decrease in the subpixel accuracy. In Chapter 6 we explore several sources of error in subpixel localization using the CG method as a prototype method of particle tracking and offer a method to correct the so called "pixel-locking" [75, 76] errors in particle tracking.

1.4 Structure of Dissertation

This thesis covers two general topics of research, the study of the dynamics of driven optical matter and the development of new methods for correcting errors in particle tracking. Chapter 2 details the experimental methods performed for this work, including the construction of the optical trapping instrument used in the experiments and the preparation of samples for optical trapping experiments. Chapter 3 presents a systematic study of the properties of driven optical matter by experimental and simulated methods. Chapter 4 examines the kinetics of driven optical matter crossing a stationary electromagnetic barrier. An in-depth look at nonequilibrium barrier crossing kinetics are tested using driven optical matter crossing the EM barrier. In Chapter 5, driven optical matter is used to explore barrier crossing kinetics where the barrier is not fixed at one location but moves with the particles. This "particle passing" process also involves a 2-dimensional reaction coordinate *vs* the 1-D system of Chapter 4. Finally, in Chapter 6, localization errors that result from particle tracking are explored and a new method for correcting those errors, the SPIFF algorithm, is presented.

CHAPTER 2

EXPERIMENTAL METHODS

2.1 Optical Trapping Instrument

A home built Titanium-doped sapphire (Ti:S) laser reflected from a SLM and directed into and focused by a microscope was used to trap the Ag nanoparticles as shown in Figure 2.1. 3.4 W of power from a continuous wave laser (Spectra Physics Millennia 523 nm) was used to pump either a home-built or commercial Ti:S laser [77]. A $\lambda/2$ waveplate was used to align the polarization of the pump laser to be perpendicular to the laser table. As shown in Figure 2.2 the 532 nm beam was focused with a $f = 5$ in focal length lens onto the Ti:S crystal (Crystal Systems, 2.6 mm path length, absorbance = $5\,\mathrm{cm}^{-1}$, Brewster cut). The crystal was cooled to 9 °C using water circulated through a home-built copper mount that was clamped onto the Ti:S crystal from the top and bottom to allow uniform cooling the crystal from both sides. The Ti:S crystal and mount was connected to a 3-axis translation stage with a single axis rotation stage that allowed rotation of the crystal in the plane of incidence. Laser excitation of the Ti:S crystal was collected by the concave mirrors CM_1 and CM_2 that have broad reflectivity for the red fluorescence of the Ti:S crystal ($\geq$99.9% for wavelengths 650 nm–1020 nm) and high transmission ($\sim$98%) at the pump wavelength. The curved mirrors CM_1 and CM_2 were placed one radius of curvature from the Ti:S crystal (radius of curvature=5 cm) and are angled to direct fluorescence to the high-reflector and output coupler (HR and OC, respectively in Figure 2.2) Both the HR and the OC are flat dielectric mirrors, with the OC transmitting 5% at 800 nm wavelength. A birefringent tuning element (BT) was inserted at Brewster's angle after alignment of the laser cavity. The angle of the BT in the plane perpendicular to the laser table was manipulated allowing the laser wavelength to be tuned from 740 nm to 840 nm. The laser cavity output power was $\sim$400 mW at the desired wavelength of 800 nm.

The home built Ti:S laser was used for trapping in the optical trapping instrument

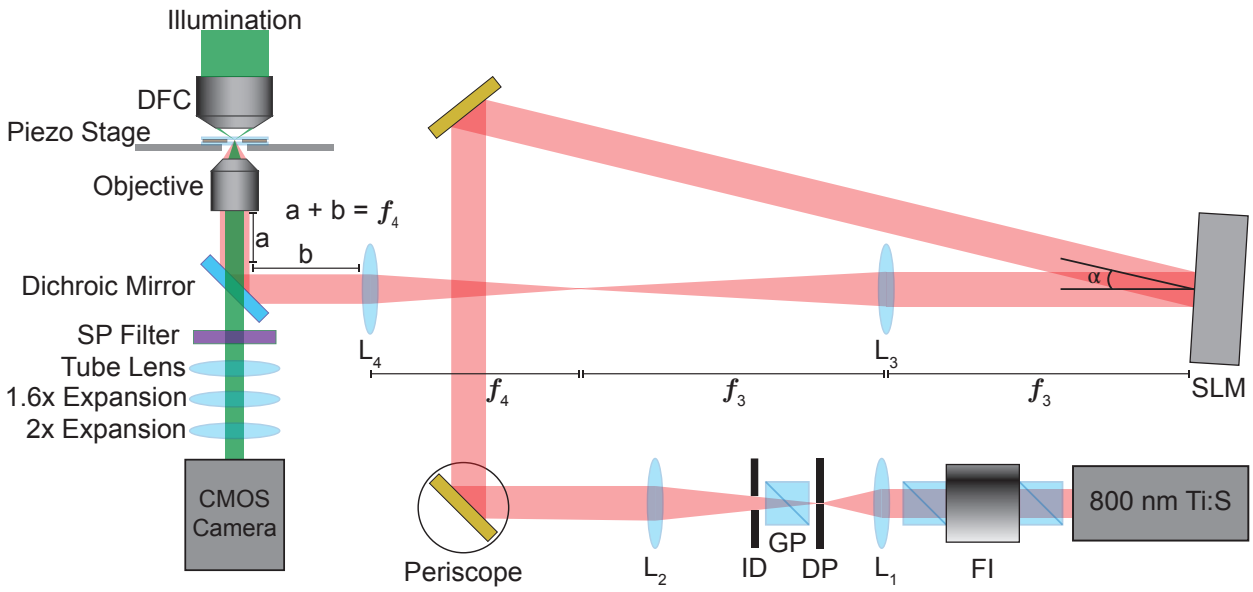

Figure 2.1: Schematic of the optical trapping instrument. Abbreviations are Faraday isolator FI, lens L, diamond pinhole DP, Glan-laser polarizer GP, iris diaphragm ID, spatial light modulator SLM, short pass SP, dark field condenser DFC. The angle of incidence of the laser beam on the SLM is $\alpha < 3°$.

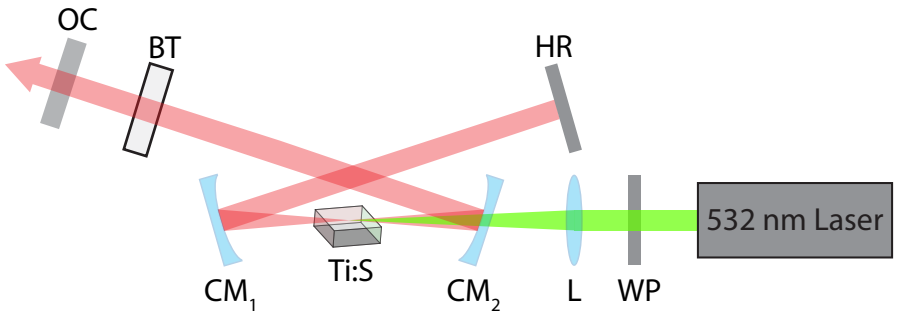

Figure 2.2: Schematic of the laser cavity of the home-built titanium-doped sapphire (Ti:S) laser. Abbreviations are $\lambda/2$ waveplate WP, lens L, curved mirror CM, titanium-doped sapphire crystal Ti:S, high reflector HR, birefringent tuning element BT, and output coupler OC.

depicted in Figure 2.1. The 800 nm Ti:S laser was directed through a Faraday isolator (FI) before it was cleaned up with a home built spatial filter. A 15 cm lens (L_1) focused the beam through a 50 µm diamond pinhole (DP). The resulting TEM_{00} beam passes through a Glan-laser (GP) polarizer to make the polarization perpendicular to the optical table. An iris diaphragm (ID) was placed after the Glan-laser polarizer to block the Airy (diffraction) rings surrounding the desired TEM_{00} portion of the beam. Finally, a 40 cm lens (L_2) was used to collimated the laser light. A periscope, directing the laser up and then right, setting the beam at the height of the back port of the microscope (Olympus, IX71) and changed the polarization of the beam from perpendicular to parallel to the optical table. A turning mirror was used to steer the beam towards the spatial light modulator (SLM, Hamamatsu X10468-02). The angle of the beam incident on the SLM was very small, $< 3°$, in order to provide good phase modulation of the beam. The SLM was also oriented so the long axis of the rectangular window was parallel to the optical table providing optimal phase modulation of the parallel polarized incident beam. After the SLM, a $4f$ lens system was used to relay the phase modulated beam from the SLM surface to the back aperture of a 60x water immersion objective (Olympus, UPlanSApo NA 1.2). Two 2 inch diameter lenses, a 75 cm (L_3) and a 50 cm (L_4), were spaced to make a $4f$ telescope where L_4 was 50 cm from the back aperture of the objective accounting for the distance traveled between two turning mirrors and a dichroic mirror.

The laser light, focused by the objective, was used to trap Ag nanoparticles in a sample chamber secured on a piezo stage (Physik Instrumente, E-710.P3D). Ag nanoparticles were visualized in the in the trap via scattered light from a dark field condenser (DFC, 1.2–1.4 NA). Laser light war filtered from the illumination (Schott, Ace I 20500) light through a 720 nm short-pass filter placed before the tube lens and a series of (two) expansion lenses. Videos of the particle motion were captured with an CMOS camera (Andor, Neo sCMOS DC-152Q-C00-FI) at frame rates of 80–110 frames per second. Defining a square region of interest (ROI) less than 380 pixels in each dimension and centered (vertically) on the CMOS

detector allows for indefinite spooling of data directly to a hard drive disk.

2.2 Ag Nanoparticle Sample Preparation

A thin glass sample chamber was constructed out of silicone rubber and coverglass that allowed imaging nanoparticles with the microscope. The procedure of construction is shown in Figure 2.3. A silicone rubber sheet of 180 µm (McMaster-Carr, PN:87315K61) was cut into a 22 mm × 30 mm rectangle. The center of the silicone rubber rectangle was punched out with a single-hole hole punch leaving a circular cutout in the center of the silicone rubber. The punched silicone rubber rectangle was washed thoroughly with water and dried using nitrogen to remove any excess silicone rubber or debris. A 22 mm × 30 mm coverglass (Fisher Scientific, No. 1.5, 12-544-A) handled with steel tweezers was rinsed with methanol (Sigma Aldrich, ACS Grade) and dried with nitrogen. The punched silicone rubber rectangle was rinsed with methanol and dried with nitrogen and then immediately place carefully onto the coverglass such that the cutout circle was close to the center of the cover glass (Figure 2.3a). Bubbles were removed between the rubber and the glass by smoothing the silicone rubber rectangle using the flat part of a stainless steel tweezer.

High-quality crystalline Au nanoplate mirrors were synthesized using a polyol synthesis method [78–80] and were solvated in water. The solution of Au nanoplate mirrors was shaken to suspend the nanoplates in the solution then 10 µL was immediately withdrawn from the bottom of the vial (container) and deposited as a drop into the circular cutout on the coverglass. The Au nanoplate mirrors in the 10 µL volume settle on the glass surface within the circular cutout and the coverslip was set in a petri dish (lid ajar) and allowed to dry overnight (Figure 2.3b). After all the water has evaporated, the coverslip with the Au nanoplate mirrors was rinsed gently with a squirt bottle of 18 MΩ water to remove nanoplates that were not stuck to the glass surface. Coverslips with Au nanoplate mirrors and silicone rubber on them and blank coverslips were O_3 plasma cleaned at 200 W for 10 minutes (MRSEC, Plasma Etch Inc., PE-100). Plasma cleaned coverslips could be used for

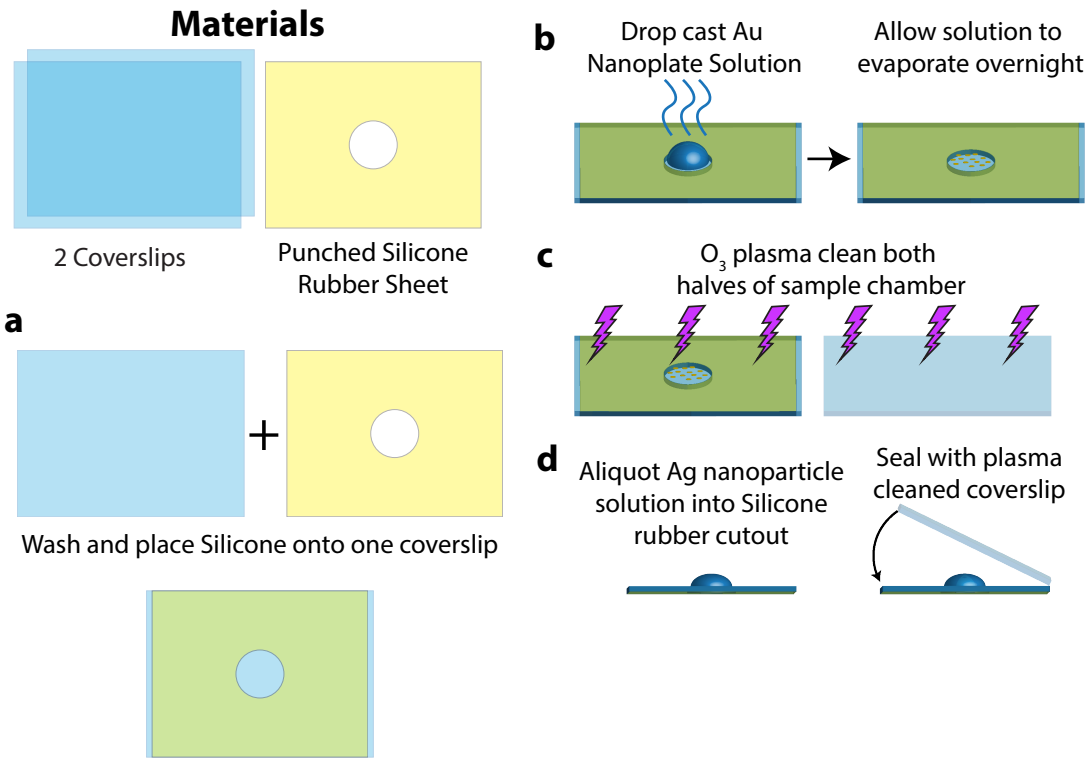

Figure 2.3: Ag nanoparticle sample chamber preparation procedure.

up to 6 hours after cleaning (Figure 2.3c).

A solution of 150 nm citrate capped Ag nanoparticles (NanoComposix, NanoXact KJW1606, 0.02 mg/mL) was diluted 150–800x the stock solution where lower concentration allowed trapping 1–2 particles whereas higher concentration allowed trapping many particles in the optical trap. Once a diluted Ag nanoparticle solution was made it could be used for up to 24 hours before the nanoparticles tended to have increased chance to stick to surfaces. The Ag nanoparticle solution was shaken and sonicated (Cole-Palmer, 8890) in a plastic tube for 10 minutes before use.

The sample cell was completed by depositing a aliquot of the diluted Ag nanoparticle solution of 7–10 µL was on the glass coverslip with the Au nanoplates and silicon rubber. The second, blank, coverslip is carefully placed onto the one containing the aliquot and the silicon rubber by lowering one edged until it touches the plasma cleaned silicone rubber spacer then letting it go at a small angle ($< 60°$) so that the blank coverslip seals to it (Figure 2.3d). If

large air bubbles are present in between the two coverslips in the cutout of the silicone rubber the coverslips are pealed apart and a new aliquot of the diluted Ag nanoparticle solution is re-deposited and resealed until a sample chamber with no air bubbles is created.

Citrate capped Ag nanoparticles were determined to have the best electrostatic repulsion with the Au nanoplate mirror surface which allowed for trapping Ag nanoparticles over the Au surface without much surface interaction. However, polyvinylpyrrolidone (PVP) capped Ag nanoparticles (NanoComposix, NanoXact KJW1882, 0.02 mg/mL) were found to stick to the glass coverslip less often than the citrate Ag nanoparticles when trapped exclusively over glass. Therefore, if the experiment involved only trapping over the glass coverslip surface the same procedure for sample chamber preparation was used except with PVP capped Ag nanoparticles.

2.3 Performing the Experiment

The sample chamber containing the Ag nanoparticle solution is placed on a sample holder oriented so that the coverslip that has the Au nanoplates (if applicable) is on top of the blank coverslip. The sample holder secures the sample chamber with a couple of copper spring clips that are attached with screws on the sample holder. The sample holder is held, with Teflon screws, in a recessed mount on a 3D (xyz) piezo stage mounted on the microscope. The 60x water immersion objective is brought close to the bottom coverslip using the microscope focus until the water droplet on the objective makes contact with the bottom of the coverslip. A single drop of immersion oil (Olympus, Type-F, $n = 1.518$) is placed on the top coverslip and checked that there is now bubbles in the oil before lowering the DFC to make contact with the oil and achieving the dark field condition. The objective is adjusted until the bottom surface of the top coverslip is in the focal plane using the manual focus on the microscope. The back reflections of the laser, visualized with the CMOS detector with the 720 nm SP filter removed, can be used to confirm the correct focal plane as there will be three interfaces where the laser will be reflected (backwards) as the objective is moved towards the coverslip.

These interfaces are: the bottom surface of the bottom coverslip, the top surface of the bottom coverslip, and the bottom surface of the top coverslip. The objective is set so that the reflected laser light is in focus at the third interface. The 720 nm SP filter is inserted back into the optical path to block reflected and scattered 800 nm laser light from reaching the CMOS detector.

Optimizing the ring trap

Some optimization of the optical trapping setup is necessary before any optical trapping experiments can be performed. The SLM is powered on and a $l = 0$ phase mask is displayed using the software LCoS Control (Hamamatsu) or home-built software (named Phase, see Supplemental Material). The optical trapping laser will collect Ag nanoparticles at the bottom surface of the top coverslip in an optical trap. In this thesis, the optical trap is primarily a ring. Once 10–15 nanoparticles are collected in the ring trap the image of the trapped particles is inspected using the CMOS camera in video mode confirming the particles are able to explore all positions around the ring. If the particles are gathered to one side of the ring trap then adjustments are made to the tip and tilt of the turning mirror that is positioned just before the microscope (between L_4 and Dichroic Mirror in Figure 2.1, not shown) until the particles are seen to diffuse over the entirety of the ring. The focus on the microscope is adjusted once more to a position where the particles appear the most confined in the optical trap; *i.e.*, most confined in the radial direction but free to diffuse azimuthally.

Collecting Data

Videos of the trapped Ag nanoparticles are recorded using Andor Solis software. In order to achieve discreet time resolved images, the "Electronic Shuttering Mode" was set to "Global" and a short exposure of $\sim$0.001 s was set in Solis. In Solis a square ROI is set around the ring trap that is less than 380 pixels in each dimension. Solis provides the option to spool data directly to a hard drive disk (HDD) and when using such a small ROI an unlimited number

of frames can be recorded and spooled to the HDD at up to 90 frames per second. The camera chip is cooled to $-30\,^{\circ}\mathrm{C}$ using Solis using the camera's internal fan. Right before data collection, the fan is disabled in Solis allowing for up to 15 min of data collection with the chip maintaining the $-30\,^{\circ}\mathrm{C}$ temperature. The fan is turned off to prevent its vibrations from shaking the camera and the image. The desired trap is selected with LCoS Control or Phase and once the trap has the desired number of particles, "Take Signal" is selected within Solis to begin the data collection. During the data acquisition, the piezo stage can be manipulated manually using the software PI PZT Control to account for focus drift that occurs during the experiment. After the acquisition, data is saved as a ".sif" file on the HDD until further processing.

2.4 Particle Tracking

Several different particle tracking algorithms were used to conduct the research in this dissertation. Particle tracking involves two steps, localization and linking. Localization is the determination of the location (or center) of each particle in each frame, while linking involves connecting these particle positions from frame to frame thereby creating trajectories of particle motions. Some experiments rely on a single software package to do both the localization and the linking, however, others required performing localization with one software package and linking with a different software package. In this section I describe the different tracking algorithms and discuss why each one was used.

The MosaicSuite [72] plugin (termed Mosaic) developed by the Mosaic Group provides a simple way to track particles within ImageJ [70]. For localization Mosaic uses the center-of-mass method developed by Crocker and Grier [71] and for linking uses a modified version of the Crocker-Grier method developed by Sbalzarini and Koumoutsakos [72]. Mosaic only offers four parameters for particle tracking. Two of the parameters, used for localization, are the radius of features and the threshold for detecting local maxima in the image as a feature. The other two parameters, used for linking, are maximum particle displacement between

frames and the memory, *i.e.* the number of frames a particle can disappear and return while still being identified as the same particle. The algorithm doesn't suffer from pixel locking (described in Chapter 6) when the radius of the features is set large enough. Despite being a center-of-mass based algorithm, Mosaic is still quite slow and extremely memory intensive. Because Brownian motion is the only type of dynamics that Mosaic is programmed for, the linking range in a driven ring trap experiment needs to be set very large (*e.g.* $>$ half the frame width) in order for Mosaic to properly link particles. Additionally, it was discovered that Mosaic may swap the identity of nearby particles during the linking step so caution should be used when tracking images of more than 1 particle.

A particle tracking GUI was developed by Raghuveer Parthasarthy (Raghu GUI) in MATLAB (MathWorks Inc., Natick MA) to execute the radial symmetry method of particle localization that he developed [73]. The Raghu GUI provides several localization methods, besides the radial symmetry method, to allow the user to test different methods on their data including the Crocker-Grier center-of-mass method and a non-linear least squares Gaussian fit (NLLS Gaussian) method. Although one of the slowest methods, the NLLS Gaussian fit provides accurate sub-pixel localization of particle centers. The Raghu GUI provides more parameters than Mosaic for particle localization. For example, the size of the Gaussian kernel used for noise reduction in the image can be set explicitly. Also, the Raghu GUI provides three different methods of isolating local maxima in the image as a particle which are: keeping the brightest N pixels, keeping the brightest pixels based on a percentile of pixel intensity in the image, or keeping the brightest pixels that are within a set standard deviation from the median. However, just like Mosaic, the Raghu GUI has the same algorithm for the linking; it assumes diffusive Brownian dynamics. We found that the Raghu GUI would switch the identities of particles when they get close, more often than Mosaic when linking driven Ag nanoparticles in a ring trap. For this reason, the Raghu GUI was used only for localization and not for linking.

Finally, an implementation of the Crocker-Grier method of particle tracking was devel-

oped in Python in a library known as Trackpy [81]. Trackpy is a library that was developed with customization in mind and every parameter is accessible to the user for the localization and linking algorithms. For example, when using the linking method in Trackpy a function can be passed to the software to act as a "predictor" for how it should link particles in successive frames. When linking particles rotating in the optical ring trap a predictor is used to bias the linking of particles in one frame to particles in the next frame with an angular translation based on the rotational velocity of the particles (an implementation of this can be found in Appendix B.1). This allows very accurate linking of trajectories without needing to set the maximum particle displacement between frames to large values. Although Trackpy's localization is based on the Crocker-Grier center-of-mass method, the library does include a method for refining subpixel accuracy using a NLLS Gaussian fit to the image data (implemented in Supplemental Material). In addition to all the features mentioned, Trackpy is also an open source project so any code can be examined or changed to fit the needs of the image data. Without an associated GUI, Trackpy is the most difficult particle tracking software to use (of those described above), however, its customizability makes it by far the most powerful.

2.5 Alignment of the SLM

To properly align the SLM and the positions of L_3 and L_4 the experimental setup was built in parts where the divergence or convergence of the beam is checked at each step. First, the optical instrument in Figure 2.1 is built with the objective, L_4, and L_3 removed. The SLM is powered on and displays a phase mask (with the proper wavefront correction) that performs no phase modulation to the beam. The tip and tilt of the SLM and mirrors between the SLM and the microscope are adjusted so that the optical axis is aligned going straight through the center of the piezo stage after reflecting off of the dichroic mirror in the microscope. The laser beam reflected off the SLM surface is confirmed to be collimated and that the phase profile of the beam is uniform using a Shack-Hartman wavefront sensor (Thorlabs,

WFS150-7AR). Next, the objective is mounted in the microscope. A sample chamber (from Figure 2.3) with Au nanoplates on the top coverslip surface is prepared and mounted on the piezo stage. The focus of the objective is adjusted so the Au nanoplates can be imaged in the microscope and the focus knob on the microscope is set to locked position for the rest of the SLM alignment so the lenses are aligned with a position of the objective that will be used for imaging. The sample chamber is removed from the piezo stage and the L_4 is placed into the instrument roughly 50 cm from the back of the objective on a 3D (xyz) translation stage. The objective and L_4 effectively create a telescope lens system where the optimal position of L_4 is where the beam coming out of the objective is collimated. The position of L_4 is adjusted so that the beam coming out of the objective is as collimated as possible. After L_4 is correctly positioned, L_3 is added to the instrument roughly 125 cm before L_4 along the optical path on a 3D (xyz) translation stage. The distance of L_3 from L_4 is adjusted such that the beam after L_4 is collimated. Finally, after L_3 is in the correct position, the SLM is positioned 75 cm before L_3 along the optical axis. The result of this alignment procedure produces a lens relay system between the plane of the SLM and the focal point of the objective.

2.6 Optimizing the SLM and Developing Phase Masks

2.6.1 Testing the SLM Lookup Table

As discussed in Chapter 1 a SLM modifies the phase of light by using a liquid crystal array where the crystals in each pixel can be oriented to change the refractive index of light passing through it. The orientation of the liquid crystals are controlled by a modulated drive voltage across two electrodes on either side of the liquid crystal cell. However, the liquid crystal orientation has a non-linear response with respect to the voltage applied across the electrodes. Also, the SLM controller can apply voltages to the liquid crystals beyond what is necessary for a 2π phase shift (*e.g.* a pixel can modulate the phase of light from 0 to 3π).

Therefore, a lookup table (LUT) is necessary in order to turn the desired phase in a phase mask into the voltage value that produces the desired phase shift in the liquid crystal. The LUT is designed for two purposes: 1) to linearize the phase response of the SLM and 2) limit the phase modulation to values between 0 and 2π. When a phase mask is set to be displayed on the SLM the SLM controller turns the pixel values (in the mask) into voltage values to use for the electrodes in each pixel of the SLM. The LUT makes it so that the phase mask image with values from 0 to 255 (for 8-bit) modulates the phase of the beam between 0 and 2π respectively.

The phase response of a SLM can be measured through different methods. The Hamamatsu tech sheet on liquid crystal on silicon SLMs outlines a method using a pair of cross polarizers to measure the phase response of a SLM [82]. However, the simplest method to measure the phase response of the SLM is to use a series of masks that contain two different phases and see the response of the beam when one of the phases is changed and the other remains fixed. For example, a series checkerboard patterned masks (Figure 2.4 a and b) of two different image values where one of the checks remains at a fixed value and the other is changed will cause maximum diffraction when the checks are π out of phase from one another and no diffraction when the checks are in phase. A checkerboard phase mask where phases are shifted by π results in a diffraction pattern that diverts light away from the center of the optical axis. Therefore, the power of the center of the beam can be measured to determine the phase response of the SLM as the value of the checks in the checkerboard phase mask are scanned through from 0 to 255. When the checks in checkerboard phase mask are in phase on the SLM then there is no diffraction and the full power of the laser is measured. However, when the checks on the SLM are π out of phase then the power measured in the center will be a minimum in the laser power. If the LUT of the pixel values is linear with respect to the phase response of the SLM then Figure 2.4a would produce no diffraction because the values 0 and 255 would correspond to a 0 and 2π phase shift respectively, while Figure 2.4b would result in maximum diffract because the values 128 and 255 would correspond to a π

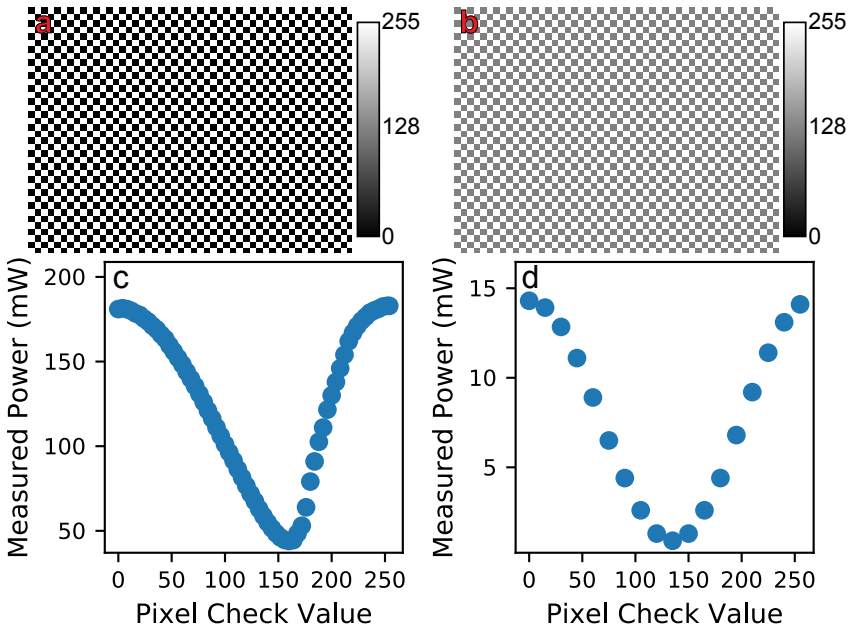

Figure 2.4: Phase masks used for lookup table calibration and power readings from different lookup tables. (a) Checkerboard phase mask where the checks are set to either 0 or 255. (b) Checkerboard phase mask where the checks are set to 128 or 255. (c and d) Power reading (y-axis) of the center (non-diffracted) beam resulting from the different checkerboard phase masks where one of the checks had a value of 255 and the other was varied (x-axis value). (c) The power reading from the checkerboard measurement of a poorly optimized SLM LUT. (d) The power reading from the checkerboard measurement of an optimized LUT. Note: the beam was attenuated in (d) compared to (c) to have a factor of ∼10x less power.

and 2π phase shift.

In order to measure the phase response of the SLM due to the varying checkerboard phase masks a power meter was placed after L_3 but before L_4 in Figure 2.1. The power meter was placed near the focus (not at the focus) after L_3 where the center beam (for checks that are in phase) is separated from the beams caused by the diffraction (for checks that are out of phase). An iris diaphragm was placed before the power meter and was set to block all diffracted light and only measure the power of the center beam. The power of the center beam was measured with the power meter for the different values of the checks in the checkerboard phase masks for both with the LUT turned off in the software (Figure 2.4c) and with the manufacturer provided LUT (Figure 2.4d). When no LUT is used the phase modulation of the SLM had some desirable characteristics such as the phase for the checks

equal to 0 are the same phase as for checks equal to 255. However, the phase response of the SLM is not linear with respect to the pixel values which produces a minima in the power at pixel value of 160 instead of at 128, the latter being where one would want the pixels to be π out of phase with one another and have maximum diffraction (and minimum power). When the manufacturer's LUT is used the power curve (Figure 2.4d) is has a sinusoidal shape with a minimum at pixel value of 135. Even though the manufacturer's LUT produced maximum diffraction at 135 it was still close enough to the desired value of 128 to not be a concern.

2.6.2 SLM Wavefront Correction

The liquid crystals that control the phase of light incident on the SLM are adhered to a very thin mirror which can distort or bend easily. Manufacturers, like Hamamatsu and MeadowLark, know that the surface of the mirror is not perfectly flat and provide a phase correction mask (known as wavefront correction) that compensates for the phase imparted from the distortions in the mirror [82]. However, the proper wavefront correction for a SLM can change if the mirror behind the liquid crystals distorts further. The procedure in this section presents one method of how to determine the proper wavefront correction phase mask for a SLM and is partially adapted from Jesacher [83].

To measure the wavefront of the SLM a Michelson interferometer [84] was constructed using the SLM as one of the arms in the interferometer. The optical system in Figure 2.5 was constructed after the periscope in the optical trapping system in Figure 2.1. The SLM is powered on and set to display a black, all 0 valued pixels, phase mask. The wavefront correction feature was disabled in the SLM software or set to a wavefront correction mask that performed no phase modulation (*e.g.* an all black 0 valued pixels mask). The beam after the periscope in Figure 2.1 was directed towards the SLM and sent through a beam expander (Thorlabs, BE02-05-B) where the beam was expanded the maximum amount in order to fill the entire SLM and make the intensity profile as uniform as possible. The expanded beam passed through a 50:50 dichroic beam splitting cube (BSC) (Thorlabs, CM1-BS2, 700 nm–

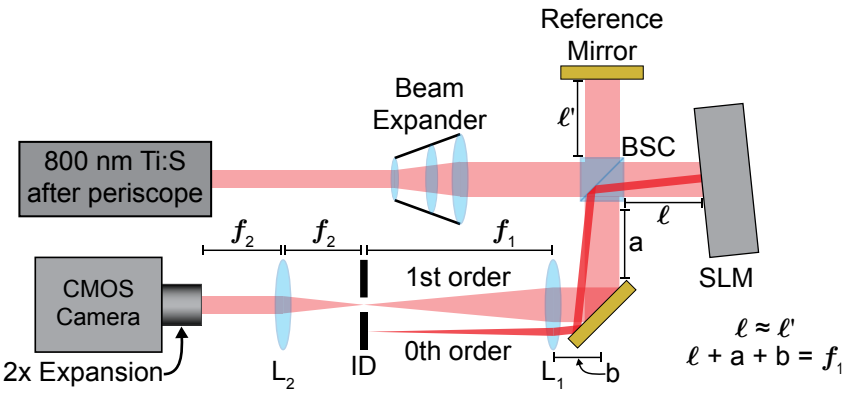

Figure 2.5: Interferometer setup for determining the wavefront correction for the SLM. The setup is built after the periscope in the schematic from Figure 2.1. The abbreviations are lens L, iris diaphragm ID, spatial light modulator SLM, and beam splitting cube BSC. The large pink beam shows the path of the 1st diffracted order off the SLM while the small red beam shows the 0th order off the SLM.

1100 nm) mounted on a single axis translation mount (z) and a 2-axis prism mount (tip and tilt) that directed half the beam to the SLM and half to a reference mirror. The distance of the reference mirror from the BSC was adjusted to roughly match the distance of the SLM to the BSC. The tip and tilt of the reference mirror and the SLM were aligned such that the incident and reflected beams from the BSC remained collinear. A $4f$ lens system was used to relay the image of the SLM to the CMOS camera. A 50 cm lens (L_1 in Figure 2.5) is placed 50 cm from the surface of the SLM along the optical path. Next, 70 cm from L_1, a 20 cm lens (L_2 in Figure 2.5) is placed in order to complete a $4f$ relay system. A CMOS detector (Andor, Neo sCMOS DC-152Q-C00-FI) with an attached 2x expander is placed 20 cm from L_2 and is adjusted until an in focus image of the SLM surface and interferogram can be viewed using the CMOS detector.

At this point, the interferogram imaged on the CMOS detector is a combination of the 1st order diffracted light (due to a lack of wavefront correction) and 0th order non-diffracted light. To isolate the 1st order diffracted light from the 0th order non-diffracted light the SLM is rotated ∼10 degrees in the direction parallel to the optical table. Then, a blaze grating phase mask (Figure 2.6a) is displayed on the SLM that will shift the 1st order diffracted beam to compensate for the ∼10 degree rotation of the SLM. The blaze grating phase used

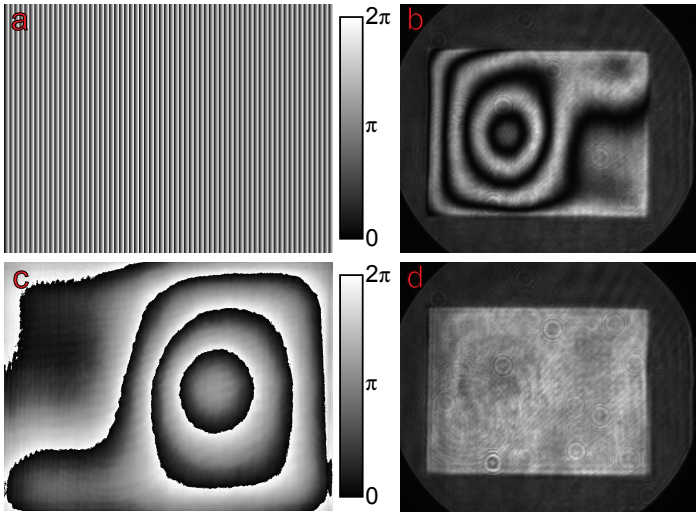

Figure 2.6: Phase masks and interferograms for SLM wavefront correction. (a) Blazed grating phase mask displayed on the SLM to separate the non-diffracted 0th order light. (b) An image of the interferogram of the SLM with no wavefront correction phase function. The dim large circular intensity in the image is from the beam that comes from the reference mirror and overfills the rectangular shaped beam from the SLM. (c) The wavefront correction mask retrieved from a series of interferograms. The correction is inverted through the origin compared to (b) due to the numbers of lenses in the imaging system. (d) An image of the interferogram of the SLM with the wavefront correction function (from c) applied.

should be adjusted such that the first order diffracted light returns to propagating collinear with the beam from the reference mirror. Small changes were made to the blaze grating on the SLM or the tip/tilt of the reference mirror to make the interferogram viewed on the CMOS detector to have the fewest number of fringes possible which resulted in the image in Figure 2.6b. The interferogram in Figure 2.6b represents the phase distortions imparted on the beam from the SLM due to the non-uniform shape of the mirror adhered to the liquid crystal pixel elements.

To extract out the phase function from the interferogram in Figure 2.6b a measurement of the interferograms for different phase shifts was recorded. In a traditional Michelson interferometer, the phase is shifted by changing the path length of the reference mirror by fractions of a wavelength and movement of the fringes in the interferogram relate to the phase profile of the sample. However, the sample (SLM) can modify the phase of light so instead of moving the reference mirror a phase shift is added to the phase mask in Figure 2.6a

and the interferogram is recorded. This is equivalent to adding a uniform valued phase mask to the blazed grating in Figure 2.6a and taking the modulo 2π, which is also known as adjusting the Z_0^0 Zernike mode. The interferograms from five different phases recorded were: 0, $\pi/2$, π, $3\pi/2$, and 2π. Each interferogram recorded was similar the one in Figure 2.6b but the fringe pattern appeared shifted with each phase step. The five interferograms were cropped in ImageJ so that only the rectangular interferogram was visible and, if necessary, were transformed (*e.g.* rotated) to compensate for the CMOS detector was not perfectly parallel to the optical table. The cropped interferograms were imported into a Python script (see Supplemental Material) that performed the phase retrieval. In the Python script the value of each pixel was scaled so that max value in the interferogram was set to 1 and the minimum value was set to 0. The phase of the SLM was determined from the intensities of the pixels in each interferogram using the Hariharan phase retrieval algorithm [85]:

$$\text{phase} = \arctan\left(\frac{2I_2 - I_4}{I_1 - 2I_3 + I_5}\right), \tag{2.1}$$

where I_1, I_2, I_3, I_4, and I_5 are the scaled pixel intensities from each interferogram with phase shifts 0, $\pi/2$, π, $3\pi/2$, and 2π respectively. The phase for each pixel was calculated using equation 2.1 which results in a wavefront correction phase mask to correct the deformities of the SLM mirror surface. The wavefront correction phase mask is inverted through its center to account for the number of lenses in our imaging setup and is scaled (in x and y) to the proper size to be displayed on the SLM shown in Figure 2.6c. Once the wavefront correction was applied to the SLM (added to the blazed grating in Figure 2.6a) the interferogram (Figure 2.6d) showed no interference fringes demonstrating that the distortions from the SLM had been compensated for.

2.6.3 Phase Mask Development

The SLM displays a phase mask which is a spatial representation of how the phase of the light will be modulated after reflecting off the SLM surface. The trapping instrument outlined in Figure 2.1 is designed to relay the phase function from the SLM to the Fourier plane in the microscope at the objective focus. Therefore, the Fourier transform of a phase mask produces the phase and intensity expected at the optical trapping plane in the microscope. Since any optic can be represented as how it distorts the phase of the electromagnetic field, the SLM has the capability to serve as any type of optic. For example, lenses perform a parabolic distortion of the phase of light that pases through it which causes the beam to converge and focus, while mirrors tilt the phase front of the light to propagate in a new direction. The phase functions that perform operations including focusing or tilting can be represented by Zernike polynomials [86] which are functions that are orthogonal on a unit disk. Several of the Zernike polynomials and their optical distortions are listed in Table 2.1 (adapted from [87]). The Zernike polynomials describe the way the phase of the beam should change in polar coordinates, ρ and θ, with respect to the center of the optical axis of the beam. To use these polynomials in a phase mask the phase mask pixels need to be represented in polar coordinates with the center of the mask set to $\rho = 0$. The phase mask of the desired Zernike polynomial is created from:

$$\text{Phase mask} = 2\pi k Z_n^m(\rho_{ij}, \theta_{ij}) \mod 2\pi, \tag{2.2}$$

Table 2.1: Relevant Zernike polynomials and their associated optical distortions.

Radial degree (n)	Azimuthal degree (m)	Z_n^m	Optical distortion
0	0	1	Piston
1	1	$2\rho\cos\theta$	Tip
1	-1	$2\rho\sin\theta$	Tilt
2	0	$\sqrt{3}(2\rho^2-1)$	Focus/Defocus
2	-2	$\sqrt{6}\rho^2\sin 2\theta$	Oblique Astigmatism
2	2	$\sqrt{6}\rho^2\cos 2\theta$	Vertical Astigmatism
4	0	$\sqrt{5}(6\rho^4-6\rho^2+1)$	Spherical Focus/Defocus

where ρ_{ij} and θ_{ij} are the radial and angular coordinates respectively of pixel (i, j), Z_n^m is the Zernike polynomial, and k is a factor that describes the magnitude of optical distortion. For example, when using Z_2^0 for creating a lens function a $k = 10$ would have a shorter focal length than $k = 1$. These Zernike polynomials (or any phase function) can be added to any existing phase function to impart that phase character on the beam in addition to performing the original phase masks' function. Therefore, adding the focusing Zernike polynomial to a ring phase mask will shift the focal plane of the the optical ring trap. The first 11 Zernike polynomials are accessible either standalone or can be added to any phase function using the home-built software for controlling the Hamamatsu SLM (see Supplemental Material).

However, more exotic phase functions cannot be described by a combination of Zernike polynomials. To create optical traps shaped like lines [88] or rings [89] requires phase functions that designed for that specific purpose. Sometimes the the phase function can be inferred, for example a line trap is a cylindrical lens that focuses the beam in one dimension but not the other. Others, like the ring trap, are determined analytically by determining a phase function which, when Fourier transformed, produces the desired intensity. Finally, the phase functions increase in complexity when a gradient force in a certain direction is desired. For example, the optical ring vortex traps used primarily in this thesis originate from an analytical expression that combines the optical vortex beams [21, 90] with the optical ring trap [91]. Many other exotic phase patterns can be found through reading the optical trapping literature.

Finally, there are several methods to create phase functions that produce the desired beam intensity in the focal plane of the microscope objective. If you want two separate traps to appear in the focal plane at the same time a simple way to accomplish this is to create two blazed grating phase masks to divert the beam in different directions then create a new mask by randomly sampling from each of the two blazed grating masks. Doing the random sampling will make half the beam intensity diffract according to one blazed grating and the other half will diffract according to the other blazed grating. More traps can be created by

sampling more masks (*e.g.* three, four, five, etc.) at the expense of of splitting the intensity between each trap. If the desired intensity profile in the focal plane is more complicated than a series of Gaussian traps then a phase mask can be calculated using an iterative phase retrieval algorithm. The Gerchberg-Saxton (GS) algorithm is an iterative phase retrieval algorithm that determines the phase function to create a desired intensity [92]. The electric field can be represented as:

$$E^{\text{in}}(\mathbf{r}) = A^{\text{in}}(\mathbf{r}) \exp[i\phi^{\text{in}}(\mathbf{r})], \tag{2.3}$$

where A^{in} is the amplitude of the beam at the SLM plane and ϕ^{in} is the phase of the SLM. When equation 2.3 is Fourier transformed the electric field at the optical trapping plane is recovered:

$$E^{f}(\mathbf{r}) = A^{f}(\mathbf{r}) \exp[i\phi^{f}(\mathbf{r})], \tag{2.4}$$

where A^f and ϕ^f is the amplitude and phase at the optical trapping plane respectively. When equation 2.4 is inverse Fourier transformed then the electric field in the SLM plane (equation 2.3) is recovered. The GS algorithm converges on a phase by iteratively Fourier transforming and inverse Fourier transforming between equations 2.3 and 2.4 while replacing the amplitudes at each step. To start, the amplitude in equation 2.3, A^{in}, is always the amplitude of our incident beam which is a Gaussian function, while the phase is initially random values. Equation 2.3 is Fourier transformed to find A^f and ϕ^f in the focal plane. Next, the A^f is replaced by the desired amplitude, *i.e.* the desired shape of the beam in the optical trapping plane. Then, equation 2.4 is inverse Fourier transformed to find A^{in} and ϕ^{in} where A^{in} is replaced once again with the Gaussian amplitude that represents the beam incident on the SLM. Afterwards, equation 2.4 is Fourier transformed again and the process is repeated until ϕ^{in} converges and does not change appreciably between iterations. The GS algorithm converges quite quickly so to retrieve a phase mask only several iterations of the algorithm need to be calculated (*e.g.* 5 to 10 iterations). However, because the

GS algorithm converges quickly the final phase may not be optimal. Variations of the GS algorithm exist where the phase retrieval is slower but results in a better phase mask such as the adaptive-additive algorithm [31].

CHAPTER 3

DRIVEN OPTICAL MATTER: DYNAMICS OF ELECTRODYNAMICALLY COUPLED NANOPARTICLES IN AN OPTICAL RING VORTEX

Reproduced in part with permission from: Patrick Figliozzi, Nishant Sule, Zijie Yan, Ying Bao, Stanislav Burov, Stephen K. Gray, Stuart A. Rice, Suriyanarayanan Vaikuntanathan, and Norbert F. Scherer. Driven optical matter: Dynamics of electrodynamically coupled nanoparticles in an optical ring vortex. *Phys. Rev. E*, 95(2):022604, doi: 10.1103/PhysRevE.95.022604. Author contributions: Nishant Sule performed the ED-LD, Langevin Dynamics, and FDTD simulations. Ying Bao synthesized the Au nanoplates used in the experiments. Stanislav Burov developed the mean-squared displacement model. Zijie Yan built and maintained the optical trapping instrument used in the experiments. All authors discussed the results and commented on the manuscript.

3.1 Introduction

There is much interest in understanding and controlling the collective motions that arise in driven systems of colloidal particles in solution [67, 68, 94, 95]. These studies quantify of the influence of hydrodynamic interactions that also play a role in the collective dynamics of self-propelled active matter systems [96–99]. It is becoming increasingly common that optical fields and forces are used for these studies as intensity and phase gradients can confine particles without introducing physical boundaries that would alter the hydrodynamic interactions and yet can produce large deterministic forces to drive single polarizable microparticles or large numbers of them [39, 94]. Shaped optical fields can be applied to manipulate single and multiple nanoparticles by optical forces arising from momentum transfer, *e.g.*, trapping by intensity gradient forces exerted by a tightly focused Gaussian beam, or pushing by radiation

pressure due to absorption and scattering [100, 101].

Alternatively, light that possesses spin [102] or orbital angular momentum (OAM) [103] can cause nanoparticles to spin or undergo orbital rotational motion [104–107]. Optical beams possessing OAM are colloquially termed optical vortices [90], as these beams exhibit annular cross-sections and tilted phase fronts. Following the observation of rotating microparticles driven by an optical vortex laser beam [108], the transfer of OAM from photons to microparticles has been widely exploited [90, 91, 104, 108–120], especially for investigating hydrodynamic coupling between multiple particles [67, 94, 114, 116, 121–123].

In an optical vortex, each photon has an angular momentum of $l\hbar$, where l is the topological charge of the vortex (*i.e.*, the total phase shift upon circling the vortex center divided by 2π) [103]. Theoretically, the angular velocity of a rotating particle will be linearly proportional to l assuming that the total photon flux incident on the particle is always the same [90, 110]. However, this assumption is usually not valid. The classic optical vortices, *i.e.*, Laguerre-Gauss beams [103], have varying radii depending on l [90], which means the intensity on the particle will change with different topological charges.

A vortex with constant intensity profile and radius that is independent of l is an ideal optical field to study motion and particle interactions as a function of the drive, or l. A class of "perfect optical vortices" (*i.e.* holographic ring traps) produced only using a SLM was introduced in Roichman et al. [91] to study the dynamics of driven microparticles; a linear dependence of particle rotation rate on l was found only when $l \geq 20$ [39]. An alternative route to creating a "perfect optical vortex" [124] was recently demonstrated by making an optical ring with an axicon and a lens and then adding OAM to the ring with a spatial light modulator (SLM) [125]. The dynamics of microparticles pushed against a coverslip surface by the optical vortex were investigated and a linear dependence of particle rotation rate on l was obtained, but only when $l \geq 2$; the particles did not start to rotate at $l = 1$ due to the frictional forces on the microparticles and the limited laser power [124]. Lehmuskero et al. [119] have recently demonstrated that (plasmonic) metal (Au) nanoparticles can be

trapped and driven in focused optical vortex beams. Therefore, a better demonstration of OAM transfer could result from a tightly focused optical vortex and particles with smaller frictional forces, *e.g.*, nanoparticles and/or trapping away from a surface.

Nonequilibrium studies of trapped and driven colloids such as those listed above focus on hydrodynamic forces. Yet, electrodynamic forces and interactions can be important [40, 41, 126–130]. The relative importance of hydrodynamic and electrodynamic interactions changes with particle size, particle spacing, and the constitutive nature of the particles (*e.g.* dielectric with small or large index of refraction or metallic particles, *etc.*). In fact, as the size of the particles decrease and with a suitable choice of material (*e.g.* metal) the intense scattering of the trapping field can lead to strong electrodynamic interactions amongst the particles [43, 44, 100, 131].

In this chapter, we introduce and characterize a constant-radius optical vortex that is created by interfering a holographic ring trap using a retro-reflection geometry with a gold (Au) nanoplate mirror [131]. We study the dynamics of single and multiple silver (Ag) nanoparticles driven by the optical vortex to clearly demonstrate OAM transfer from $l = -5$ to $l = 0$ to $l = +5$. We also perform comparative experiments with these nanoparticles trapped near an electrostatically slightly charged (repulsive) glass surface. We show that multiple nanoparticles in the optical vortex are electrodynamically coupled *via* optical binding interactions [40, 44, 104, 131], resulting in the formation of optical matter [18], which is in distinct contrast with the hydrodynamically coupled microparticles in nearly all previous reports. The use of metal nanoparticles and the concomitant strong optical binding interactions are key aspects of our study. The experiments achieve modest nonequilibrium conditions, with Péclet numbers [68] in the range of 0.2–5 for trapping at a glass interface or 3–75 when over a Au nanoplate mirror. Using combined electrodynamics-Langevin dynamics (ED-LD) simulations [132] we demonstrate that the optical drive force and the interparticle interactions vary in a sinusoidal manner for linearly polarized light, which is confirmed in experiment. The ED-LD simulations allow us to quantitatively explain how these electrodynamic inter-

actions affect interparticle dynamics. We examine the dynamics of the electrodynamically interacting Ag nanoparticles in detail by varying the optical drive force in traps over glass and the Au nanoplate mirror demonstrating that the fluctuations or noise in the interparticle separations increase with increasing optical drive. Moreover, theory and model Langevin simulations allow explaining the increasing noise with increasing l, and hence the effective temperature of the interacting particle system as resulting from the periodic modulations in optical forces. Finally, we demonstrate, with comparative measurements of driven 0.3 µm diameter polystyrene beads, that the electrodynamic interactions should not be neglected for driven dielectric particles, which might give rise to some structural and dynamic features that have been attributed exclusively to hydrodynamic interactions.

3.2 Results and Discussion

3.2.1 Generating and Characterizing an Optical Ring Vortex

The optical ring vortex was produced by phase modulation of a linearly polarized Gaussian beam from a cw Titanium Sapphire laser operating at $\lambda = 800\,\text{nm}$. The SLM modifies the incident Gaussian field with a phase function [89, 91]

$$\phi(\vec{\rho}) = AJ_l(CR\rho)e^{il\theta} \tag{3.1}$$

where $\vec{\rho} = (\rho, \theta)$ denotes the polar coordinates relative to the optical axis, A is the amplitude of the incident Gaussian beam, J_l is the l-th order Bessel function of the first kind, C is a constant that is calculated from the focal length and wavelength of the optical system, and R is the radius of the ring (See Figure 3.11 in the Chapter Appendix for images of the phase mask produced using the phase function above). In our case a microscope objective (Olympus 60x, $N.A. = 1.2$, SAPO) Fourier transforms the phase-modulated incident optical field and generates a focused optical ring vortex.

The 3D profile of the optical vortex is illustrated in Figure 3.1a; the vortex evolves into an optical ring at the focal plane and its 3D intensity profile along the optical axis is symmetric across the optical ring. This symmetry enables a retroreflection geometry when a Au nanoplate mirror is positioned at the focal plane, where the reflected beam interferes with the incident beam that generates a series of optical ring traps along the optical axis, as illustrated in Figure 3.1b. The optical ring trap we use in the experiments is the first fringe (antinode) of constructive interference above the Au nanoplate mirror, which is located approximately 250 nm away from the Au nanoplate surface. This particle center to nanoplate surface distance is determined from electrodynamics simulations (see Figure 3.12). In the experimental configuration in Figure 3.1a the scattering force pushes the particles towards the electrostatically charged glass surface but the Ag nanoparticles are also electrostatically charged with the same sign, so that the particles are repulsively trapped by the opposing scattering force of the optical trap and the electrostatic repulsion from the glass surface. In contrast, the surface-particle interactions and frictional drag are substantially reduced over the Au nanoplate mirror since the particles get trapped at the first interference fringe ~ 250 nm above the Au nanoplate surface. Therefore, the dynamics of the Ag nanoparticles are different in the two configurations.

The retroreflection and constructive interference also increases the intensity of the light in the trapping region by a factor of 4, resulting in a deeper trap potential that restricts the particles to a tighter ring than the analogous trap over the glass. Evidence of this is shown in the top two plots in Figure 3.2a where the probability of finding a 150 nm diameter Ag particle over glass (blue, left) has greater radial breadth (*i.e.* radial fluctuations) than for a nanoparticle over the Au nanoplate (red, right). The difference in the trap strength is more apparent when looking at the particle distributions in polar coordinates (Figure 3.2b). The radial width of the distribution of particle positions is larger when trapping over glass (blue, left) than over the Au nanoplate (red, right).

The difference between the nanoparticle trapping over glass or with the retroreflection

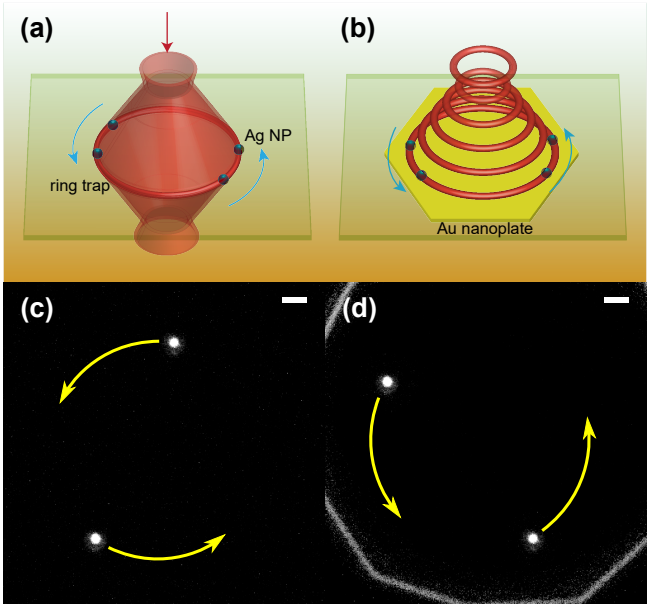

Figure 3.1: Schematic of the focused optical beam and ring trap over (a) a glass coverslip and (b) a Au nanoplate. A dark-field optical microscope image of two Ag nanoparticles trapped (c) over glass and (d) over a Au nanoplate mirror. The bright line segments and polygonal shape are the edges of the Au nanoplate. Note the Au nanoplate overfills the panel. The curved arrows in (c) and (d) indicate the direction of rotation of the nanoparticles in the optical vortex ring trap. The white scale bars in (c) and (d) is 1 µm.

over the Au nanoplate mirror can be approximately replicated in the simulation by using different electric field intensities. An electric field intensity I_0 is used in the ED-LD simulations over glass while the simulations over the Au nanoplate are performed with an intensity of $4I_0$ corresponding to a constructive interference antinode. Although, the motion of the nanoparticles along the optical axis (z) would be different for trapping at the glass interface and over the Au nanoplate, we are interested in the motion of the particles driven in the transverse (x-y) plane of the optical axis. Therefore, the simple approximation of using twice the value of the incident field (or $4I_0$) is sufficient for the purpose of understanding the behavior for different drives. Figure 3.2c shows the trajectory of a simulated nanoparticle at intensity I_0 with an $l = 2$ applied angular force. The amount of radial diffusion qualitatively matches the distribution for the experiment over glass, shown in blue (left) in Figures 3.2a and 3.2b. The trajectory in Figure 3.2d, calculated from simulations with an intensity of $4I_0$ while keeping the same $l = 2$ angular force, matches the distribution of the particle positions in the experiment, shown in red (right) in Figures 3.2a and 3.2b. The total duration of the simulated trajectories shown in Figures 3.2c and 3.2d are the same so it is clear from the figures that the particle moves a shorter distance for the lower intensity source.

3.2.2 Imparting Orbital Angular Force

Unlike traditional vortex beams, the intensity profile and the radius of the optical ring vortex are independent of l for the phase masks we apply (see Figure 3.11), while the optical angular force in the optical trap can be varied as desired. The size and intensity of the optical ring vortex can be calculated by taking the Fourier transform of the phase mask for each l, showing that the trap's radius and intensity profile are independent of l (Figure 3.11). However, the phase profile depends on l as seen in the third column of Figure 3.11, where the phase gradient is $\nabla\phi = \frac{2\pi l}{2\pi R} = \frac{l}{R}$ around the ring. That phase gradient may be viewed as the source of optical angular force in the optical vortex. The phase gradient also gives rise to an optical force $F_l \propto I\nabla\phi$ [39, 133] that will drive trapped particles around the ring.

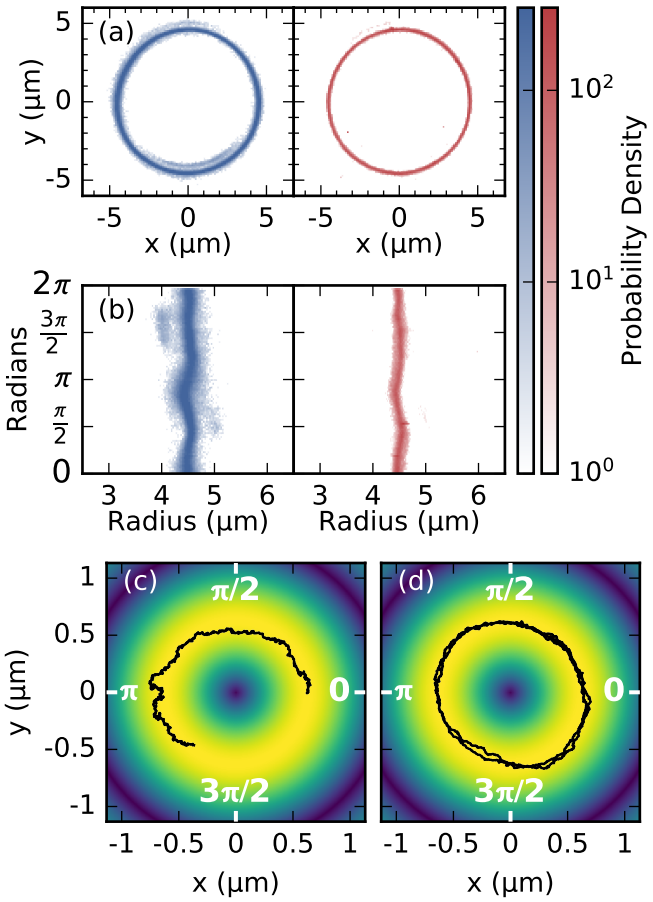

Figure 3.2: Probability densities and simulated trajectories of particles in the ring traps. (a,b) Probability densities of particles in the ring traps over glass (blue, left) or over plate (red, right). Distribution of the particle positions in (a) Cartesian coordinates and (b) polar coordinates in the lab frame. (c,d) Electric field intensity (heat map) and particle trajectory from the simulation at intensity I_0 (c) and $4I_0$ (d) for $l = 2$. Example trajectories from the simulation are shown in black.

Since both intensity and radius are independent of l, it is easy to see that $F_l \propto l$, indicating that each increase in l results in a linear increase of rotational force applied to the particles in the ring trap.

The angular optical force applied to particles is examined using the trajectories of Ag nanoparticles in an optical ring vortex. The position of a single Ag nanoparticle is recorded while l is increased every $\sim 11\,\mathrm{s}$ in a ring trap of $R = 9.5\,\mu\mathrm{m}$ with l ranging from 0 to 5 both over glass and over a Au nanoplate. The same identical Ag nanoparticle is used for all measurements over glass and another for all measurements over the Au nanoplate mirror. The nanoparticle's trajectory is determined for each value of l over glass and over the Au nanoplate mirror. The $l = 0$ trajectories show only diffusive behavior of the nanoparticle both over glass and over the Au nanoplate (Figures 3.3a and 3.3b). However, when l is increased the nanoparticle makes deterministic orbits (but with fluctuations) around the ring. The trajectories show that a nanoparticle over the Au nanoplate (Figure 3.3a) completes about six times as many rotations as a nanoparticle over glass (Figure 3.3b) for a given l. In addition the trajectories have fewer fluctuations and more closely follow circular paths (*i.e.* straight lines in the polar representation) in experiments done over the Au nanoplate (Figure 3.3b) than in the experiments over glass; the trajectories over glass are noisier around the linear fits (Figure 3.3a).

The trajectories calculated from simulations using intensities of I_0 and $4I_0$ show the same behavior as the experiments over glass and over the Au nanoplate, respectively. The trajectories from simulations of intensity I_0 (Figure 3.3c) are noisier about the linear fit similar to those observed in the experiment over glass (Figure 3.3a). Likewise, the simulation trajectories at $4I_0$ (Figure 3.3d) show a more linear increase in time just like the experimental results with the optical ring vortex over the Au nanoplate (Figure 3.3b). One difference between the simulated and the experimental trajectories is that there is a noticeable oscillatory deviation from a straight line of the trajectory seen in the simulations, especially for $l = 4$ and $l = 5$ in Figures 3.3c and 3.3d. The oscillatory deviation will be addressed below.

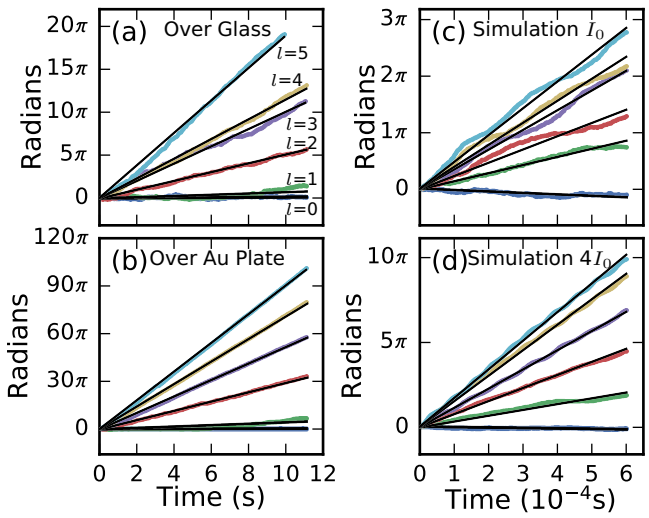

Figure 3.3: Angular displacements *vs* time for experiments and simulations for glass and Au nanoplate conditions and angular drives $l = 0$–5. (a) Experimental trajectories of a single Ag nanoparticle rotation over glass and (b) over the Au nanoplate for six different drives. (c) The trajectories of a single Ag nanoparticle rotation in the simulation with intensity at I_0 and (d) at intensity $4I_0$ for $l = 0$–5. The solid black lines are linear fits of the rotation (angular displacement) versus time.

It should be noted that the simulated optical ring vortex is not the same size as in the experiments mainly due to restrictions on available computational resources and memory. As a result of the smaller size (diameter) of the simulated ring trap and to facilitate more angular motion (rotations) in the $\sim 2\,\text{ms}$ long simulated trajectories, the electric field intensity is 30 times larger than in the experiments. The main consequence of the smaller ring size and larger electric field intensity is that the optical forces and therefore the particle velocities are larger. However, as seen from Figure 3.3 the figures below, the qualitative agreement between the experimental and the simulation data is striking.

The mean squared displacement (MSD) of single particle trajectories reveals the strength of the drive force for different values of l. The MSD from experiment and simulation (Figures 3.4a-d) can be fit with

$$\text{MSD}(\tau, l) = 2D(l)\tau + \frac{F(l)^2}{\gamma^2}\tau^2 \tag{3.2}$$

where $D(l)$ is the l-dependent diffusion constant [134, 135], $F(l)$ is the optical force, γ is the friction coefficient, and τ is the lag time. Here, we assume that the diffusion constant

is independent of the angular drive. The diffusive character of the trapped nanoparticle is most apparent over the glass surface (Figure 3.4a) for short timescales demonstrated by the curve when $\tau < 0.1\,\mathrm{s}$ where the linear term in the MSD is dominant, while when $\tau > 0.1\,\mathrm{s}$ the squared term dominates and the particle's motion is determined primarily by the optical force. Nanoparticles trapped over the Au nanoplate exhibit much less transverse diffusive behavior; the motion of the particles is dominated by the optical drive force (Figure 3.4b).

The plot of $F(l)/\gamma$ as a function of l in Figure 3.4e using the fitting parameters from Figures 3.4a-d, shows that the optical force increases linearly with l from -5 to 5. This result, which is consistent with the theoretical analysis, clearly demonstrates that the optical angular force transfer is linearly proportional to l. Moreover, the slope of $F(l)/\gamma$ over the nanoplate is 5.5 times that over the glass. Constructive interference over the Au nanoplate only increases the intensity of the trap by 4-fold and the angular force $F(l) \propto I$, intensity, so the additional increase of the slope indicates that the friction coefficient, γ, decreases over the nanoplate. The effect of the hydrodynamic friction is apparent when comparing the simulation results in Figure 3.4e to the experimental ones. When the simulation for intensity $4I_0$ (Figure 3.4e, open circles) is aligned with the experimental results over the nanoplate mirror (Figure 3.4e, closed circles) the corresponding simulation results for intensity I_0 (Figure 3.4e, open triangles) do not align perfectly with (*i.e.* have a different slope than) the experimental results obtained over the glass (Figure 3.4e, closed triangles). The 90–100 nm separation of the nanoparticle surface from the glass surface, estimated from a Derjaguin-Landau-Verwey-Overbeek (DLVO) potential treatment for the electrostatics measured and estimated for the experiment (See Chapter Appendix), is within the distance where hydrodynamic interactions with the surface are significant [136, 137]. Therefore, we believe that the discrepancy between the slopes shows the effect of the hydrodynamic friction present in the experiments over glass, which is not accounted for in the simulation.

The oscillating deviations from a linear fit to the particle trajectories found in the simulation (shown in Figures 3.3c and 3.3d) reflect periodic modulations of the particle's velocity.

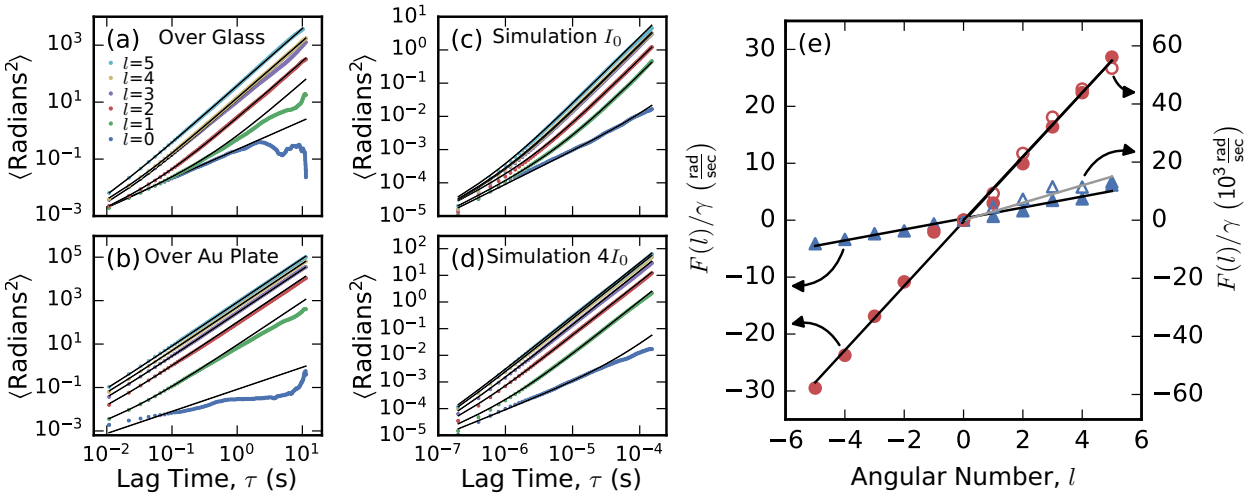

Figure 3.4: MSD of experimental and simulated particle motion and forces on Ag nanoparticles from experiment and simulation. (a, b) Angular MSD for different angular drives l from the experiment trapping over the glass surface (a) or over the nanoplate mirror (b). (c, d) Angular MSD for different angular drives l from simulations with intensity I_0 (c) and $4I_0$ (d). The MSD's for a-d are calculated from the angular displacement vs time results from Fig 3. (e) Fit parameters of $F(l)/\gamma$ from the MSD of single nanoparticles in the optical ring vortex over glass (closed blue triangles) and over the Au nanoplate (closed red circles) using the left y-axis. Fit parameters of $F(l)/\gamma$ from the MSD of single nanoparticle simulations for I_0 (open blue triangles) and $4I_0$ (open red circles) using the right y-axis. Solid black lines show linear fits to the data, the solid gray line shows the fit to $F(l)/\gamma$ vs l for intensity I_0 in the simulation. Note that the vertical axes are chosen so that the fitted lines to the Au nanoplate (and $4I_0$) results are identical.

The particle speed is plotted as a function of its position on the ring in Figures 3.5a and 3.5b. The speeds are calculated using single particle trajectories; both the experimental and the simulation results show a large change of the instantaneous speed as a function of the angular position around the ring. Both the experiment and the simulation show similar angle-dependent modulation of the speed, that behaves as a sine function centered around a non-zero mean value. Figures 3.5c and 3.5d show vector maps of the optical forces acting on a 150 nm-Ag particle for $l = 0$ and $l = 4$, respectively. The direction of polarization (horizontal) is indicated by the gray arrow in the top right corner. The optical forces are calculated from the Maxwell stress tensor by placing the Ag nanoparticle at each position and performing an FDTD simulation to determine the total fields. Larger magnitude optical force vectors are seen in the 0 and π regions of the optical ring vortex for $l = 0$ and in the $\pi/2$ and $3\pi/2$ regions for $l = 4$, respectively. This makes it clear that the linear polarization of the beam creates an anisotropy in the optical forces and results in the velocity oscillations revealed in Figures 3.5a and 3.5b. The force anisotropy for linearly polarized vortex beams was also noted by Lehmuskero et al. [119]. The anisotropy or modulation in the optical forces for linearly polarized light has important consequences for the dynamics of the nanoparticles driven in the optical ring vortex as discussed below.

3.2.3 Electrodynamic Interparticle Interactions

As previously shown [44, 45, 131], Ag nanoparticles interact electrodynamically *via* optical binding; a periodic modulation of the electric field in the vicinity of the nanoparticle resulting from interference of the incident field and the scattered field from each particle. The strength and spatial aspects of optical binding depend on the polarization of the incident beam [44]. In the present experiment the polarization of light is held constant; it is horizontally polarized in the reference frame of the rings shown in the figures. This produces particle-particle interactions that depend on the location of the particles as they move in the ring trap. Pairs of nanoparticles oriented perpendicular to the light polarization direction have a stronger

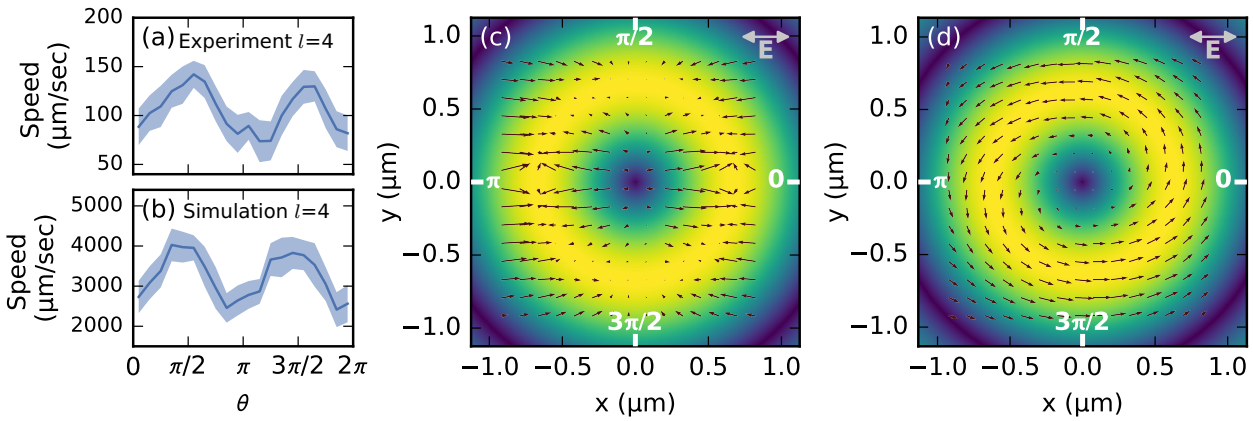

Figure 3.5: Speed and force information of nanoparticles in the optical ring vortex. (a-b) Speed as a function of position around the optical ring vortex in (a) the experiment over the nanoplate mirror at $l = 4$ and (b) in the simulation at intensity $4I_0$ at $l = 4$. The speeds are calculated by taking the difference between the Cartesian positions of the nanoparticles in successive frames in the experiment or timesteps in the simulation and dividing by the time increment (*e.g.* 1/framerate). (c-d) Electric field intensity (heat map) and force vector map in the $4I_0$ simulation at $l = 0$ (c) and $l = 4$ (d).

optical binding interaction than do pairs of nanoparticles aligned parallel [44]. A peak in the probability distribution of interparticle separations at the nearest-neighbor distance results from an optical binding interaction.

The distribution of the nearest-neighbor separations shown in Figure 3.6 demonstrates the effect of polarization on interparticle interactions as a function of angle in the optical ring vortex. These interparticle separations can be further grouped based on sections of the ring trap where particles can arrange aligned parallel to or perpendicular to the polarization. The dashed lines in Figure 3.6 indicate the sections of the optical ring vortex that are binned for the different configurations relative to the polarization of light. Particle pairs are considered parallel to the polarization if they are in a $\pi/8$ slice of the ring centered on the $\pi/2$ or $3\pi/2$ positions. Likewise, particle pairs are perpendicular to the polarization if they are in a $\pi/8$ slice of the ring centered on the 0 or π positions. Figure 3.6 demonstrates that the particles prefer optical binding separations when in the 0 and π positions; the distributions show increased probability to be separated by 0.6 µm, 1.2 µm, and 1.8 µm, which is consistent with past experimental and theoretical results for optical binding [44]. The positions at $\pi/2$

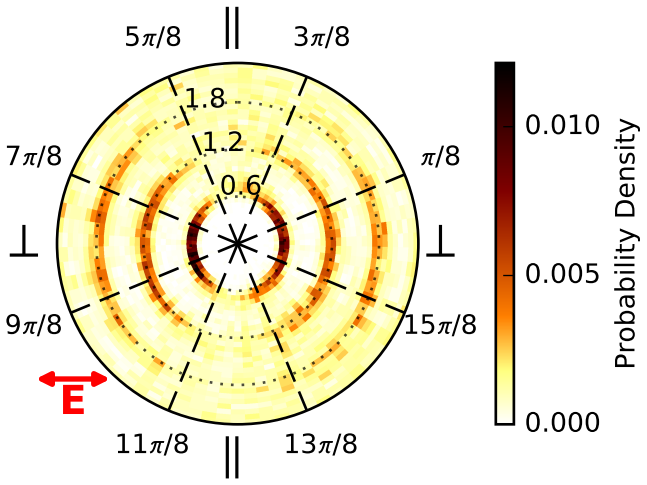

Figure 3.6: Probability density plot of interparticle separations characterized as parallel or perpendicular with respect to the electric field polarization (horizontal to the ring trap). The interparticle separation is plotted with respect to the angular location of the midpoint of a pair. The radial coordinate is the interparticle separation (in µm units). The color represents the probability density of events in the radial and angular coordinates. Four of the octants of the ring trap are categorized as parallel or perpendicular with respect to the electric field. These octants, labeled $\perp$ and $\parallel$, are sections of the optical ring vortex where the trap is perpendicular or parallel to the electric field polarization. This data is from a multi-particle experiment at $l = 2$ over glass. Similar results are obtained for other values of l and also over the Au nanoplate.

and $3\pi/2$ in Figure 3.6 do not show the same effect because the optical binding interactions are weaker for particles aligned parallel to the polarization.

3.2.4 Distributions of Interparticle Separations

The nearest-neighbor separations are examined in the regions where the polarization is aligned parallel or perpendicular to the particles in the ring trap with respect to the driving force for the over-glass *vs* over-nanoplate conditions. Experiments over glass shown in Figures 3.7a-c demonstrate that the optical binding interactions are much more pronounced for nearest neighbors perpendicular to the polarization than particles parallel to the polarization. The emergence of particle interactions at separations corresponding to the second optical binding distance (site) at 1.2 µm are also noticeable, but only observed for particles aligned perpendicular to the polarization where the binding is stronger. The optical binding

increases dramatically over the Au nanoplate as seen in Figures 3.7d-f because the particles trapped in the antinode created by retroreflection experience a 4-fold increase in intensity. Here, the first, second, third, and perhaps the fourth optical binding sites are evident.

The distributions of interparticle separations can be further classified based on the magnitude of the optical angular drive force, $F(l)$, applied in each experiment. We observe that the noise (fluctuations) increase with increasing optical drive force and that this competes with the attractive optical binding interactions. Figure 3.7a shows that the optical binding interactions dominate in the probability distributions of the interparticle separation for small l ($l = 0$, 1, 2), where the first binding site at 0.6 µm is strongly populated and the emergence of the second binding site can be seen at 1.2 µm for particles over glass. Likewise, Figure 3.7d shows very narrow distributions at the first, second, third, and fourth binding distances arise over the Au nanoplate mirror. As the optical drive force increases the distributions broaden around each optical binding site (Figure 3.7b and 3.7e). Finally, at large l ($l = 4$, 5), the distributions are so broad that evidence for optical binding interactions largely disappears beyond the first site at 0.6 µm (Figures 3.7c,f).

We also examined the dynamics of interparticle separations by performing ED-LD simulations with two 150 nm Ag nanoparticles in the optical ring vortex. Unless specified, the two particles were initialized with a separation of 0.6 µm, corresponding to the first optical binding separation, and placed symmetrically around the 0° position in the ring. Figure 3.8a shows the probability densities of the interparticle separations for different values of l. For small l (*i.e.* $l = 0$–1) we obtain a strong peak in the probability density around the first optical binding location (0.6 µm). Increasing the optical driving force on the particles leads to broadening of the first peak and the emergence of probability density at the second (for medium l, *i.e.* $l = 2$–3) and third (for large l, *i.e.* $l = 4$–5) optical binding separations. Thus, the particles separate more easily from their initial condition at the first optical binding site with increasing l. These simulation results are consistent with the experimental results of Figure 3.7. We determined the potentials of mean force at the first optical binding

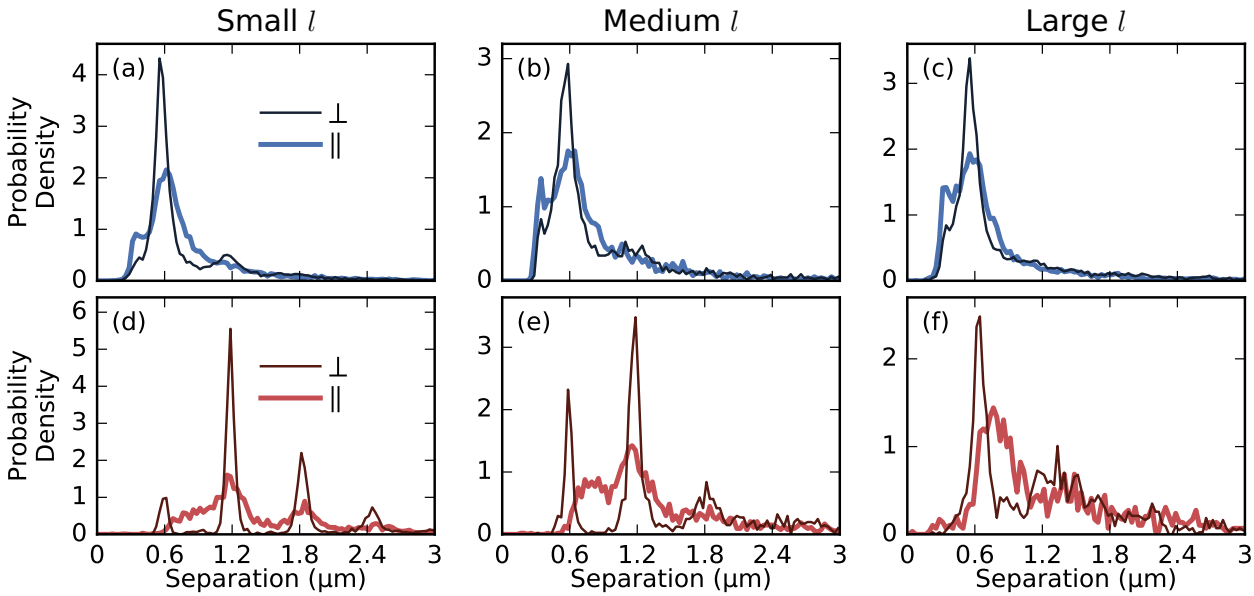

Figure 3.7: Conditional probability distributions of the nearest neighbor separation grouped into categories of (a,d) small (l = 0–2), (b,e) medium (l = 3), and (c,f) large (l = 4–5) applied optical force for experiments over glass (blue, top row) and over the Au nanoplate (red, bottom row). In each panel there are distributions for particle pairs that are parallel (thick light colored curve) or perpendicular (thin dark colored curve) to the polarization. The separations are binned parallel or perpendicular based on the scheme in Figure 3.6. Curves are plotted through the midpoints of the distribution bins.

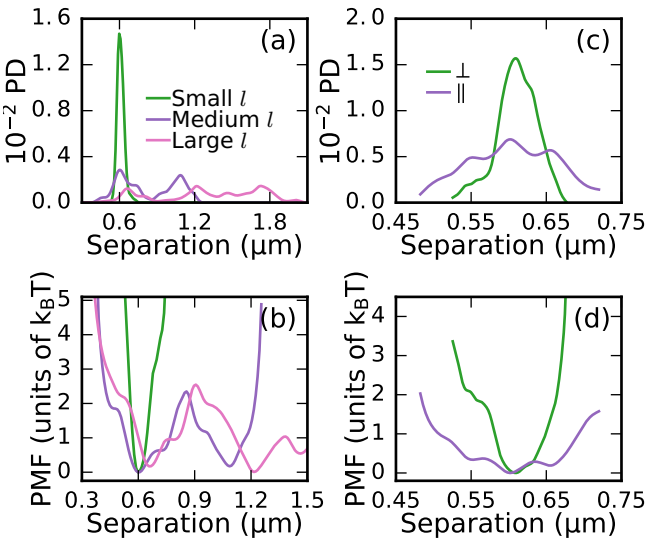

Figure 3.8: Simulations of two Ag nanoparticles in an optical ring vortex with electric field intensity $4I_0$. (a) Probability density (PD) distributions of nearest-neighbor separations for nanoparticle pairs in the simulation for l = 0–1 (small l), l = 2–3 (medium l), and l = 4–5 (large l). (b) Potentials of mean force (PMF) around the first two optical binding sites calculated from the probability densities from (a). (c) Distributions of interparticle separations calculated from simulations for $l = 0$, where the two particles are initialized symmetrically about the $\perp$ (0) or the $\parallel$ ($\pi/2$) positions in the ring. (d) Potentials of mean force for $l = 0$ at $\perp$ (green) and $\parallel$ (purple) calculated from the probability densities in (c). All curves are plotted using a Gaussian kernel density estimator.

site from the interparticle probability densities for the different values of l. As shown in Figure 3.8b, these results demonstrate a diminishment of the effective optical binding potential with increasing l. This means that the noise of the system increases with drive. Further, as shown in Figures 3.8c and 3.8d, we determined the probability densities and corresponding potentials of mean force at the location of the first optical binding site with no optical drive (*i.e.* $l = 0$) in the regions where the polarization of the incident field is aligned perpendicular and parallel to the interparticle axis. Together with the experiments (Figure 3.7), these results demonstrate that optical binding is weaker when the polarization is parallel to the interparticle axis, leading to a broader distribution in the probability density that reflects a shallower (weaker) effective potential.

3.2.5 Increasing Effective Temperature with Drive Force

The experimental and simulation results in Figures 3.7 and 3.8 show that increasing the optical drive force causes an increase in the effective temperature of the system; a larger optical drive force causes particles to fluctuate more and with greater magnitude about the optical binding sites. Note that the total optical intensity on the particles is constant so particle heating is constant for all values of l. The increase in the fluctuations, and therefore the effective temperature with increasing l, could result from the modulation in the optical binding potential. We used the following minimal model system to test this hypothesis. Imagine two particles confined to the perimeter of a circle (as in the experiments) with an angular modulation of the interparticle potential. Assuming over-damped dynamics, we show in the Chapter Appendix section 3.4.5 that the effective potential of mean force between the two particles, in the limit that the driving force is large, is simply the potential of mean force of the undriven system averaged over the entire ring. In other words, in the high drive limit the effective potential is the average of the modulated potential [138] and thus the driving force reduces the well depths and barriers in the modulated potential. Therefore, the variance of the probability distributions of the particles is determined by an effective force constant $k_{\text{eff}} = (k_{\text{min}} + k_{\text{max}})/2$ where, k_{min} and k_{max} are the minimum and maximum force constants of the modulated (assumed) harmonic interparticle potential.

However, Figure 3.5 indicates that the optical drive force that any particle in the ring vortex experiences is also modulated for linearly polarized incident light. The modulation in the optical drive force comes from asymmetry in the optical gradient while the optical binding interactions (Figures 3.7-3.8) are altered by their orientation with respect to the direction of linear polarization. The effects of both kinds of force modulations, *i.e.* modulation in optical binding and optical driving force, are combined in the probability densities obtained from experiments and the ED-LD simulations and therefore cannot be used to identify the dominant mechanism that leads to the increase in fluctuations (*i.e.* increase in the effective temperature).

In order to separate the effects of the modulated optical binding and the modulated optical drive forces, we perform 1D Langevin dynamics (LD) simulations with periodic boundary conditions and impose a sinusoidal variation in the modulation of both the binding and drive forces. We assume a harmonic potential for optical binding and use the maximum and minimum force constants from the full ED-LD simulations for $l = 0$ shown in Figure 3.8d. Optical binding forces result from the interactions of the incident and the scattered fields and depend on the wavelength and intensity of the beam, and size of the particles. The size and intensity of the optical ring vortex does not depend on the value of l, therefore, optical binding forces can be assumed to be independent of l. The optical drive forces for different l are extracted from full ED-LD simulations of a single nanoparticle in the trap. The 1D Langevin equation, the optical drive force, F_{d}, and optical binding force, F_{b}, for the i-th particle in these simulations are

$$m\frac{d^2\theta_i}{dt^2} = F_{\mathrm{d}}(\theta_i) + F_{\mathrm{b}}(\theta_i) - \lambda\frac{d\theta_i}{dt} + \eta, \tag{3.3}$$

where θ_i is the position of the i-th particle, λ is the Stokes drag friction coefficient, η is the stochastic thermal noise. The optical forces are:

$$F_{\mathrm{d}}(\theta_i) = (F_{\max} - F_{\min})\sin^2(\theta_i) + F_{\min}, \tag{3.4a}$$

$$F_{\min} = l(1.5 \times 10^{-12}\,\mathrm{N}), \tag{3.4b}$$

$$F_{\max} = 2F_{\min}, \tag{3.4c}$$

$$F_{\mathrm{b}}(\theta_i) = -\frac{d}{d\theta_i}U_{\mathrm{b}}(\theta_i), \tag{3.4d}$$

$$U_{\mathrm{b}}(\theta_i) = k(\theta_c)(\theta_i - \theta_j - \theta_{\mathrm{b}})^2, \tag{3.4e}$$

$$k(\theta_c) = (k_{\max} - k_{\min})\cos^2(\theta_c) + k_{\min}, \tag{3.4f}$$

where $k_{\max} = 3 \times 10^{-6}\,\mathrm{N\,m^{-1}}$ and $k_{\min} = 0.25k_{\max}$ are the force constants, $\theta_c = (\theta_i +$

$\theta_j)/2$ is the center of mass position of the two particle system, and θ_b is the separation corresponding to the first optical binding site (0.6 µm).

We perform the 1D LD simulations with two nanoparticles by assuming a modulated optical binding force but keeping a constant optical drive force, and by modulating both the binding and driving forces. The results are shown in Figure 3.9a and 3.9b, respectively. In the simulations with a constant driving force but modulated binding forces, we find that the effective force constant obtained from the probability distributions is the average of the maximum (at locations of 0 and π) and minimum (at locations of $\pi/2$ and $3\pi/2$) force constants for larger driving forces. However, the probability densities do not change appreciably with increasing l for the values of force constants (k_max, k_min) extracted from our ED-LD simulations. On the other hand, by including a modulating driving force in the 1D LD simulations, we find that the probability densities broaden with increasing l and a two-peaked distribution emerges for very large drive ($l = 50$). This result is reminiscent of the changes in the probability densities and pmfs of Figure 3.8. We illustrate the drive-force-induced modulation in Figure 3.14. The interparticle separations are modulated more strongly at large l for a modulated optical drive force, illustrating the origin of the increasing breadth of the probability density function of Figure 3.9b. These LD simulations combined with the analytical theory explain that the rise in effective temperature of the system with increasing l stems from the modulation in the optical driving force that is inherent to the linearly polarized beam.

The increase in the interparticle fluctuations and single particle dynamics due to the modulated drive force is reminiscent of the topic of enhanced or giant diffusion [139–143]. However, our study concerns force modulation as opposed to constant drive over a periodically modulated potential as first proposed by Hänggi and co-workers [144]. Therefore, although the isomorphism may seem clear, we foresee subtleties that will be addressed in a separate publication.

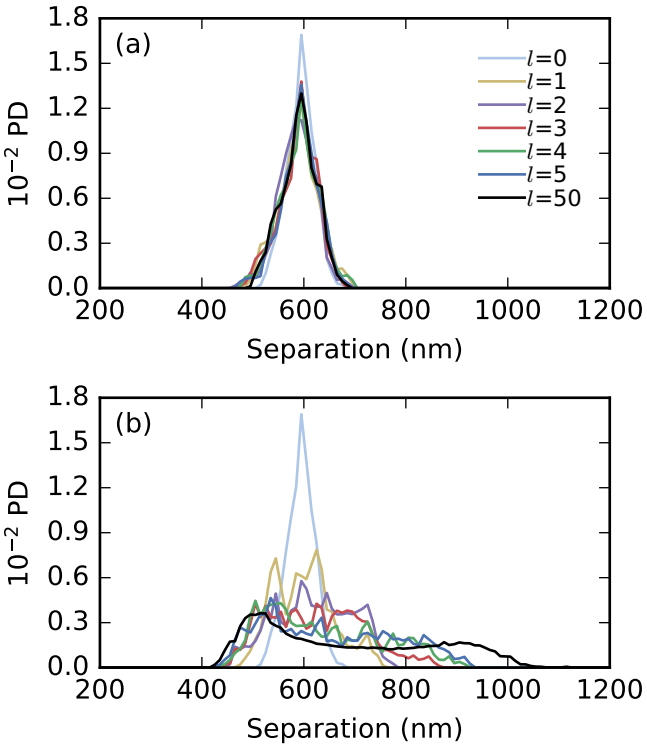

Figure 3.9: Interparticle separation probability density (PD) functions affected by periodic modulation of (a) interparticle potential or (b) drive force. 1D LD simulations with periodic boundaries of two particles using parameters extracted from the full ED-LD simulations assuming (a) constant drive and modulated interparticle potential and (b) modulated drive and interparticle potential.

3.2.6 *Optical Binding in Driven Dielectric Colloids*

We also considered whether electrodynamic interactions (*i.e.*, optical binding) are significant for dielectric (polystyrene) particles trapped using the same optical ring vortex. The large peak in the probability density at a separation of 0.6 µm for the 300 nm polystyrene particles in Figure 3.10a and another peak at a separation of 1.2 µm corresponding to the second optical binding site for particles oriented perpendicular to the polarization is a strong indication of optical binding. The inset in Figure 3.10a shows the difference of the perpendicular and parallel distributions of the nearest neighbor separations, which exhibits characteristics of optical binding seen in Ag nanoparticles over glass (Figure 3.10b) such as a broader and smaller amplitude parallel peak and the emergence of the optical binding at 1.2 µm.

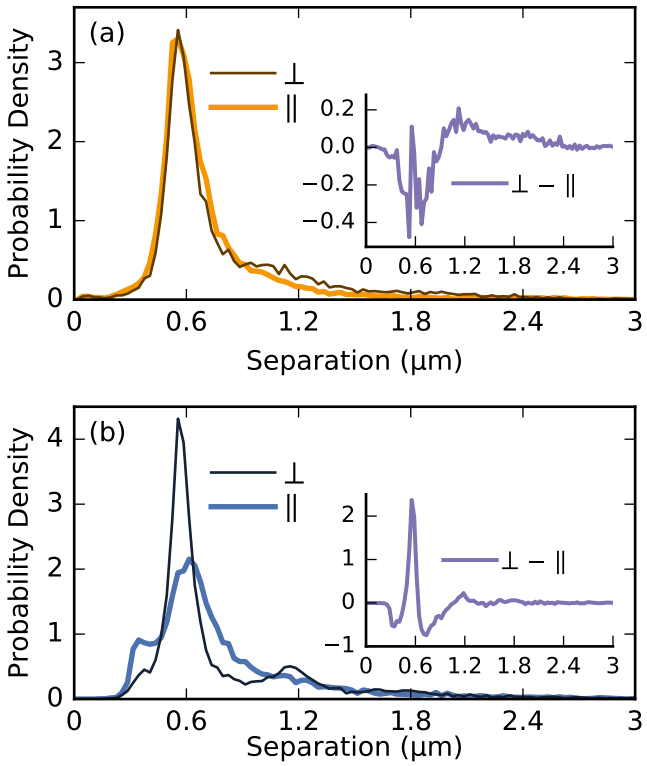

Figure 3.10: Distributions of nearest-neighbor separations. (a,b) Probability densities of interparticle separation for (a) 300 nm polystyrene particles in the optical ring vortex over glass at $l = 1$ for both parallel and perpendicular positions in the ring and (b) Ag nanoparticles over glass for small l (same as Fig 7a). The insets for (a) and (b) show the difference (perpendicular minus parallel) of the respective distributions.

3.3 Conclusions

We have examined the properties of driven optical matter composed of metal nanoparticles in a optical ring vortex. The creation of a superior optical ring vortex by retroreflection from a Au nanoplate mirror is a technical advance that allows trapping particles in an interference antinode above the Au surface. The interferometric trap improves the axial tightness of the trap while also increasing the optical force on the nanoparticles and has reduced hydrodynamic friction as compared with particles that are moving in a vortex trap near a glass surface. Using 150 nm Ag nanoparticles in the optical ring vortex, we demonstrated in experiment and simulation that the optical drive force around the ring vortex trap is inherently modulated for a linearly polarized beam. This modulated force affects the interparticle interactions so as to increase the noise (or effective temperature) and effectively weaken the long-range attractive optical binding interactions.

We developed a model system and simulations showing that the increase in effective temperature (or fluctuations in interparticle separations) results mainly from the modulation in the optical drive force associated with the linear polarization of the incident beam. These electrodynamic forces and interactions in optically driven systems are often not considered in studies of hydrodynamically interacting driven colloidal systems. While the optical binding interactions may not dominate the interactions between larger dielectric particles, we want to encourage the understanding of their existence in these types of driven optical systems. Moreover, the modulation in the electrodynamic driving force that is inherent in a linearly polarized optical ring vortex will affect the interactions between colloidal particles currently ascribed to be solely due to hydrodynamic interactions [67] and is the dominant cause of persistent oscillatory dynamics of optically driven systems [95]. Finally, the modulation of the optical drive force that we study here and the significant increase in noise with drive force that we find in experiment and explain *via* simulations and theory bears strong resemblance to the topic of "enhanced diffusion" [139–143]. We plan to address this topic in detail in a separate publication.

3.4 Chapter Appendix

3.4.1 Methods

Experimental

The experiments were performed using dark field microscopy with optical tweezers. Sample cells were mounted on an inverted microscope (Olympus IX71) and imaged through a 60x water immersion objective (Olympus UPLSAPO). Magnification was further increased with both a 2x and 1.6x expansion lenses. The optical tweezer was created using a linearly polarized Gaussian beam ($\lambda = 800\,\text{nm}$) from a Ti:sapphire laser that is shaped by a spatial light modulator (Hamamatsu X10468-02) to generate vortex ring traps of varying azimuthal phase gradients. Images of the trapped nanoparticles were recorded with an array detector (Andor Neo sCMOS DC-152Q-C00-F1) at a frame rate of 90 frames/sec with an exposure of 0.4 ms

Sample cells were created by sandwiching a 180 µm silicone rubber spacer between two coverslips. A solution of Au nanoplates are drop cast onto the coverslip inside a cutout of the spacer. A diluted solution of spherical Ag nanoparticles ($150 \pm 9.6\,\text{nm}$ diameter, nanoComposix) is placed inside the cut out of the spacer and another coverslip is placed over it creating a sealed sample cell. The sample cell is oriented such that the coverslip with the Au nanoplates is on top and the objective images through the bottom coverslip. This allows the laser to push particles to the top surface by the scattering force where particles can be trapped near the top surface over glass or a nanoplate mirror. However, due to electrostatic repulsion between the particles and the glass the particles do not touch the glass (or Au surface) and instead are repulsively trapped by the opposing scattering and electrostatic forces. A phase gradient encoded in the spatial light modulator controls the angular force applied to the particles in the ring trap.

The nanoparticle positions and trajectories are extracted from the images using the Mo-

saic Suite ImageJ plugin [72]. A kernel radius of 6 pixels with a 0.05 percentile threshold for the brightest maxima is used for particle localization. A large max displacement of 150 pixels between frames was used for linking particle positions into trajectories. Particle trajectories were checked manually to make sure the particle positions were properly linked between frames.

Numerical

Simulations of one and two Ag nanoparticles in an optical ring vortex trap were performed using coupled electrodynamics-Langevin dynamics (ED-LD) solver that we developed [132]. The ED-LD simulation self-consistently couples the finite-difference time-domain (FDTD) method of solving Maxwell's equations with a splitting-method scheme for integrating the Langevin equation. The optical ring vortex beam is introduced in the simulation using the scattered field technique [145, 146] in which the incident electric field is described in cylindrical coordinates as

$$\vec{E}(\rho,\theta,z) = \hat{x}E_0 J_l(kC_\rho\rho)e^{il\theta}e^{i(kz-\omega t)}. \tag{3.5}$$

Here, $E_0 = \sqrt{2I_0/n\epsilon_0 c}$ is the electric field magnitude and I_0 is the intensity of the beam,l is the number of 0 to 2π angular phase rotations around the ring, J_l is a Bessel function of the first kind of order l. We use the constant C_ρ as an adjustable parameter that is varied in order to keep a constant radius for the beam. The incident magnetic field is calculated from Ampere's law for each time step before updating the scattered fields in the main FDTD calculation. The electrodynamic forces on the Ag nanoparticles are calculated using the Maxwell stress tensor, while the electrostatic forces due to surface charges are calculated using Coulomb's law. The Drude model is used to describe the dispersive Ag nanoparticles using the auxiliary differential equation method [146]. We use the following Drude parameters for Ag, $\epsilon_\infty = 3.045$, $\omega_p = 2.117 \times 10^{15}\,\mathrm{s}^{-1}$, and $\gamma_p = 6.069 \times 10^{13}\,\mathrm{s}^{-1}$.The total force

(electrodynamic + electrostatic) on each nanoparticle is used in the Langevin equation to calculate the nanoparticle trajectories. Since, we are interested in the driven (transverse) motion of the nanoparticles, we only use the transverse forces to simulate their trajectories. We were able to simulate a maximum of $\sim 2\,\mathrm{ms}$ long trajectories with the computing resources available to us. Therefore, in order to generate multiple particle orbits around the ring, we simulate a smaller ($\sim 2\,\mu\mathrm{m}$) diameter optical ring vortex with an electric field intensity that is roughly 30 times that in the experiments. The details of the coupled ED-LD simulation can be found in Sule et al. [132].

3.4.2 The Optical Ring Vortex

Please see Figure 3.11 for the phase masks on the SLM and a schematic of the optical ring vortex.

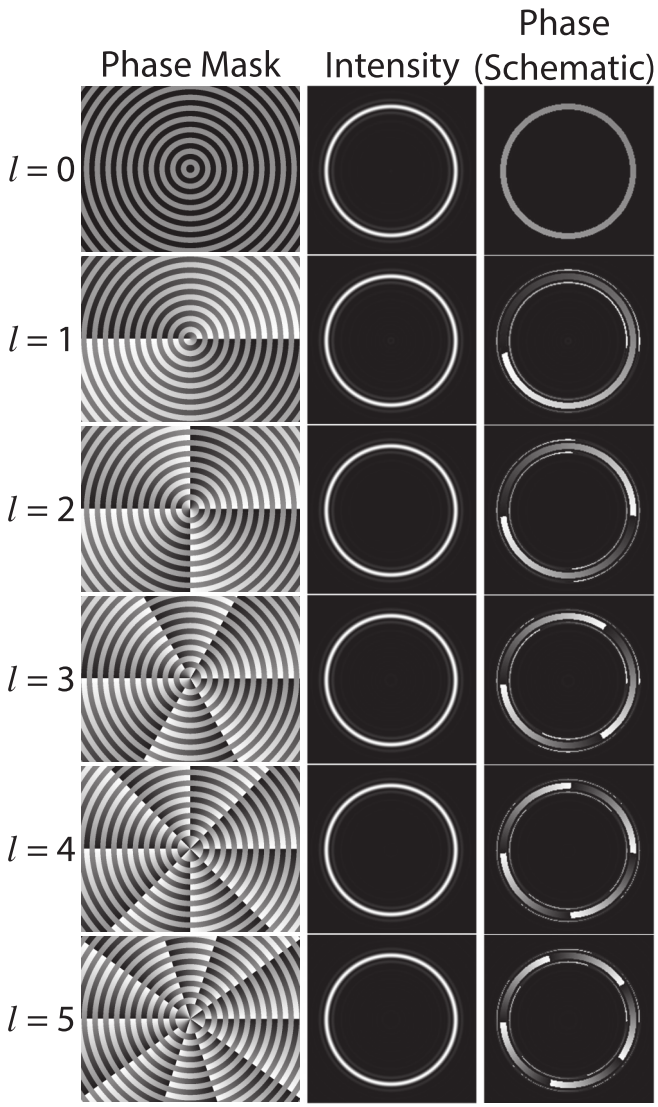

Figure 3.11: Diagram showing the properties of the optical ring vortex for different l's. The first column shows the phase mask used on the SLM to produce the ring trap. The second column shows the intensity of the beam for each l, which is the same for all l's. The third column shows a schematic of the phase of the optical ring vortex for each l.

3.4.3 Electric Field Over the Au Nanoplate

We estimate the electric field over the Au nanoplate from the FDTD simulations. Figure 3.12 shows the electric field intensity in the retroflection geometry over the Au nanoplate mirror discussed in the main text. The electric field intensity is largest 250 nm away from the Au nanoplate surface where the Ag nanoparticles are trapped.

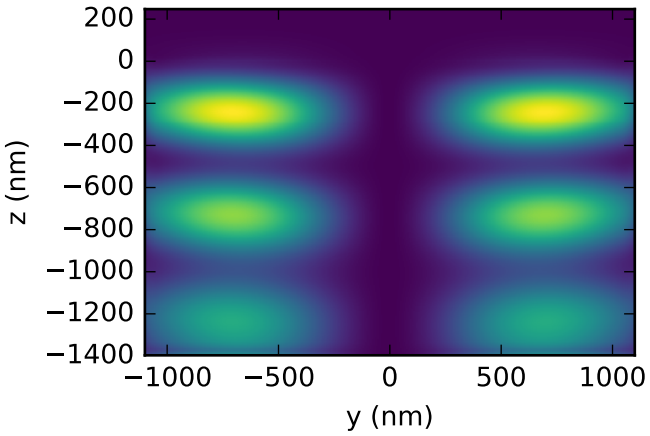

Figure 3.12: The electric field intensity of the optical ring trap over the Au nanoplate shown in the y-z plane bisecting the ring trap. The surface of the Au nanoplate is at 0 nm. The maximum intensity of the first antinode occurs about 250 nm above the Au nanoplate mirror.

3.4.4 Separation of Ag Nanoparticle and Glass Surface

Electrostatic Contribution

DLVO Theory

DLVO Theory uses the idea that the electrostatic interactions are a combination of two competing forces, the van der Waals attractive force and the double layer repulsive forces [147]. These potentials describe all of the electrostatic forces the glass surface and a Ag nanoparticle (in the absence of the optical trapping beam) as a function of their separation d.

$$W(d) = W_{\mathrm{A}}(d) + W_{\mathrm{R}}(d) \tag{3.6}$$

Here, $W_{\mathrm{A}}(d)$ is the potential energy from the attractive van der Waals interaction, $W_{\mathrm{R}}(d)$ is the potential energy from repulsive electrostatic interactions, and $W(d)$ is the total potential energy. The Ag nanoparticle interacting with the glass is treated as a spherical particle interacting with an infinitely flat plate.

Van der Waals Attractive Forces

The nonretarded van der Waals potential energy of a sphere with a surface for all separations is [148]:

$$W_{\mathrm{A}}(d) = -\frac{A}{6}\left(\frac{r}{d} + \frac{r}{2r+d} + \ln\frac{d}{2r+d}\right) \tag{3.7}$$

where A is the Hamaker constant and r is the radius of the sphere. Lifshitz theory treats the objects as continuous materials with bulk refractive index and permittivity. The Hamaker constant for material 1 interacting with material 2 through material 3 as [149, 150]:

$$A = \frac{3\mathrm{k_B T}}{4}\left(\frac{\epsilon_1-\epsilon_3}{\epsilon_1+\epsilon_3}\right)\left(\frac{\epsilon_2-\epsilon_3}{\epsilon_2+\epsilon_3}\right) + \frac{3h}{4\pi}\int_{\nu_1}^{\infty}\frac{(\epsilon_1(i\nu)-\epsilon_3(i\nu))\,(\epsilon_2(i\nu)-\epsilon_3(i\nu))}{(\epsilon_1(i\nu)+\epsilon_3(i\nu))\,(\epsilon_2(i\nu)+\epsilon_3(i\nu))}\,d\nu \tag{3.8}$$

where ϵ_1, ϵ_2, and ϵ_3 are the electric permittivities of material 1, 2, and 3, respectively while $\epsilon_1(i\nu)$, $\epsilon_2(i\nu)$, $\epsilon_3(i\nu)$ are the permittivities at imaginary frequencies $i\nu$ (see Israelachvili [151] for more details), and $\nu_1 = 2\pi\mathrm{k_B T}/h = 3.9\times10^{13}\,\mathrm{Hz}$ at 298 K. The permittivities at imaginary frequencies are calculated differently depending whether the material is dielectric or metallic [151]:

$$\epsilon_{\mathrm{dielectric}}(i\nu) = 1 + \frac{n^2-1}{1-(i\nu)^2/\nu_e^2} \tag{3.9a}$$

$$\epsilon_{\mathrm{metal}}(i\nu) = 1 - \nu_e^2/(i\nu)^2 \tag{3.9b}$$

where n is the refractive index of the material and ν_e is the mean ionization frequency.

Double Layer Repulsive Forces

The potential for the interaction of the double layer repulsion of a sphere with a surface is [152]:

$$W_{\mathrm{R}}(d) = 16e^{-\kappa d}\epsilon r\left(\frac{\mathrm{k_B T}}{ze}\right)^2 \tanh\left(\frac{ze\psi_p}{4\mathrm{k_B T}}\right)\tanh\left(\frac{ze\psi_s}{4\mathrm{k_B T}}\right) \tag{3.10}$$

where ϵ is the dielectric constant of the fluid, r is the radius of the sphere, $\mathrm{k_B T}$ is the thermal energy, z is the ion valency (assuming a symmetric electrolyte), e is the protonic charge, κ

is the inverse Debye length, and ψ_s and ψ_p are the surface potentials of the sphere and the plate, respectively. The surface potential of the glass surface was estimated from an Sze et al. [153] while the surface potential of an Ag nanoparticle was found experimentally through a zeta potential measurement [154]. The parameters used are in equation 3.10: radius, $r = 75\,\mathrm{nm}$, $\epsilon = 80.4$, $\epsilon_0 = 8.85 \times 10^{-12}\,\mathrm{F\,m^{-1}}$, $e = 1.602 \times 10^{-19}\,\mathrm{C}$, $z = 1$, ionic strength, $I = 1.8 \times 10^{-4}\,\mathrm{mol\,L^{-1}}$, $\kappa = 4.4 \times 10^{7}\,\mathrm{m^{-1}}$, $\psi_s = -16\,\mathrm{mV}$, $\psi_p = -77\,\mathrm{mV}$.

Gravity Contribution

The potential energy for gravity in this system decreases as a function of the particle's distance from the plate. This is because of the geometry of the experiment such that the coverslip is above and the particles are pushed up against it. The potential energy of gravity is:

$$W_{\mathrm{g}}(d) = -\frac{4}{3}\pi r^3(\rho_{\mathrm{Ag}} - \rho_{\mathrm{H_2O}})gd \tag{3.11}$$

where $\rho_{\mathrm{Ag}} = 10.5\,\mathrm{g/cm^3}$, $\rho_{\mathrm{H_2O}} = 1.0\,\mathrm{g/cm^3}$, $\mathrm{g} = 9.8\,\mathrm{m/s^2}$.

Laser Contribution

The optical trap contributes two forces to the trapped spherical particle, the scattering force (along the optical axis) and the intensity gradient force. When the particle being trapped is much smaller than the wavelength of light ($\mathrm{R} < \lambda/10$) the Rayleigh approximation holds, which treats the particle as a dipole affected by the electric field. For simplicity we will use the Rayleigh approximation for this calculation even though the particle radius is 75 nm compared to the wavelength in water being $800\,\mathrm{nm}/1.33 \simeq 600\,\mathrm{nm}$.

The scattering force is the result of photons scattering off the particle and imparting momentum to the particle. In the Rayleigh regime the scattering force is [155]:

$$F_{\mathrm{scat}} = n_m \frac{\sigma\langle S\rangle}{c} \tag{3.12}$$

where σ is the particle's cross section defined as:

$$\sigma = \frac{8}{3}\pi(kr)^4 r^2 \left(\frac{n^2-1}{n^2+2}\right)^2 \tag{3.13}$$

and $\langle S \rangle$ is the time averaged Poyting vector. For a plane wave this is:

$$\langle S \rangle = \frac{E_m^2}{2c\mu_o} = \frac{1}{2} E_m^2 \left(c\epsilon_o\right) \tag{3.14}$$

where E_m^2 is the intensity of the plane wave incident on the particle. The intensity can be estimated based on the power entering the microscope divided by the area of laser focus. The laser power is measured to be 112 mW after the SLM but before it microscope objective. The power lost from the objective transmission is estimated from the Olympus website and accounting for overfilling the back aperture. The area the laser illuminates is estimated from the diameter of the ring trap with diffraction limited annular width. For the experiments presented the power density is estimated to be $2.79 \times 10^{-6}\,\mathrm{mW/nm^2}$. The wave vector is $k{=}2\pi/\lambda$ where λ is the wavelength of the laser. Refractive indices for water at 800 nm is $n_{\mathrm{H_2O}} = 1.3290$ [156] and $n_{\mathrm{Ag}} = 0.0368$ for Ag [157]. The potential energy from the laser becomes:

$$W_{\mathrm{scat}}(d) = F_{\mathrm{scat}} \times d \tag{3.15}$$

Total Potential Energy for the Ag nanoparticle Near Glass Surface

The sum of all potentials (from equations 3.7, 3.10, 3.11, and 3.15) gives the full potential energy function of the 150 nm diameter particle.

$$W_{\mathrm{full}}(d) = W_{\mathrm{A}}(d) + W_{\mathrm{R}}(d) + W_{\mathrm{g}}(d) + W_{\mathrm{scat}}(d) \tag{3.16}$$

The potential energy function for the parameters given above is shown in Figure 3.13. The minimum of this function will be the equilibrium position of the Ag nanoparticle near the

glass surface.

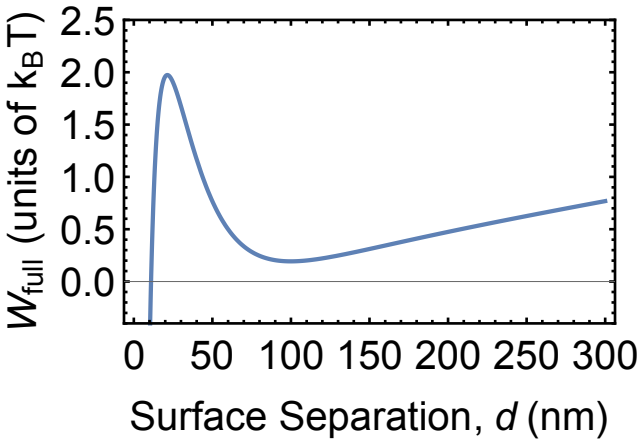

Figure 3.13: The calculated potential energy of a Ag nanoparticle in an optical ring vortex over the glass surface. The minimum is at ∼95 nm, and the barrier for the particle to spontaneously jump and get stuck on the glass surface is $\sim 1.8 k_B T$.

3.4.5 Fluctuations Increase with Increasing Drive Force

We present a series of simple analytical arguments that qualitatively explain increased fluctuations as a function of the driving force. As in the detailed numerical analysis, we imagine a system of two driven particles confined to a ring. The over damped equations for motion of this pair of particles have the form

$$\frac{d\theta_{1/2}}{dt} = v_d - \mu V'(\theta_1, \theta_2) + \eta_{1/2}(t) \tag{3.17}$$

where θ_i denotes the angular location of particle $i = \{1, 2\}$, v_d is the driving force on the two particles, $V'(\theta_1, \theta_2)$ is the optical force of interaction between the two particles and η_i denotes the random noise term. Since we are interested in the potential of mean force for $\theta_1 - \theta_2$, we use Eq. 3.17 to construct equations of motion for $\delta\theta = (\theta_1 - \theta_2)$ and $\theta_{\text{sum}} = (\theta_1 + \theta_2)/2$,

$$\frac{d\delta\theta}{dt} = -2\mu V'(\theta_1, \theta_2) + 2\eta_- \tag{3.18}$$

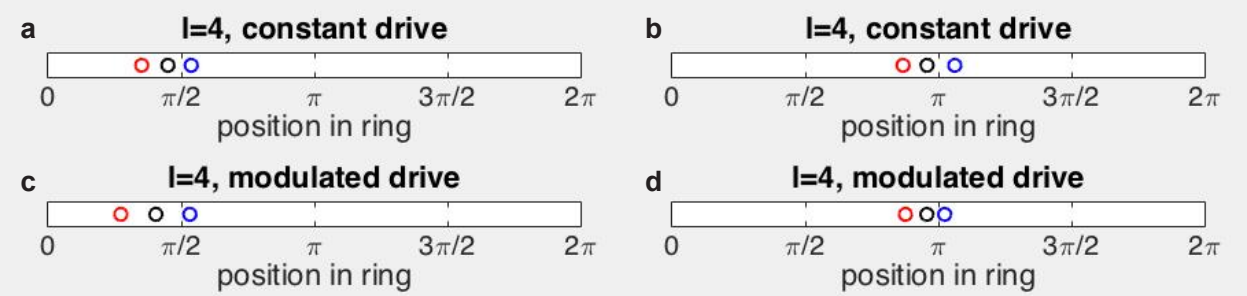

Figure 3.14: Snapshots of the LD simulations for l=4 for (a,b) constant and (c,d) modulated drive forces. Panels (a,b) show the positions of the particles in a constant drive force when the particles are located at $\pi/2$ (a) and π (b). Panels (c,d) show the positions of the particles in a modulated drive force when the particles are located at $\pi/2$ (c) and π (d). The angles correspond to the polar coordinate system used in the main text.

$$\frac{d\theta_s}{dt} = v_d + \eta_+ \tag{3.19}$$

where $\eta_\pm \equiv (\eta_1 \pm \eta_2)/2$ and we have used the fact that the forces on the particles due to the inter-particle potential have opposite signs to derive Eq. 3.18. To proceed, we will make the simplifying approximation that the two particle potential $V(\theta_1, \theta_2)$ depends simply on θ_s and $\delta\theta$, $V(\theta_1, \theta_2) \equiv \tilde{V}(\delta\theta, \theta_s)$.

This set of coupled equations can be simplified further by using the approximation $\theta_s(t) \approx v_d t$. With this approximation, we can view the time dependent two particle system with spatial modulation as a time dependent one particle problem without spatial modulation. This time dependent problem becomes analytically tractable in the limit of high driving force [138]. In this limit, the probability distribution for observing a certain $\delta\theta$ can be simply written as

$$P(\delta\theta) \sim e^{-\alpha \int_0^{2\pi} \tilde{V}(\delta\theta, x) dx} \tag{3.20}$$

The effective potential is simply the average of the potential $\tilde{V}$. This averaging can wash out some of the features of the strong time independent PMF and is the reason for larger fluctuations at higher drives.

1D Langevin Dynamics (LD) simulations are discussed in the main text where the effects of a modulated drive force and interparticle potential were examined as a mechanism for the

increased interparticle separation fluctuations. The changes in the interparticle separations are seen in snapshots of these LD simulations shown in Figure 3.14. For LD simulations where the drive force is constant the relative positions of the particles remains approximately the same regardless of where the particles are located in the ring trap (Figure 3.14a and b). When the drive force is assumed to be modulated the interparticle separations increase (Figure 3.14c) when they are in the ring trap at the $\pi/2$ and $3\pi/2$ positions for high drive. Likewise, the interparticle distances decrease (Figure 3.14d) when they are at the 0 and π positions in the ring for low drive. The interparticle potential is modulated in both simulations. It is clear that the modulation in drive force, as opposed to the modulation of interparticle potential, is the dominant cause of the increase in fluctuations of interparticle separation.

CHAPTER 4

CRITICAL ASSESSMENT OF NONEQUILIBRIUM BARRIER CROSSING PROCESSES USING DRIVEN OPTICAL MATTER

Contributions: Nishant Sule performed the ED-LD and FDTD simulations. Erik Thiede executed the umbrella sampling method to extract the potential mean force. Curtis Peterson developed the inverse Gaussian transport analysis and contributed some additional experimental data.

4.1 Introduction

The kinetics of barrier crossing phenomena are of fundamental importance in Physics, Chemistry, and Biology [46–54]. Studies of barrier crossing in Chemistry typically obtain the rate at which molecules react to form products by surmounting an energy (or free energy) barrier. The transition state, at the barrier top, separates reactants from products. Transition state theory (TST) describes barrier crossing dynamics in the gas phase for frictionless conditions, while Kramers theory is appropriate in frictionally damped environments, *e.g.* in solution [48, 59, 60]. The latter assumes that a parabolic barrier is crossed in a diffusive manner in a canonical ensemble (at equilibrium) where the barrier height $>k_BT$. Kramers theory has been extended to describe the kinetics of barrier crossing when a force or load is applied, providing a relationship between the applied force on a molecule and its rate of mechanical rupture [54, 62]. Applying a force decreases the effective barrier and reduces the distance from the well to the transition state along the reaction coordinate (Figure 4.1). Single molecule force spectroscopy experiments have been used to determine the rate of mechanical unfolding of macromolecules (*e.g.* protein, RNA) using an atomic force microscope or optical laser tweezers suitably linked to the macromolecules [49–51]. The force that drives barrier crossing is mechanical pulling of the molecule and ultimately it's rupture by thermal fluctuations.

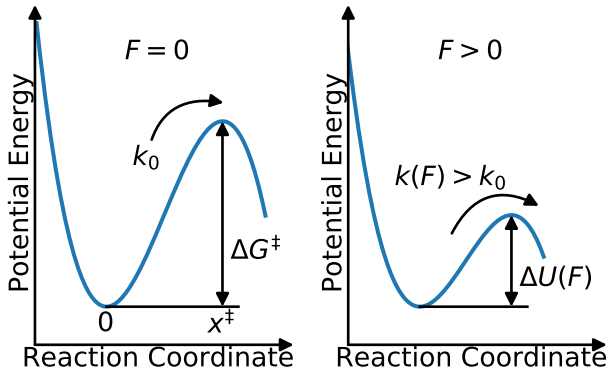

Figure 4.1: Schematic of barrier crossing with visual representation of relevant parameters. The left panel shows an example of an equilibrium barrier with height $\Delta G^{\ddagger}$ and barrier distance of $x^{\ddagger}$. At equilibrium the rate of crossing the barrier is k_0. The left panel shows the same barrier crossing with a force applied in the direction of the reaction coordinate which lowers the height of the barrier to a force dependent height, $\Delta U(F)$, and has a force dependent crossing rate of $k(F)$. The parameters are relevant to the Dudko-Hummer-Szabo model analysis described below. The figure is adapted from [62].

However, single molecule force spectroscopy experiments do not allow critical assessment of the dynamical process as the atoms cannot be visualized and the actual transition state crossing event occurs too rapidly to be followed by the force transduction instruments [158]. Optical tweezers and electrodynamically manipulated nanoparticles provide a new paradigm to study barrier crossing phenomena. Optical trapping can be used to confine and drive nanoparticles through momentum transfer to, and gradient forces on, the particles. Electrodynamic barriers suitable to enable the desired experiments can also be created. Particles that strongly scatter the incident electromagnetic field (*e.g.* Ag nanoparticles) alter the field in their vicinity producing locations of field enhancement that cause other particles to gather at these locations; a phenomena known as optical binding [18, 40]. As shown in Figure 4.2, optical binding and other electrodynamic interactions between metal nanoparticles and also with the Au nanoplate mirror lead to rich energy landscapes (see Figures 4.2c and 4.2d) that allow studying a wide range of phenomena including barrier crossing by single nanoparticles. In an optical trap system several nanoparticles can become optically bound together in a structure, as optical matter, where the motion of one particle influences the motion of all

the other optically bound particles in the system [18, 44, 45, 93, 130, 131]. Thus, experimental conditions that allow controlled scattering of EM fields to create localized fields and field gradients can serve to create electrodynamic energy landscapes while optical trapping and suitable gradient forces allow driving nanoparticles through the energy landscapes, thus making optical matter systems suitable for developing a deeper understanding of barrier crossing phenomena.

In this paper, we trap and drive nanoparticles to study the force-dependence of crossing electrodynamic barriers. The same optical properties used to form optical matter (*i.e.* intensity and phase gradients) [93] can be used to drive particles and optical matter to study non-equilibrium phenomena. Specifically, we use optical ring traps with controlled optical phase gradients to study the effects of applied force on the kinetics of barrier crossing. Although our study is akin to single molecule force microscopy studies, one important distinction is that we directly visualize the particle's motion during the entire barrier crossing process with optical microscopy at high frame rates. Our results allow distinguishing between TST (Bell model) [159] and driven Kramers theory (Dudko, Hummer and Szabo) [62] models of barrier crossing. Finite-difference time-domain (FDTD) and electrodynamics-Langevin dynamics (ED-LD) simulations [93, 132] are performed to model the shape of the electrodynamic barrier and the driven Brownian dynamics of the nanoparticles. The potentials of mean force obtained do not agree as closely as expected with our experimental results. We conclude that the experimental results reflect a combination of activation and non-diffusive transport thus violating the assumptions of Kramers theory. Therefore, the distribution function and trajectory information we obtain calls for the development of a comprehensive theory that includes deterministic transport through the barrier region.

4.2 Results and Discussion

Recently, we characterized the trapping and dynamics of metal nanoparticles in an optical ring vortex over glass and Au nanoplate surfaces [93]. The present study builds directly

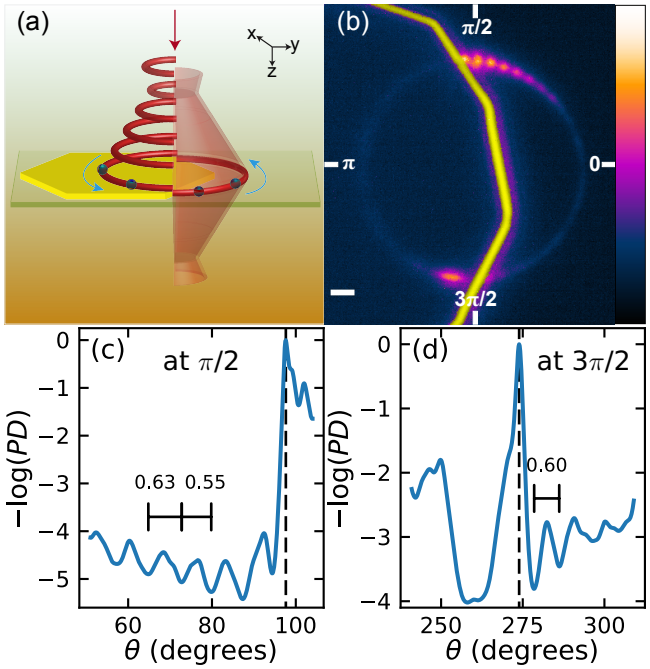

Figure 4.2: Schematic of the experiment and results of Ag nanoparticles driven in a ring trap that straddles a Au nanoplate mirror. (a) Schematic of the focused optical beam and ring trap half over a glass coverslip and half over a Au nanoplate. Antinodes of intensity arise over the Au nanoplate due to interference. (b) Colorized time average intensity for the "half nanoplate" experiment for $l = 1$. The yellow line segments are the edge of the Au nanoplate while the purple-orange colormap shows the time averaged intensity of the nanoparticles. The colorbar scale (right) shows the intensity in counts from 94–152 and the white scale bar in the bottom left corner is 1 µm. The leading edge of the Au nanoplate near the $\pi/2$ position of the ring shows a periodic pattern that is the result of electrodynamic interactions (*i.e.* optical binding) between nanoparticles and the edge of the nanoplate. (c) The $-\log(PD)$ (probability density) of the nanoparticles at the leading edge of the Au nanoplate (at $\pi/2$) and (d) at the falling edge (at $3\pi/2$) calculated along the arc of the optical ring vortex as a function of angular position in degrees. The black annotations in (c) and (d) show the distance (µm) along a chord of the optical ring vortex between pairs of select peaks in the $-\log(PD)$. The spacings agree with the separation expected from optical binding [44, 93]. The dashed vertical lines in (c and d) are the locations of the edges of the nanoplate.

on this earlier work (presented in Chapter 3). An electrodynamic barrier is created by producing an optical ring vortex trap [44, 89, 93] that spans a Au nanoplate mirror [131] and a glass coverslip (Figure 4.2a) with a focal condition that provides suitable trapping over both surfaces. 150 nm Ag nanoparticles are trapped and driven around the optical ring with a drive force produced by phase gradients in the azimuthal direction determined by the topological charge, l, of the vortex [89]. Once the particle hops onto the Au nanoplate it is driven by the optical ring and travels to the edge of the Au nanoplate where the electrodynamic barrier exists. Evidence of the electrodynamic barriers can be seen as enhanced intensity at the $\pi/2$ and $3\pi/2$ locations in the integrated sequence of images in Figure 4.2b. We establish the trajectories of the particles as they are driven in the optical trap by particle tracking analysis of the microscopy (imaging) data (see Chapter Appendix). The trajectories are used to calculate probability densities, dwell times, and the forces on individual nanoparticles. The negative logarithm of the probability densities near the edge of the nanoplate show troughs and peaks (*e.g.* see the region near the dashed line in Figures 4.2c and 4.2d) corresponding to the electrodynamic barriers. The large barrier and resulting accumulation of particles at the leading edge of the Au nanoplate (*i.e.* the $\pi/2$ position) prevents a large number of nanoparticles being over the Au nanoplate at any time. That allows us to study the barrier crossing of single nanoparticles on the falling edge of the Au nanoplate (*i.e.* the $3\pi/2$ position). This chapter focuses on barrier-crossing phenomena occurring near the falling edge of the Au nanoplate mirror as this deals with the simple case of a single particle process.

Numerical simulations that combine electrodynamics and Langevin dynamics methods, termed ED-LD [93, 132], are used to characterize the electrodynamic barrier and examine single Ag nanoparticle barrier crossing dynamics. The simulations focus on a short arc (subtending an angle of 25°) about the falling edge of the Au nanoplate where the relevant barrier-crossing dynamics occur. We assume that the curvature of the arc is negligible for the dynamics as shown in Figure 4.3a and that the edge of the Au nanoplate is perpendicular to the optical trap. Thus, we simulate a line trap that is partially over a Au nanoplate of

200 nm thickness placed on a glass substrate such that reflections from the Au nanoplate result in a standing wave perpendicular to the surface, as shown in Figure 4.3a. The phase gradient within the line trap corresponds to the experimental phase gradient in the short arc near the falling edge. Field enhancement associated with the edge of the nanoplate affects the intensity of the antinode near the edge (see Figure 4.3a). The non-uniform intensity creates a (gradient) force on the Ag nanoparticle, pulling it towards the region of highest intensity. It is this intensity maximum that corresponds to the potential energy well. The electrodynamic barrier is, in turn, a region of lower intensity near the nanoplate edge and a correspondingly greater potential energy.

The optical force on a Ag nanoparticle in the first antinode shown in Figure 4.3b indicates that the electrodynamic barrier occurs between -400 nm and -200 nm from the edge of the Au nanoplate. The difference between the optical force in traps with drive (non-zero l) and the un-driven trap ($l = 0$) is plotted as an inset in Figure 4.3b showing that the shape of the barrier changes with drive. A typical trajectory of a single Ag nanoparticle crossing the edge, determined from ED-LD simulations, is superimposed on the first antinode shown in Figure 4.3a. The optical force along the trajectory is shown in Figure 4.3c for different values of l; the particle is unable to cross the barrier for low drives (l=0,1,2) and remains stuck in the potential well of the electrodynamic barrier on the timescale of the simulation.

We calculate the rate of particles crossing the barrier in the experiments from the distribution of dwell times for each l. Using the particle's angular position as the reaction coordinate, the dwell-time distribution, $P_{\mathrm{D}}(t)$, is calculated from the number of frames a particle takes to cross over the edge of the Au nanoplate after entering a region before the edge (see Chapter Appendix for details). The decay of the cumulative dwell time, $\mathrm{CDT} = 1 - \int_{-\infty}^{t} P_{\mathrm{D}}(t')dt'$, is fit with an exponential decay function, Ae^{-kt}, where k is the rate of particles crossing the barrier (Figures 4.4a-c). The particle velocities measured over the Au nanoplate (away from the edges) are used in conjunction with Stokes Law to calculate the average optical force on each Ag nanoparticle (See Chapter Appendix for details). We find that the distributions of

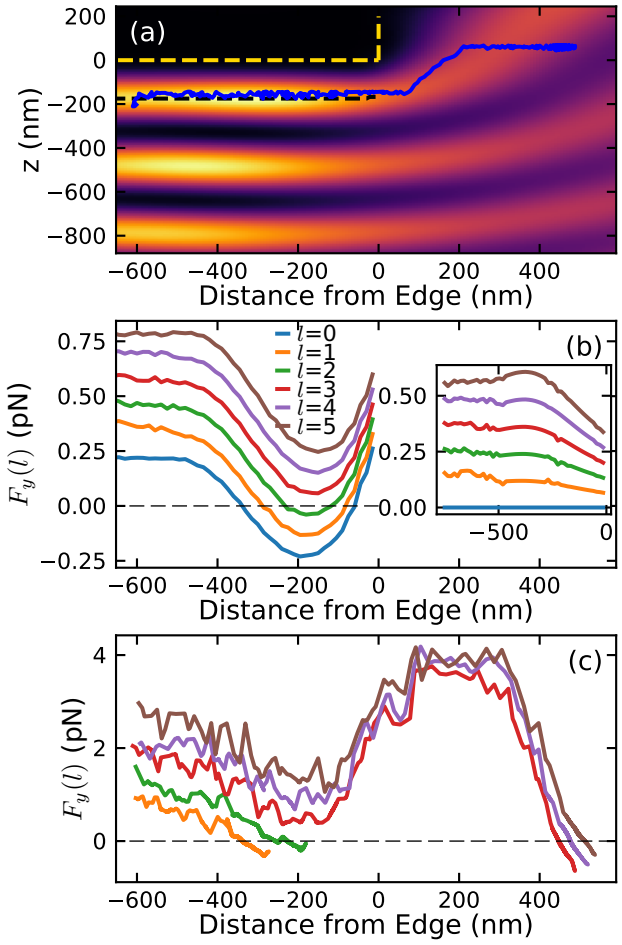

Figure 4.3: Electrodynamics and Langevin dynamics (ED-LD) simulations of Ag nanoparticles traversing the edge of a Au nanoplate. (a) The electric field intensity calculated from FDTD simulations in the z-y plane for a line trap incident centered at the edge of a Au nanoplate (the optical beam propagates along z). The Au nanoplate surface is at 0 nm in z (yellow dashed line) and the falling edge of the Au plate is at 0 nm (horizontal scale). Dashed black line indicates the positions of maximum electric field intensity along the z-axis in the first antinode over the Au nanoplate mirror. Blue line is a trajectory of a nanoparticle crossing the electrodynamic barrier for $l = 4$ in the ED-LD simulation. (b) The y-axis component of the optical force on a nanoparticle calculated from FDTD simulations along the black dashed line in (a) for different l's. The inset in (b) shows the net optical force on a nanoparticle, $F_y(l \neq 0) - F_y(l = 0)$. (c) The optical force acting on a nanoparticle along its trajectory from ED-LD simulations (*e.g.* the blue curve in panel (a) for $l = 4$) for different l. The force curves are smoothed with a Gaussian weighted average with a full width half maximum of 12 nm.

applied force broaden and the mean force increases with l (Figures 4.4d-f) as does the rate of particles crossing the barrier.

We draw an analogy between the present study and single-molecule pulling experiments where the rupture rate of a molecule increases with the applied force [49–51]. The simplest model for a force-dependent barrier crossing rate was presented by Bell [159] and Evans and Ritchie [160]:

$$ln[k(F)] = ln(k_0) + \frac{x_b}{k_b T} F, \tag{4.1}$$

which predicts a linear relationship between the applied force, F, and the logarithm of the rate, $k(F)$. The linear approximation is only valid for barriers $\gg \mathrm{k_B T}$. The Bell-Evans (BE) model is essentially a transition state theory picture where $\int F \cdot dx$ is subtracted from the force-independent potential energy function. The rate of barrier crossing at equilibrium in the absence of applied force, k_0, and the distance from the well to the barrier, x_b, can be obtained by extrapolation of the BE model fit to $F = 0$. We fit our experimental electrodynamic barrier crossing data to the BE model in Figure 4.4g (red dashed line) obtaining $x_b = 120\,\mathrm{nm}$ and $k_0 = 0.63\,\mathrm{s}^{-1}$. However, the distance, x_b, is much smaller than what we estimate from the simulation in Figure 4.3c.

A Kramers theory based model by Dudko et al. [62] (DHS model) provides a more detailed treatment of the rate of barrier crossing in the presence of an external force, F,

$$k(F) = k_0 \left(1 - \frac{\nu F x^{\ddagger}}{\Delta G^{\ddagger}}\right)^{\frac{1}{\nu}-1} e^{\beta \Delta G^{\ddagger}[1-(1-\nu F x^{\ddagger}/\Delta G^{\ddagger})^{1/\nu}]} \tag{4.2}$$

where $x^{\ddagger}$ is the distance from the lowest point in the well to the transition state ($\Delta G^{\ddagger}$) and ν describes the shape of the barrier; $\nu = 1/2$ corresponds to a cusp free-energy surface while $\nu = 2/3$ corresponds to a linear-cubic free energy surface. The DHS model fit with $\nu = 1/2$, $x_b = 251\,\mathrm{nm}$, the equilibrium rate $k_0 = 0.22\,\mathrm{s}^{-1}$, and $\Delta G^{\ddagger} = 7.3\,\mathrm{k_B T}$ is in excellent agreement with the experimental data.

Analogous to single-molecule pulling experiments [51, 161, 162], we find that there is a

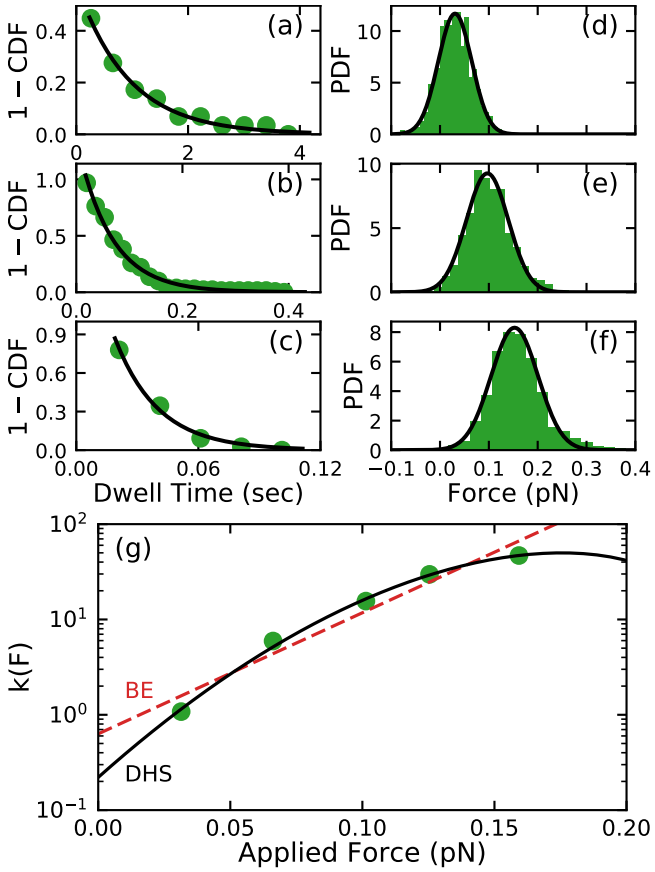

Figure 4.4: Rates, forces, and model fitting to driven nanoparticle barrier crossing results. (a-c) Cumulative dwell time distributions of Ag nanoparticles crossing from 230 degrees to past the maximum of the $-\log(PD)$ (see Figures 4.2b and 4.2d) for (a) $l = 1$ (b) $l = 3$ and (c) $l = 5$. The solid black lines are exponential fits of the decay of the cumulative dwell time distributions. (d-f) distributions of optical drive force on all Ag nanoparticles in the optical ring trap determined from their speeds over the Au nanoplate for (d) $l = 1$ (e) $l = 3$ and (f) $l = 5$. Solid black lines in (d-f) are Gaussian fits to the force distributions. (g) Rate of Au nanoplate barrier crossing as a function of the applied force in the ring trap. The dashed red line shows the fit using Bell-Evans model and the solid black curve shows a fit using the Dudko-Hummer-Szabo theory of barrier crossing for $\nu = 1/2$; *i.e.*, the potential energy surface of the barrier is assumed to be cusp shaped.

large enhancement in the force-dependent rate, $k(F)$, compared to the calculated equilibrium rate, $k(0)$. The enhancement factor is 10^2 for the experiments presented here and 10^3–10^6 in some typical the single-molecule pulling experiments [51, 161, 162]. Therefore, our non-equilibrium or driven barrier-crossing experiments are in the same out of equilibrium regime as typical single-molecule pulling experiments (see Chapter Appendix for details).

The relative simplicity of the driven single Ag nanoparticle experiments as compared to single-molecule pulling measurements and the direct visualization of particle motion allows us to obtain more insight into the dynamics of non-equilibrium barrier crossing. The negative log of the probability density (PD) of particle positions obtained from microscopy shows a barrier close to the Au nanoplate edge (see Figure 4.5a) whose height decreases as the drive force is increased. We also obtain $-\log(PD)$ using the trajectories from the ED-LD simulations as shown in Figure 4.5b (solid lines) and find very good agreement with experiments (dashed line in Figure 4.5b).

However, upon more careful consideration of the nonequilibrium experiment and simulation, one realizes problems with the interpretation of the results. The probability densities obtained from the experiments as well as the simulations suffer from sampling errors after the barrier *vs* before; the particles move very quickly after crossing the barrier and nanoplate edge due to the strong radiation pressure. Therefore, in order to obtain the equilibrium barrier without these sampling errors, we employed an umbrella sampling method [163, 164] to recover the potentials of mean force (pmf), shown in Figure 4.5c for various drives along the reaction coordinate (see Chapter Appendix for details). We find that at $l = 0$, the nanoparticle encounters a $\sim$10 k_BT barrier and the free energy barrier decreases in height as the optical drive (*i.e.*, l) is increased. More importantly, the pmfs in Figure 4.5c reveal that the barrier is only present for low drives ($l = 0$–2) and becomes small or non-existent for higher drives ($l > 2$). Furthermore, as shown in Figure 4.5d, the sampling error and the resultant apparent barrier in the $-\log(PD)$ representations can be clearly seen when compared with the pmf determined from umbrella sampling; the barrier is located before the Au nanoplate

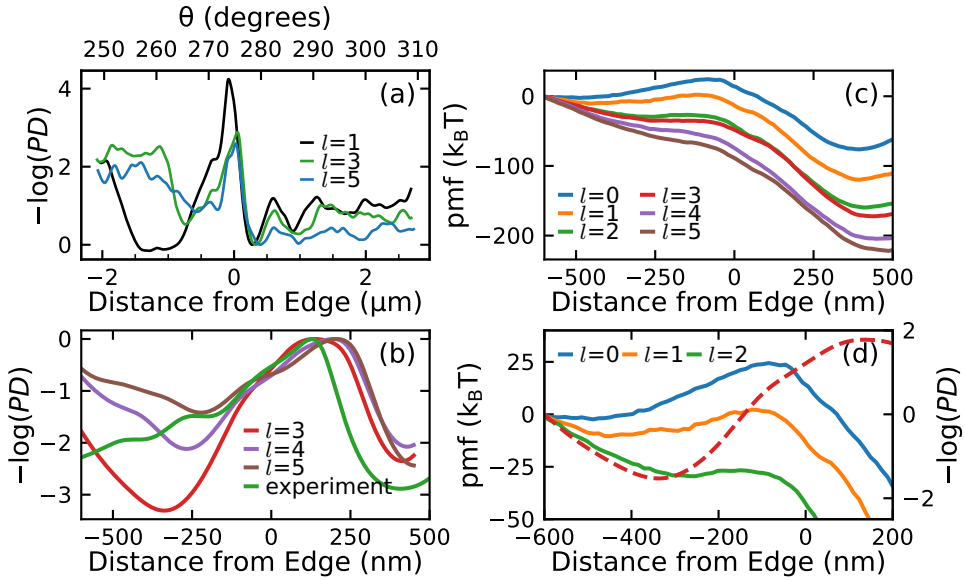

Figure 4.5: Comparison of non-equilibrium $-\log(PD)$ (Probability Density) and potentials of mean force from driven dynamics. (a) $-\log(PD)$ obtained from the experimental single-particle trajectories for $l = 1$, 3, 5. The bottom horizontal axis shows the distance from the edge of the nanoplate as an arc along the ring while the top axis shows the angular position in the ring. (b) $-\log(PD)$ calculated from ED-LD particle trajectories for $l = 3$–5. The green curve is the $-\log(PD)$ from the experiment for $l = 3$ shown in (a). (see Chapter Appendix for for determination of the Au nanoplate edge in the experiment) (c) Potentials of mean force (pmf) calculated from umbrella sampling ED-LD trajectories for $l = 0$–5. (d) Potentials of mean force calculated from umbrella sampled ED-LD simulations for $l = 0$–2 (left axis) and $-\log(PD)$ calculated from the trajectory in the ED-LD simulation for $l = 3$ (right axis, same as red curve in (c)).

edge in the pmf while the peak in the $-\log(PD)$ occurs after the edge.

Although we cannot interpret the apparent barriers obtained from statistical $[-\log(PD)]$ analysis as real physical barriers, the kinetic data of Figure 4.3 are valid. However, a naive interpretation of the rates must be modified to allow for transport in the barrier region. Assuming that the distribution of transport times, $P_{\text{trans}}(t)$, and barrier crossing times, $P_{\text{waiting}}(t)$, are independently distributed, the total dwell time distribution is given by a convolution

$$P_{\text{D}}(t) = \int_{-\infty}^{\infty} P_{\text{waiting}}(\tau) P_{\text{trans}}(t-\tau) d\tau \tag{4.3}$$

Since the distribution of average velocities (hence forces) over the Au nanoplate away from the edges is Gaussian, $P_{\text{trans}}(t)$ is distributed as an inverse Gaussian. Figure 4.6a shows a simulated convoluted dwell-time distribution, and Figure 4.6b shows a pure travel time distribution. The simulated $P_{\text{D}}(t)$ can be created by

$$t_i^{\text{D}} = t_i^{\text{trans}} + t_i^{\text{waiting}} = \frac{d}{v_i} + t_i^{\text{waiting}}, \tag{4.4}$$

where v_i is drawn from a Gaussian distribution, d is a constant travel distance, and t_i^{waiting} is drawn from an exponential decay distribution. The two distributions look very similar; after a sharp rise, both distributions are well-fit by an exponential decay. These surprising results suggest that the DHS model analysis fits the data even past the critical force where the barrier has disappeared completely and the process becomes deterministic. The statistical signature of a barrier crossing process when transport becomes completely negligible *i.e.* $P_{\text{trans}}(t) \to \delta(t)$ is nearly identical to an inverse Gaussian – transport only – process. When waiting times and transport times are comparable, the convolution of the two distributions obscures the exponential rate constant associated with barrier crossing. The actual rate constant in Figure 4.6a was $285\,\text{s}^{-1}$, while the measured rate constant from exponential fitting was $313\,\text{s}^{-1}$, a difference of 10 The distribution in Figure 4.6b, which contained no exponential process, but the same transport distribution in Figure 4.6a yielded an exponen-

tial decay constant of $541\,\mathrm{s}^{-1}$. Figure 4.6c shows an experimental dwell-time distribution taken from data in the high driving force regime (*i.e.* where no barrier remains) along with a simulated pure travel time distribution in which the velocity distribution was obtained from the experimental data as described before. The close agreement of these two results indicates that when the driving force is greater than the critical force, the measured dwell time distribution, which is only associated with transport, can be readily mistaken as a rate process. In fact, an exponential fit yields a decay constant that is reasonable compared to the rate constants extracted in the lower drive regime where waiting times are significant.

4.3 Conclusions

The results of our experiments, simulations, and their analysis yield some important observations and conclusions. In our experiments there is a cross-over from thermal activation and diffusive barrier crossing in the low driving force regime to drift-dominated transport through the barrier region in the high drive (high force) regime; *i.e.*, where the driving force overcomes the barrier completely. Both our driven single Ag nanoparticle experiments and many single-molecule force-spectroscopy measurements as exemplified by Nome et al. [51], Dudko et al. [161], and Garcia-Manyes et al. [162], are far from equilibrium and in part or in total in the limit where no barrier exists at all (see Chapter Appendix for details). We conclude that the rate and dynamics of barrier crossing in the two limiting regimes are due to distinct and disparate processes. In the vanishingly small barrier (high force) limit, the mean first-passage time over the barrier region is determined by deterministic transport (drift), with an inverse Gaussian form, while in the high barrier limit it is the result of a stochastic process controlled by the barrier height. The DHS model, which is based on the Smoluchowski limit of the Fokker-Plank formulation of Kramers theory, assumes diffusive barrier crossing [62]. However, the model is applied and has been applied even in the high-drive regime [51, 161, 162]. Despite our data spanning disparate regimes of driving forces, the DHS model provides an excellent fit for our experimental results making it difficult to

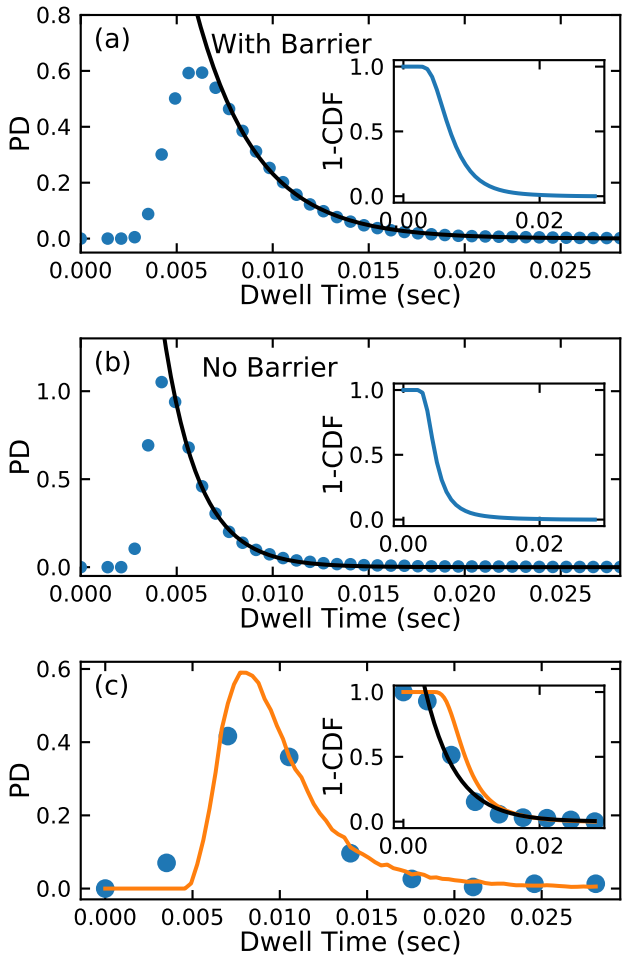

Figure 4.6: Similarity of waiting time and dwell time distributions in simulated barrier crossing and pure transport processes. (a) Convoluted exponential waiting time distribution determined by equation 4.4 with k =285 s^{-1} with a travel time distribution with region size 0.58 µm, mean velocity 123 µm s^{-1} and standard deviation of 0.14 µm. Exponential fitting yields a rate constant of 313 s^{-1}. (b) Pure travel time distribution with parameters identical to (a). (c) Dwell time distribution (dots) from experiments for highly driven Ag nanoparticles with a superimposed simulated travel time distribution obtained from a Gaussian velocity distribution and region size taken directly from experiment (*i.e.* no fitting parameters).

asses the validity of the parameter values obtained.

Our experimental and simulation results call for a re-examination of the interpretation of driven barrier-crossing process. Caution is warranted in the interpretation of non-equilibrium barrier-crossing measurements since, as we have shown, the rate constants commonly extracted from models based on Kramers theory have an entirely different meaning in the high-drive regime. The issue of high loading rate and deviations from Kramers theory has

been explored in single molecule pulling experiments [165]. Although the theory in Bullerjahn et al. [165] assumes a force term that is time dependent, it lacks a direct relationship between the rate of the reaction and the applied force. A more general understanding of the barrier-crossing process should included transport over the barrier as considered by Szabo et al. [166], in addition to thermal activation that would unify the results obtained from the wide range of nonequilibrium conditions accessible in such experiments. Belousov et al. [167], have recently addressed such a process in a drift-diffusion Langevin equation of motion but have not explicitly treated barrier crossing. We anticipate driven optical matter experiments to facilitate these developments.

4.4 Chapter Appendix

4.4.1 Materials and Methods

Experimental Methods

The experiments were preformed with nanoparticles held and driven in a ring vortex optical trap described previously [44, 93]. A 800 nm beam from a Ti-Sapphire laser is phase modulated with a spatial light modulator (SLM) to produce the optical ring vortex [44, 89]. 150 nm Ag nanoparticles are trapped and driven around the optical ring with a drive force determined by the number of azimuthal phase wrappings, l, applied in the phase modulation pattern applied to the SLM; the optical phase gradient force in the azimuthal direction increases linearly with l [89]. We use the optical ring vortex to trap particles against a glass surface or over a Au nanoplate mirror [93, 131]. The latter is oriented perpendicular to the optical axis causing retroreflection of the trapping beam and formation of antinode ring traps perpendicular to the optical axis that have essentially canceled the axial scattering force. Nanoparticles trapped over the Au nanoplate mirror are located in the first interference fringe approximately 250 nm from the surface of the Au nanoplate mirror [93, 131].

We create the electrodynamic barrier by having the ring trap span both the glass and Au

nanoplate mirror as shown in Figure 4.2a. The focal plane of the optical ring vortex is set halfway between the glass surface and the Au nanoplate surface in the direction of the optical axis creating a suitable trapping condition over both surfaces. The azimuthal force present in the optical ring vortex pushes nanoparticles trapped over the glass against the Au nanoplate edge and occasionally one of them transitions to the trap over the Au nanoplate. Particles continue to travel along the optical ring vortex over the Au nanoplate until they arrive near the edge of the Au nanoplate where there is another electrodynamic barrier. After crossing this barrier the particle circulates along the ring trap near the glass surface. Evidence for the electrodynamic barriers are shown in the temporal average intensity in Figure 4.2b at the $\pi/2$ and $3\pi/2$ locations, respectively. The large barrier and resulting accumulation of particles at the leading edge of the Au nanoplate ($\pi/2$ position) creates a reservoir that allows us to study the barrier crossing of single nanoparticles on the falling edge of the Au nanoplate ($3\pi/2$ position). The video microscopy data (acquired at 90 frames/sec) is analyzed by particle localization (Rahgu, Matlab) [73] and linking (Trackpy, Python) [81] to establish the trajectories (and other statistical properties) of the Ag nanoparticles.

Simulation Methods

The latter electrodynamic barrier (*i.e.* that associated with Ag nanoparticles over the Au nanoplate mirror moving to be over glass) near $3\pi/2$ in Figure 4.2d and displayed in Figure 4.2f was studied by numerical simulation using a combination of finite-difference time-domain (FDTD) and electrodynamics-Langevin dynamics (ED-LD) methods [132]. In both simulations the optical ring vortex is approximated with an 1650 nm long optical line trap oriented perpendicular to a 180 nm thick Au nanoplate. The line trap is positioned over the Au nanoplate such that half of the line trap (825 nm) is incident on the Au nanoplate and half is incident on the glass surface below the nanoplate. The line trap in the simulations has a phase gradient that produces an optical force parallel to the line trap orientation in the direction towards the edge of the Au nanoplate. The electric field in this system is calculated

by FDTD simulation and a slice parallel and along the center of the line trap in Figure 4.3a shows the electric field of the trap both over the Au nanoplate and over the glass. The highest intensity of the electric field is in the first interference fringe that is 175 nm away from the Au nanoplate, where the first antinode in the retroreflection geometry is realized. The electric field intensity decreases moving towards the edge of the Au nanoplate because the incident optical trap is allowed to propagate through the glass surface below the Au plate.

4.4.2 Electrodynamics-Langevin Dynamics (ED-LD) Simulations

The potential energy of a 150 nm Ag nanoparticle is calculated along a curve following the highest intensity region in the electric field (Figure 4.3a) from the finite difference time domain (FDTD) simulation measured relative to the distance from the edge of the nanoplate. Figure 4.3b shows the force acting on a particle in the ED-LD simulations for different drives. Simulations at low drive show that the particle gets trapped in a barrier as seen when $F_y(l)$ dips below 0 for l=1 and 2 at -300 nm and -200 nm from the edge respectfully. At higher drives (*e.g.* l=3, 4, and 5) the particle is able to cross the barrier because $F_y(l)$ remains positive for the particles' trajectory over the nanoplate. This behavior is confirmed in the FDTD calculation of the force on the particle (*i.e.* at zero temperature) over the Au plate shown Figure 4.3c. The force, $F_y(l)$ becomes negative only for l=0, 1, and 2 but remains positive for $l > 2$ in the pure electrodynamics calculation. The forces from the FDTD calculation are compared with respect to l=0 in Figure 4.3d showing that the difference between the forces is linear increase for different l's up until ~ -250 nm from the edge of the nanoplate.

4.4.3 Optical Binding

The particle's positions in the experiment are converted to polar coordinates according to a circle that is best fit to the entirety of the optical ring vortex in each experiment. Note

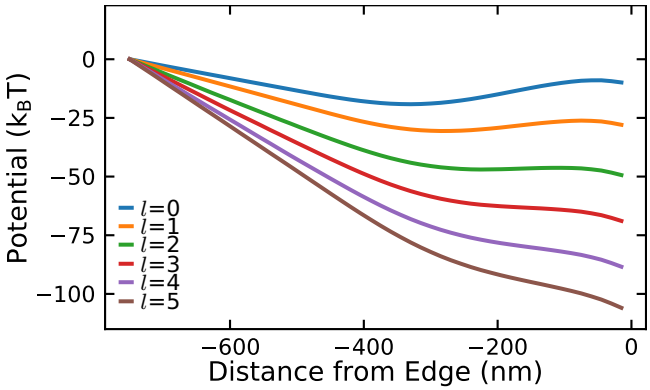

Figure 4.7: Electrodynamic potential energy, obtained from FDTD simulations. The potential energy is determined for a 150 nm diameter Ag nanoparticle following the highest electric field intensity region over the Au nanoplate.

that the "perfect ring vortex" we employ maintains a constant radius for all values of l [93]. The angular coordinate, θ, serves as the reaction coordinate for nanoparticles crossing the physical and electrodynamic barriers created by the presence of the Au nanoplate. Particles trapped in the optical ring vortex over glass are directed by the azimuthal optical force to the leading edge of the Au nanoplate mirror (Figure 4.2b at $\pi/2$) which acts as a physical barrier to the Ag nanoparticles. Since particles getting above the Au nanoplate is a rare event, the Ag nanoparticles collect near the leading edge. However, the particles become ordered in the optical ring vortex receding from the edge (counterclockwise in Figure 4.2b. The regular (averaged) particle locations shown near $\pi/2$ in Figure 4.2b result from optical binding between the nanoparticles and the edge [44, 45, 93]. The probability density (PD) and the $-\log(PD)$ is calculated along the arc of the optical ring vortex near the leading edge of the Au nanoplate. Figure 4.8 shows the arrangement of nanoparticles in optical binding locations from the physical and electrodynamic barrier caused by the Au nanoplate. The optical binding sites occupied by the nanoparticles are consistent with 600 nm separation expected for 800 nm light in water (n=1.33).

When a nanoparticle does make it into the optical ring vortex over the Au nanoplate it is driven to near the falling edge of the Au nanoplate at $3\pi/2$ in Figure 4.2b. The enhancement of trapping (and optical binding) over the Au nanoplate [93, 131] creates an electrodynamic

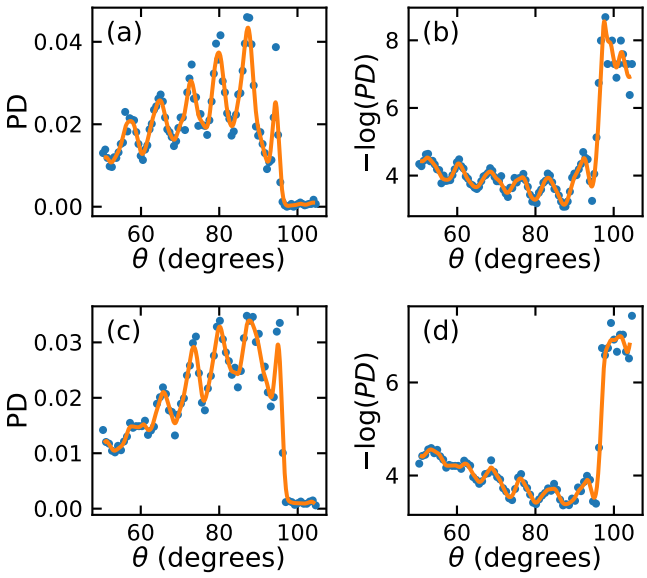

Figure 4.8: Probability density (PD) and $-\log(PD)$ for particle positions near the leading edge of the Au nanoplate for $l = 1$ (a,b) and $l = 2$ (c,d). The PD in (a) and (c) is shown as a histogram (blue markers) and as a Kernel Density Estimator (KDE, orange curve). The $-\log(PD)$ in (b) and (d) is calculated from the histogram (blue markers) or from the KDE (orange curve).

barrier for the Ag nanoparticles as they approach the edge. This is shown in increased intensity near $3\pi/2$ in Figure 4.2b and in the PD and $-\log(PD)$ of nanoparticles near the trailing edge of the Au nanoplate in Figure 4.9 and Figure 4.2f. Figures 4.9b and 4.9c exhibits a well and a barrier to particle localization (and motion) near the edge of the Au nanoplate mirror. The large barrier and resulting accumulation of particles at the leading edge of the Au nanoplate creates a reservoir that allows us to study the barrier crossing of single nanoparticles on the falling edge of the Au nanoplate.

From the PD and $-\log(PD)$ over the Au nanoplate far from either the leading or falling edges we see no evidence of an electrodynamic barrier. Figure 4.10 shows that the PD and the $-\log(PD)$ is essentially uniform for all the positions over the Au nanoplate indicating that there is no barrier.

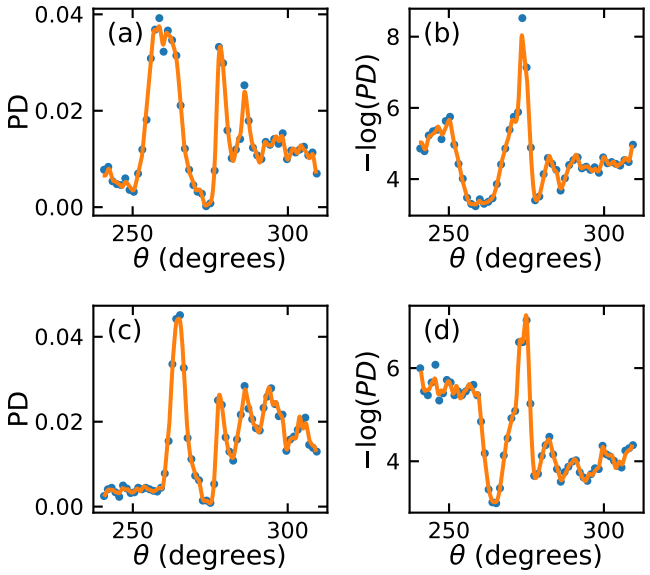

Figure 4.9: Probability density (PD) and $-\log(PD)$ for particle positions near the trailing edge of the Au nanoplate for $l = 1$ (a,b) and $l = 2$ (c,d). The PD in (a) and (c) is shown as a histogram (blue markers) and as a Kernel Density Estimator (KDE, orange curve). The $-\log(PD)$ in (b) and (d) is calculated from the histogram (blue markers) or from the KDE (orange curve).

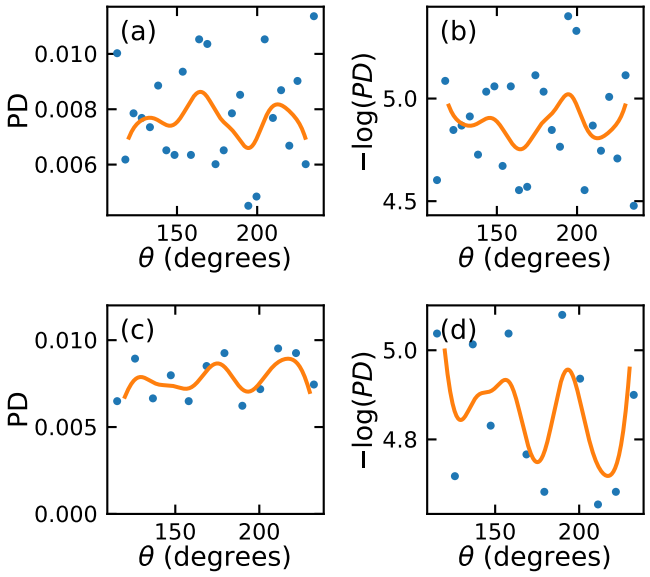

Figure 4.10: Probability density (PD) and $-\log(PD)$ for particle positions over the Au nanoplate far from either the leading or falling edges for $l = 1$ (a,b) and $l = 2$ (c,d). The PD in (a) and (c) is shown as a histogram (blue markers) and as a Kernel Density Estimator (KDE, orange curve). The $-\log(PD)$ in (b) and (d) is calculated from the histogram (blue markers) or from the KDE (orange curve).

4.4.4 Modeling Kinetics

In the main text we show that out experimental results are well fit by the Dudko-Hummer-Szabo (DHS) model [62]. We performed similar experiments using a different microscope, power density, trap radius, and a different Au nanoplate. Figure 4.11 shows that the DHS model fits these results as well. Table 4.1 summarizes the results of fitting the Bell-Evans and the DHS models to these experimental data.

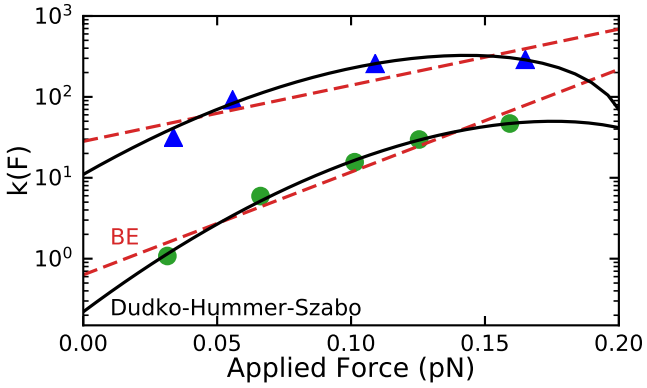

Figure 4.11: Fit to two different experiments with different conditions to the Bell-Evans (BE) and Dudko-Hummer-Szabo (DHS) models. Experiment for l =1–5 examined in the main text is represented by the green circles. An experiment for l =2–5 with different experimental parameters represented by blue triangles. Each experiment is fit with a BE fit and a DHS fit.

Table 4.1: Model parameters for the barrier crossing kinetics.

	Bell-Evans	$\nu = 1/2$	$\nu = 2/3$
$k_0[\mathrm{s}^{-1}]$	0.63	0.22	0.33
$x^{\ddagger}$[nm]	120.3	251.1	203.6
$\Delta G^{\ddagger}[\mathrm{k_B T}]$	—	7.26	6.27

4.4.5 Determination of the Nanoplate Edge

In Figures 4.5a and 4.5b in the main text we plot the $-\log(PD)$ for experiment and simulation along the reaction coordinate known as "Distance from the Edge". In the simulation, knowing the distance of the particle from the edge in y is trivial because the trajectory of

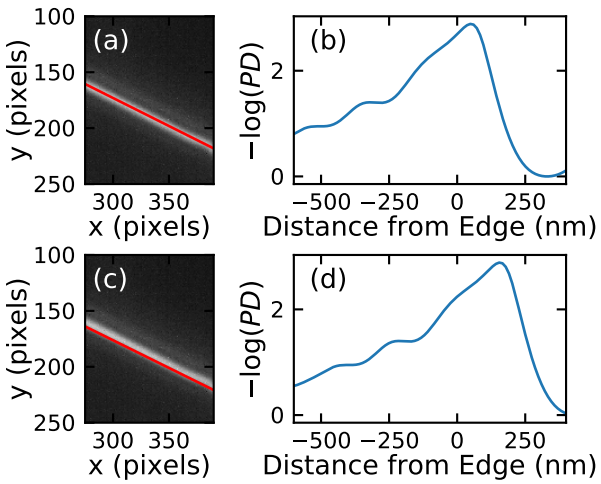

Figure 4.12: Demonstration of different methods to determine the nanoplate edge and how it affects the $-\log(PD)$. (a) Image of the nanoplate edge where the edge used in the analysis is determined from the center of the intensity band in the image. (b) The $-\log(PD)$ of the distribution of particle positions using the edge determination method in (a). (c) Image of the nanoplate edge where the edge used in the analysis is determined from the lower part of the intensity band in the image. (d) The $-\log(PD)$ of the distribution of particle positions using the edge determination method in (c).

the particle is recorded for the entire simulation. However, in the experiment, determining the location of the edge of the Au nanoplate requires some image analysis to determine because in the dark field microscopy image the edge of the Au nanoplate scatters light in all different directions. For the experimental results shown in Figure 4.5 we find the edge of the Au nanoplate by the best fit line to the light scattered off the edge of the Au nanoplate (shown in red in Figure 4.12a). This best fit line to the Au nanoplate edge was determine only from pixels from the scattered light from the edge (above a certain threshold) and the line was fit to this set of pixels using the intensities of the pixels as weights for the fit. Using this definition of the Au nanoplate edge we get the $-\log(PD)$ shown in the main text (also shown in Figure 4.12b). However, the true edge to the Au nanoplate could be anywhere within the scattered light found in the dark field microscopy image. Using the edge of the light scattered region as the definition of the nanoplate edge (Figure 4.12c) we find the $-\log(PD)$ becomes more aligned (in the "Distance from the Edge" coordinate) to the ED-LD simulation results shown in Figure 4.5b.

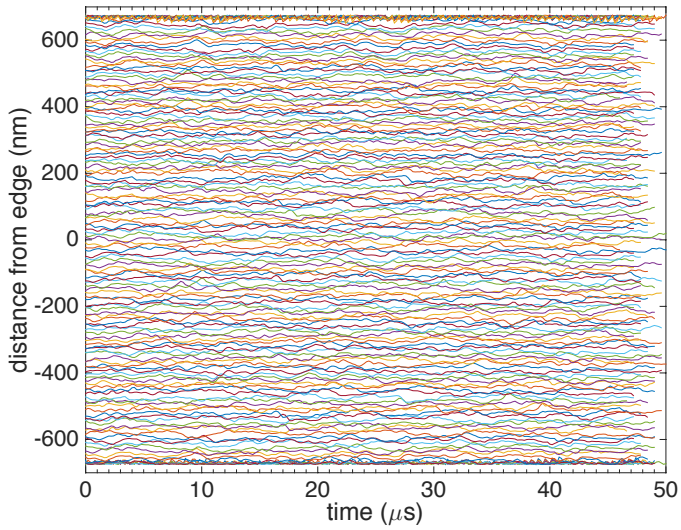

Figure 4.13: Trajectories of a Ag nanoparticle calculated using the ED-LD method for $l = 3$ with a parabolic biasing potential used to restrict the sampling within narrow regions. There are a total of 150 equally spaced biasing potentials or umbrellas.

When comparing the the experimental and simulation $-\log(PD)$ the experimental $-\log(PD)$ is shifted to align the optical binding region after the Au nanoplate edge with the one seen in the simulation at 413 nm. Because the particles in both the simulation and the experiment are the same size and the wavelength of the electric field is the same we expect that optical binding positions due to the edge of the Au nanoplate would be the same in the experiment and the simulation. The experimental $-\log(PD)$ was shifted by 78 nm to align with the minima at 413 nm in the simulation. The shift of 78 nm is within the range of error bright band of the edge of the Au nanoplate shown in the microscopy image in Figures 4.12a and 4.12c where the inner edge of the nanoplate was found to be shifted $\sim$105 nm from the center of the bright band of the nanoplate edge.

4.4.6 Equilibrium Free Energy Function Using Umbrella Sampling

We employed the Eigenvector method of umbrella sampling (EMUS) [164] to calculate the equilibrium free energy functions along the reaction coordinate for the Ag nanoparticle barrier crossing process. Umbrella sampling [163] is a technique where a series of biasing po-

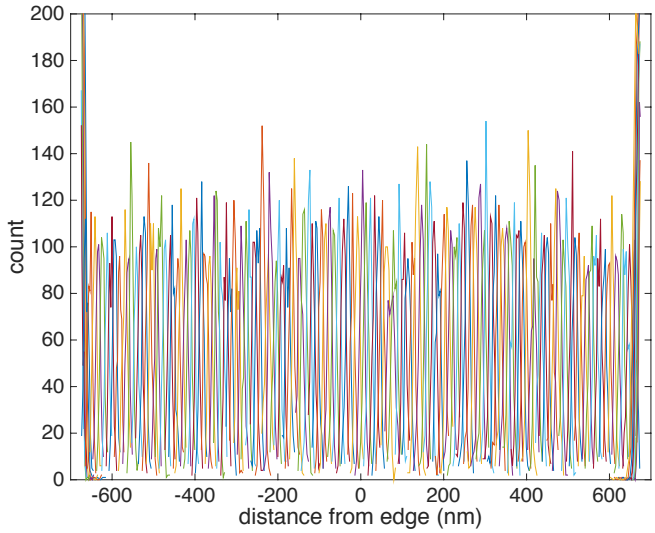

Figure 4.14: Position histogram within each parabolic biasing potential for $l = 3$ showing the narrow regions sampled by the nanoparticle and sufficient overlap between neighboring umbrellas for accurate free energy calculation.

tentials are used to restrict the sampling of a collective variable to a narrow range of values, or umbrellas, in a series of simulations. The data from the different simulations is then combined and the effect of the biasing potential is removed to obtain the overall equilibrium free energy profile. We performed ED-LD simulations to calculate the trajectories in each umbrella and subsequently used EMUS to calculate the free energy profile. The ED-LD simulations for each value of l were divided into 150 umbrellas with the following force constants of the parabolic biasing potentials, $1.5 \times 10^{-5}\,\mathrm{N\,m^{-1}}$, $1.6 \times 10^{-5}\,\mathrm{N\,m^{-1}}$, $4.5 \times 10^{-5}\,\mathrm{N\,m^{-1}}$, $7.5 \times 10^{-5}\,\mathrm{N\,m^{-1}}$, $1.0 \times 10^{-4}\,\mathrm{N\,m^{-1}}$, and $1.3 \times 10^{-4}\,\mathrm{N\,m^{-1}}$ for $l = 0$ to $l = 5$, respectively. The umbrellas were positioned such that the centers of neighboring umbrellas were closer than two standard deviations along the reaction coordinate, *i.e.*, the y axis. All the umbrellas were position in the same plane in the z direction, *i.e.*, the direction perpendicular to the place of the nanoplate. The Ag nanoparticle was initialized in the center of each umbrella and the trajectories were calculated using the ED-LD method. In Figure 4.13, the trajectories of a nanoparticle for $l = 3$ in each umbrella are plotted, showing that each of the trajectories is equilibrated within the biasing potential. The position histogram in each

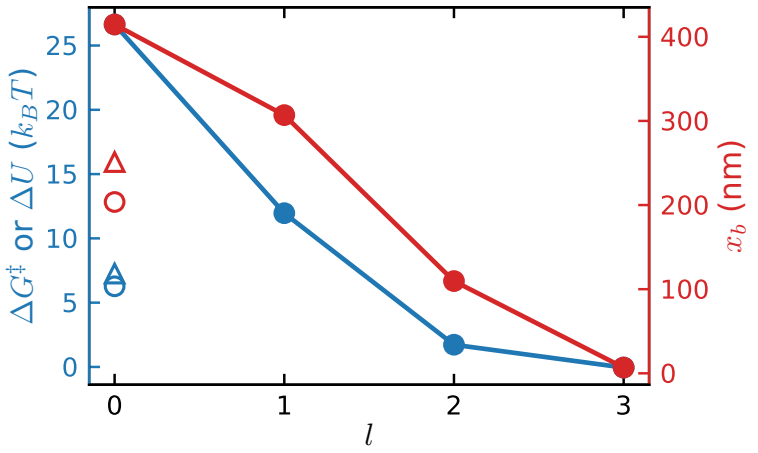

Figure 4.15: The barrier height (blue curve left axis) and barrier distance (red curve right axis) calculated from the Umbrella Sampled (US) pmfs for l=0–3. Symbols show the calculated $\Delta G^{\ddagger}$ and $x^{\ddagger}$ calculated from the DHS models for different values of ν. Open triangles show the DHS fit when $\nu = 1/2$ and open circles show the DHS fit when $\nu = 2/3$. Blue symbols show $\Delta G^{\ddagger}$ (left axis) and red symbols show $x^{\ddagger}$ (right axis) from the DHS fits.

umbrella for $l = 3$ are plotted in Figure 4.14 showing that there is sufficient overlap between the positions within neighboring umbrellas.

4.4.7 Summary of Model Results

Figure 4.15 summarizes our results from the umbrella sampled pmfs and the experimental fits to the DHS model. The minimum and the maximum of the pmf from the umbrella sampled result were determined and used to calculate the barrier height ($\Delta G^{\ddagger}$ at $l = 0$ or ΔU for $l > 0$) and distance to the barrier (x_b) for $l \leq 3$. For $l > 3$ the drive force is too large and there is no barrier in the pmfs. We found that the umbrella sampled results predict a larger $\Delta G^{\ddagger}$ and $x^{\ddagger}$ than the experimental fits to the DHS model (Figure 4.15 open symbols).

4.4.8 Comparing Electrodynamic Barrier Crossing Experiment to Single-molecule Force Spectroscopy

To draw an analogy between our experiments and single-molecule force spectroscopy experiments we compare several different experimental parameters to show we are in the same

kinetic regime as the single-molecule force spectroscopy experiments. In the main text we discuss the enhancement factor of the rate of reaction versus the equilibrium rate. This involves taking the ratio of the rate of reaction of our highest drive experiment, $k(F)$ at $l = 5$, and the calculated equilibrium rate from the DHS model, k_0. We found that $k(F)$ at $l = 5$ was $85\,\mathrm{s}^{-1}$ and our calculate k_0 was $0.22\,\mathrm{s}^{-1}$ meaning that the force in our experiment is increasing the rate of reaction to 390 times the equilibrium rate. We compare this to the rates in other papers for example Garcia-Manyes et al. [162] where the max rate of $k(F)$ was $\sim 10\,\mathrm{s}^{-1}$ while the calculated k_0 was $1.4 \times 10^{-3}\,\mathrm{s}^{-1}$ which means the rate of the fastest experiment was 7.14×10^3.

Another analysis that is often done in single-molecule pulling experiments is a extended version [168, 169] of Jarzynski's nonequilibrium work relation [170] which is used to determine the free-energy curves from the force extension curves. In Nome et al. [51] the free-energy curve is determined in and the maximum slope of this curve should relate to the energy required to cross the studied molecular barrier. The maximum slope of the free energy in Nome et al. [51] was $16\,\mathrm{k_B T\,nm^{-1}}$. This can be compared to the mean rupture force in the pulling experiment with some dimensional analysis to convert to pN. After conversion we find that equilibrium rupture force calculated from the Jarzynski relation is 65.9 pN which is much less than the average rupture force found in the experiment of 135 pN. This further demonstrates that the single-molecule pulling experiments are very far from equilibrium.

CHAPTER 5

MECHANISMS FOR REARRANGEMENTS AND BARRIER CROSSING IN 2D DRIVEN OPTICAL MATTER

5.1 Introduction

In Chapter 3 we examined the properties of driven optical matter and in Chapter 4 we used optical matter to study barrier crossing in the presence of a drive and thermal noise and compared the results to molecular kinetic models. However, in Chapter 4 the nature of the barrier was static with respect to the motion of the particles in the optical ring vortex. Therefore, establishing optical matter as a model system for more particular aspects of molecular interactions and to better understand the assembly of larger optical matter systems requires treating the specific interactions and dynamics of nanoparticles that constitute optical matter. For example, the molecular interactions between two gases, *e.g.* $\mathrm{ClNO_2}(g) + \mathrm{NO}(g) \rightleftarrows \mathrm{NO_2}(g) + \mathrm{ClNO}(g)$ [171], involve molecules of different sizes and shapes colliding in a specific way to cause the reaction to take place. So far the experiments presented in Chapters 3 and Chapter 4 do not directly relate optical matter to collisional dynamics and are also limited to 1-D interactions. In Chapter 4 the kinetics of driven optical matter was studied with respect to a static electrodynamic barrier while in Chapter 3 we addressed the fluctuating interactions between nanoparticles occupying different optical binding states, however, particles were still confined to the (effectively) one dimensional ring trap.

In this chapter we study the dynamics and kinetics of rearrangements of driven optical matter where the process or "reaction" requires two dimensional movement and is due to the electrodynamic nanoparticle interactions. We designed the driven optical matter experiments so that they have more analogies to molecular reaction phenomena. The optical polarization-dependent electrodynamic interactions serve as our analogue to intermolecular interactions while a reduction in the trapping laser power allows the driven optical matter to fluctuate

in two dimensions compared to the tightly confined traps presented in Chapter 3.

The space-dependent electrodynamic interactions between the nanoparticles allow studying barrier crossing with an oscillating barrier [172–174]. Because the polarization of the incident optical trapping beam on the particles is maintained in one direction for the experiments, the electrodynamic optical binding [40, 44, 93] interaction between a pair of particles in the optical ring vortex will change depending on where the particles a located in the ring trap. Therefore, this driven optical matter experiment can be understood as an oscillating barrier crossing system in the regime where the modulation rate is slower or comparable to the timescale for barrier crossing.

5.2 Methods

The experiments were preformed with nanoparticles held and driven in an optical ring vortex described previously in Chapter 3 [44, 93]. The 800 nm beam from a Ti-Sapphire laser is phase modulated with a spatial light modulator (SLM) to produce the optical ring vortex [44, 89] with beam power going into the back aperture of the microscope objective of $\sim$45 mW. Citrate capped 150 nm Ag nanoparticles (NanoComposix) are diluted 200x and placed into a sample chamber described in Chapter 2. The Ag nanoparticles are trapped and driven around the optical ring with a drive force determined by the number of azimuthal phase wrappings, l, applied in the phase modulation pattern on the SLM. The motion of the Ag nanoparticles is visualized via dark field microscopy and captured with a Neo sCMOS camera at 110 frames per second. A variety of different experiments were done at different l's with each one consisting of 45 s–90 s (5000 to 10,000 frames) of video. In order to resolve distinct particle shapes without blurring or distortion a camera exposure of 2×10^{-3} s to 6×10^{-4} s was used when capturing video.

Particle trajectories were extracted from the video data using the Python particle tracking software package TrackPy [81]. A function in TrackPy uses a method to accurately track particles even when two or more particles become part of a cluster [175]. The optimal

parameters for each experiment were determined by hand and were set so that the number of particles identified in each frame is consistent with the number of particles in the experiment. Additionally, frames where the focus of the image drifted were removed from particle tracking as the particle tracking algorithm would find false positives in the de-focused image of the particles. The code that performed the algorithm and contains all the optimized parameters can be found in the Supplemental Material. However, this method of particle localization uses the center of mass method which can lead to significant errors especially when particles come in close proximity [176]. So another TrackPy function which refines the positions of particles by performing a non-linear least-squares (NLLS) fit of a Gaussian function to each position allows for extracting the true positions of the particle locations with much greater accuracy especially in the case of overlapping features. The script to the perform the NLLS Gaussian fit with the parameters is in the Supplemental Material.

5.3 Results and Discussion

Ag nanoparticles are trapped over glass using an optical ring vortex similar to previous experiments in Figliozzi et al. [93]. An 800 nm laser is used with a spatial light modulator (SLM) to create the optical ring vortex. The power of the optical ring vortex after the SLM and before the back aperture of the objective is 40 mW creating a much weaker trapping condition than in Figliozzi et al. [93]. The metal nanoparticles still exhibit a strong scattering force which causes them to be held against the glass surface and the azimuthal phase gradient in the optical ring vortex causes the nanoparticles to be driven around the optical ring vortex (Figure 5.1a). Figure 5.1a shows representation of the raw data with arrows indicating the direction of travel for nanoparticles in the optical ring vortex. Since the laser power is lower than past experiments, the gradient forces acting on the Ag nanoparticles are much weaker. Particles in the optical ring vortex travel around the ring at a slower rate and have a wider radial distribution due to the decreased gradient force. Occasionally, particles can rearrange in the optical ring vortex if one fluctuates away from the center of the ring trap and returns

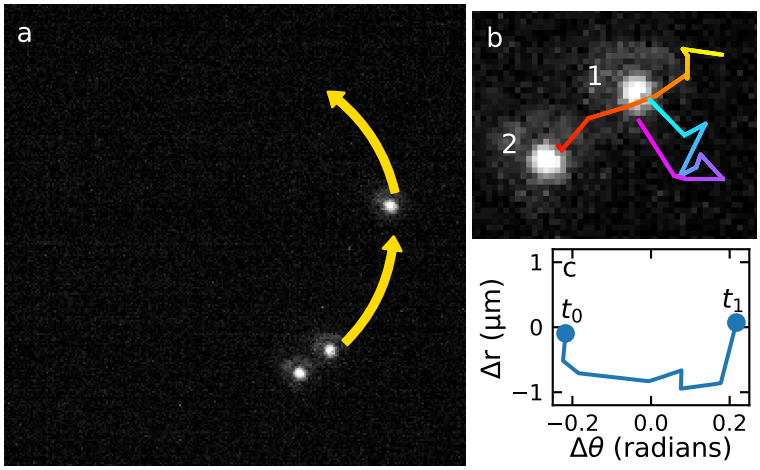

Figure 5.1: Image data and trajectories of passing events. (a) Single frame of Ag nanoparticles in an optical ring vortex. Yellow arrows indicate the direction the Ag nanoparticles travel. (b) Trajectories of particle passing event. The colored line indicates the path the Ag nanoparticle travels in the next four frames of the experiment. Particle 1 follows the trajectory that transitions from blue to purple while particle 2 follows the trajectory that transitions from red to yellow. (c) Trajectory of particle 2 from (b) plotted in polar coordinates relative to particle 1, $\Delta\theta$ and Δr. The trajectory follows the path from the t_0 to t_1.

to the trap after another particle has passed by it. An example of these passing events are illustrated in Figure 5.1b, the leading particle (in the direction of the rotating optical force) follows the trajectory off the ring trap, while the trailing particle passes due to the applied optical force.

The trajectories of the Ag nanoparticles in the optical ring vortex naturally fit a polar coordinate system, r and θ, for each particle. However, when looking at passing events between pairs of particles it is convenient to define a relative coordinate system in polar coordinates, Δr and $\Delta\theta$, that relates the position of one the particles in the pair to the other. When identifying a passing event we look for when the $\Delta\theta$ coordinate for one of the particles changes sign (*e.g.* goes from $\Delta\theta > 0$ to $\Delta\theta < 0$) as that is when the pair of particles have swapped which one is leading in the polar coordinate θ. An example of the trajectory of a passing event is shown in Figure 5.1c where the origin is set to the leading particle and the relative trajectory of the trailing particle is mapped in Δr and $\Delta\theta$ coordinates.

In the reaction coordinates Δr and $\Delta\theta$ we can examine the difference in the probability

density of particle positions of passing events versus all trajectories. If we always choose the origin to be the leading particle then the positions of a second particle can be mapped relative to the leading particle in Δr and $\Delta\theta$. The optical binding interaction that results from trapping the Ag nanoparticles with 800 nm laser light can be visualized in Figure 5.2a by the high probability regions at 0.125 rad corresponds to a particle separation of 600 nm. In the case of a passing event in Figures 5.2a and 5.2b the second particle has to traverse from $-\Delta\theta$ to $+\Delta\theta$. One might expect that in this representation of setting the leading particle to the origin would result in a higher probability density of particle positions on the $-\Delta\theta$ side of the heat maps in Figures 5.2a and 5.2b compared to the $+\Delta\theta$ side because of the energy barrier of one particle passing another. However, when a passing event occurs and the trailing particle goes from $-\Delta\theta$ to $+\Delta\theta$ the pair of particles will continue to interact as the pair moves around the optical ring vortex which is why the probability density in Figure 5.2a is about the same magnitude at $-\Delta\theta$ and $+\Delta\theta$.

The trajectories of particle pairs can be segmented further to just trajectories involved in passing events. For a pair of particles that are involved in a passing event we find the time point before they pass and look at the trajectory of the particle in the 15 frames immediately before and after the passing event. The distribution of particle positions of the frames surrounding a passing event are shown in the heat map in Figure 5.2b. The passing trajectories can be split into two cases, one where the particle passes with $-\Delta r$ and one where the particle pass with $+\Delta r$, which are used to calculate the mean path of particle passing on the $-\Delta r$ side or the $+\Delta r$ side respectfully. The two red curves in Figure 5.2b shows the mean passing trajectory for particles that pass with $+\Delta r$ (top curve) or $-\Delta r$ (bottom curve). For $\Delta\theta$ between -0.125 rad and -0.125 rad the mean path of passing originates from the optical binding location (at $\Delta\theta = -0.125$ rad) and travels around the leading particle and ends at the optical binding location at $\Delta\theta = 0.125$ rad. However, when the particles pass they do not maintain an optical binding separation because the mean path of passing does not reach $\Delta r = 0.6\,\mu$m or $-0.6\,\mu$m as the particles move around each other. For $\Delta\theta < -0.125$ rad

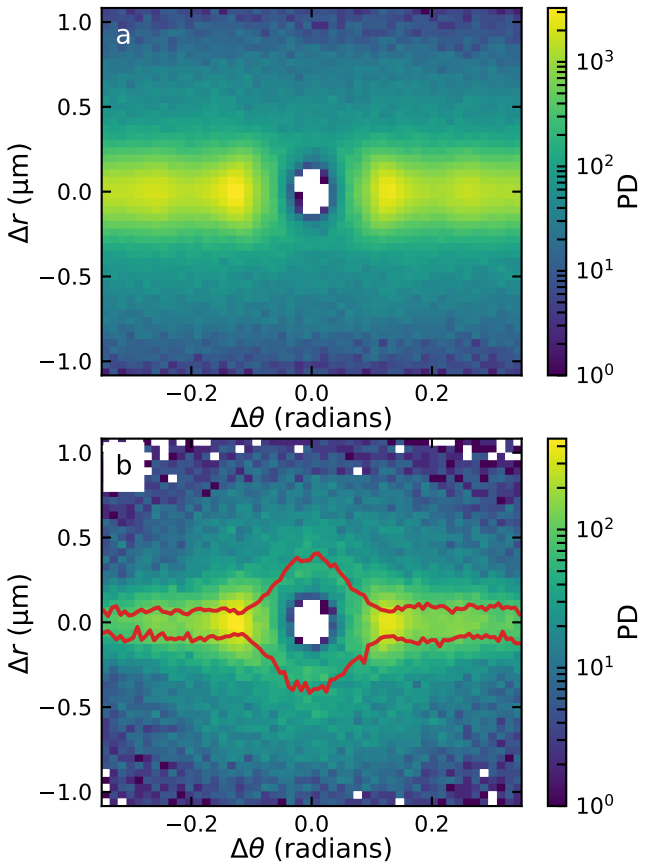

Figure 5.2: Probability density (PD) of particle pair trajectories and passing trajectories. (a) Distribution of positions of a second particle relative to the leading particle. (b) Distribution of positions of a second particle relative to the leading particle in a passing event. The red colored line indicates the mean trajectory the trailing particle makes around the leading particle during a passing event.

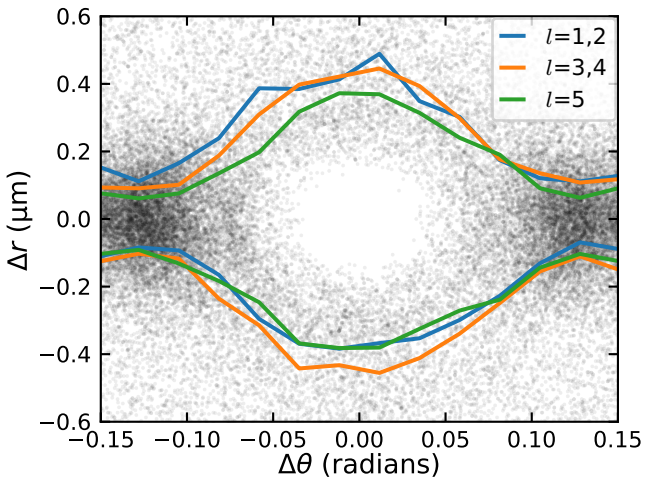

Figure 5.3: Mean trajectory of particle passing for different drives. Curves show the mean path of a passing event for different groups of l's. The black markers show the position of particles in Δr and $\Delta\theta$ within a 30 frame window where the passing event occurs in the center of the window.

and $\Delta\theta > 0.125\,\text{rad}$ the mean passing trajectory for particles that pass with $+\Delta r$ and $-\Delta r$ do not converge at $\Delta\theta = 0$ which is due to the variety of paths a particle can take in a passing event. For example, the trailing particle may have a $|\Delta r| \gg 0$ before approaching the $\Delta\theta = 0$ where the passing event occurs. Therefore when mean path is calculated for particles that pass with $+\Delta r$ and $-\Delta r$ there is a bias in the mean path towards the Δr that the particle passes on.

The mean passing path can be further segmented into passing paths for different l's to show how the most probable path of passing changes with the applied drive. The three curves in Figure 5.3 show the mean passing path for $l = 1, 2$ (blue), $l = 3, 4$ (orange), and $l = 5$ (green). For passing events with $+\Delta r$ the maximum of Δr along the path decreases as the drive is increased. Additionally, the mean path of $l = 5$ has larger curvature in Δr approaching the transition state (at $\Delta\theta = 0$) between $\Delta\theta = -0.10\,\text{rad}$ to $0\,\text{rad}$ than after the transition state between $\Delta\theta = 0\,\text{rad}$ to $0.10\,\text{rad}$. For the mean passing paths with $-\Delta r$ there is no trend in the the minimum of Δr with the drive force.

In order to grasp how the particles are passing each other in the optical ring vortex different statistical properties of the passing events can be examined. The mean radius of

particle positions, r_{avg}, in the optical ring vortex is a close approximation to the radial center of the optical ring trap. For each particle in a passing event we can compare the deviation, $|r - r_{\text{avg}}|$, of that particle from the average radius of the optical ring vortex. In Figure 5.4a we group the each particle in a passing event into two groups, particles with the smaller $|r - r_{\text{avg}}|$ are shown in blue while particles with larger $|r - r_{\text{avg}}|$ are shown in orange. Considering the grouping done in Figure 5.4a, there is no surprise that the particles that have the smaller $|r - r_{\text{avg}}|$ are grouped much more around $|r - r_{\text{avg}}| = 0$ than the particles with the larger $|r - r_{\text{avg}}|$. However, it is important to note the small amount of overlap these two distributions have indicating that during a passing event one of the particles is very likely going to be in the ring trap while the other is outside of the ring trap. Most likely, for a passing event to occur, one of the two particles must continue to be driven by the azimuthal force in the optical ring trap. Another conditional probability of grouping the $|r - r_{\text{avg}}|$ by trailing/leading particles gives insights into the mechanism for the rearrangement of Ag nanoparticles. As seen in Figure 5.4b the trailing particle has a larger probability of remaining in the optical ring trap during a passing event while the leading particle is more likely to be leave the center of the ring trap during a passing event.

We suspect that electrodynamic interparticle interactions, known as optical binding [40], are assisting the particle passing events. Optical binding [40] results from the incident electric field interfering with the scattered electric field from each particle. In the experiments performed in this chapter the polarization state of the trapping beam is horizontal in the lab frame aligned with the 0 and π parts of the ring. The optical binding interaction is strongest between nanoparticles oriented perpendicular to the polarization. To simulate the optical binding potential in the optical ring vortex, the pair wise optical binding potential was averaged in a ring pattern of the same radius as the experimental optical ring vortex using weighting that correspond to the probability of finding a particle at each θ position on the ring. Figure 5.5 gives a representation of the optical binding potential for a pair of particles moving around the optical ring vortex. As discussed in Figliozzi et al. [93] when

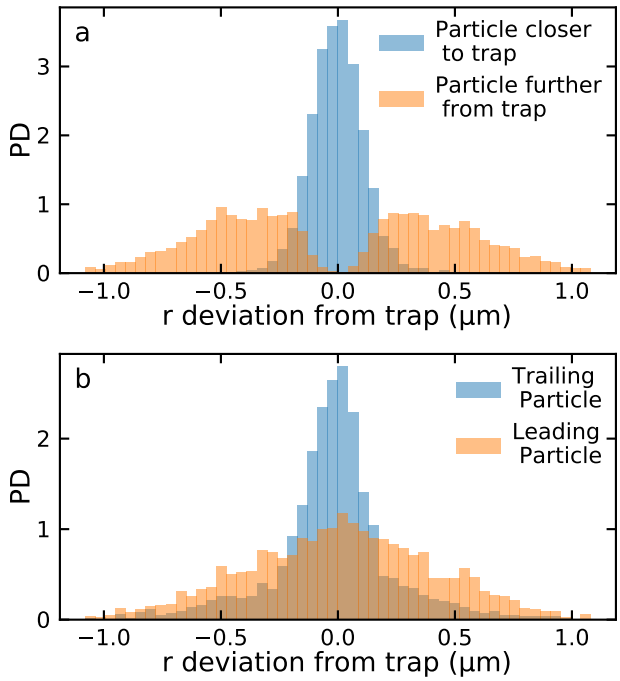

Figure 5.4: Histograms showing probability density (PD) of particle deviation from trap and location in ring of passing events. Particle deviation from the trap center during passing separated based on the particles' distance, in r, from the trap center. Blue represents particles that are closer to the trap center during a passing event while orange represents particles that are further from the trap center during a passing event. (b) Particle deviation from the trap center for successful passing events. Blue represents the particle that originates behind before a passing event while orange represents the particle that originates ahead before a passing event. The deviation from the trap center was calculated from the average particle position in r.

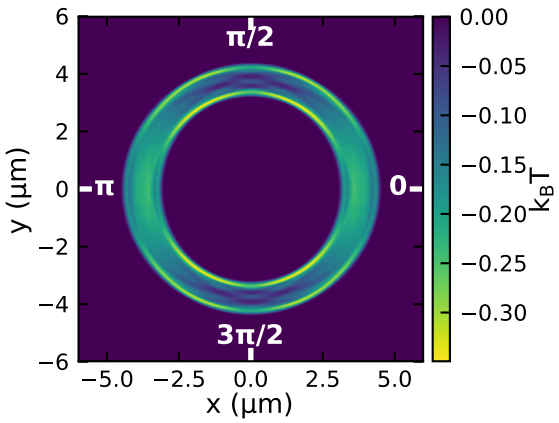

Figure 5.5: Representation of optical binding potential around the optical ring vortex. The electrodynamic potential from optical binding was averaged over a circular pattern with at the same radius of the optical ring vortex. The averaging of the potential scales with the force modulation discussed in Figliozzi et al. [93].

particles or in the 0 and π sections of the ring the optical binding interaction aligns with the optical ring vortex while at the $\pi/2$ and $3\pi/2$ the optical binding interaction is positioned off of the ring trap. From the potential energy surface in Figure 5.5c there are four regions of low potential on either side of the center of the ring shown at $\pi/4$, $3\pi/4$, $5\pi/4$, and $7\pi/4$. The locations of passing events in Figure 5.6a align with two of these regions in Figure 5.5, namely the $3\pi/4$ and $7\pi/4$ regions of the ring trap which supports that optical binding is a necessary component to a passing event taking place.

The location of particle passing events was examined with respect to the location of the particle pair on the ring trap and it was found that passing events only occur at specific locations around the optical ring vortex. A histogram of passing events versus θ reveals that passing events occur at $3\pi/4$ and $7\pi/4$ (Figure 5.6a) while the probability of a passing event occurring at $\pi/2$ and $3\pi/2$ is low. If our reaction coordinate for a pair of particles rearranging is the $\Delta\theta$ between the pair we can construct $-\log(\text{PD})$ landscape from the distribution of $\Delta\theta$ from particles pairs. We can apply a conditional probability to look at the $-\log(\text{PD})$ for when a pair of particles are located in the ring where rearrangements are more likely (*i.e.* θ equals $3\pi/4$ and $7\pi/4$) or where rearrangements are less likely (*i.e.* θ equals $3\pi/4$ and $7\pi/4$) Figure 5.6b shows $-\log(\text{PD})$ landscape of $\Delta\theta$ shows a barrier at $\Delta\theta = 0$ where the

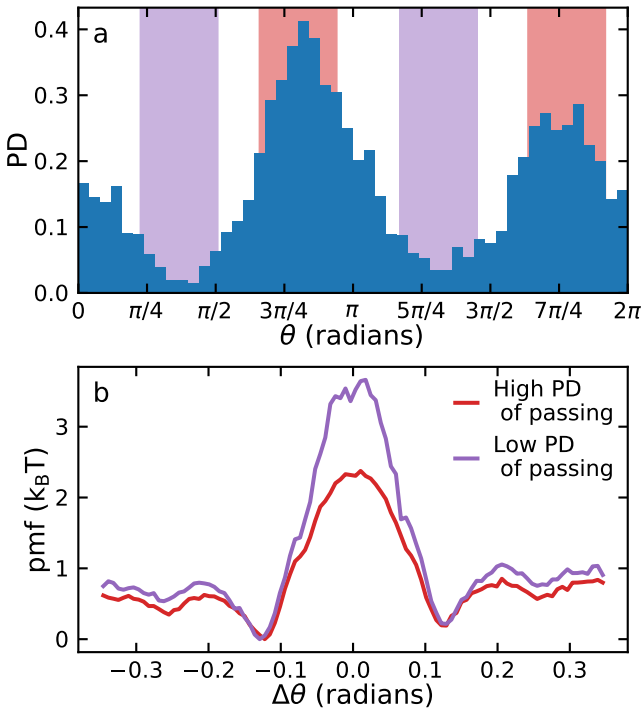

Figure 5.6: Probability density (PD) of passing events angularly around the ring and the statistical landscape of particle passing a high and low passing regions. (a) The probability of a passing event occurring in a specific section in the optical ring vortex. The red vertical bands are θ locations in the optical ring vortex where passing events are likely while the purple vertical bands are locations where passing events are the least likely. (b) The conditional $-\log(\text{PD})$ along the $\Delta\theta$ separation between a pair of particles in θ regions of high/low probabilities of passing events around the ring. The distribution of $\Delta\theta$ positions of particle pairs selected from the red/purple bands in (a).

optical binding between the particle pair is represented in the minima at $\Delta\theta = \pm 7\,\text{rad}$. For locations of the ring trap where particle passing is likely, the barrier for particles crossing $\Delta\theta = 0$ (Figure 5.6b, red curve) is much lower than the barrier for particles crossing $\Delta\theta = 0$ (Figure 5.6b, purple curve) in locations where particle passing is less likely. As a pair of particles move around the ring trap, the effective probability landscape modulates between the two curves shown in Figure 5.6.

Various aspects of the kinetics of the particle passing events are examined from different data sets and different l's. The rate of a passing event is determined by the dwell time distribution. The dwell time of passing can be found by counting the time for when a pair of particles first engage each other and count the amount of time until they pass. Here, the

dwell time is found by finding the times when a pair of particles have a $|\Delta\theta| < 0.26\,\mathrm{rad}$ and count the number of frames until the particles pass. The distribution of these dwell times are aggregated for different l's and the decay of the cumulative dwell time, CDT $= 1 - \int_{-\infty}^{t} P_{\mathrm{D}}(t')dt'$, is fit with an exponential decay, Ae^{-kt}, in order to extract the decay rate, k. Because we find the decay rate for each l we can plot the drive dependent rate constant $k(l)$ vs l shown in Figure 5.7a. Surprisingly, there is no trend in the the rate of particle passing calculated from the decay of the dwell time versus the applied drive. However, to characterize how frequently passing events occur at a specific l the rate of events is calculated for each experiment. This is done by simply identifying the number of events in each experiment and dividing by the time the data was collected to get an event rate. However, different experiments had different numbers of particles and the number of particles can influence the number of events, *i.e.* when more particles are present then there is more pairs available for rearrangement in a passing event. To correct for the different number of particles in each experiment the event rate is divided by the number of combinations of particle pairs in each experiment

$$\binom{n}{2} = \frac{n!}{2!(n-2)!}, \tag{5.1}$$

where n is the number of particles in the experiment. The event rate, when normalized with equation 5.1, increases linearly with l (Figure 5.7b). One would expect that the trend found in the number of passing events in Figure 5.7b would also be present in the rate of passing in Figure 5.7a, however, that is not the case. To reconcile these disparate results we believe that the drive force only affects the number of attempts of a pair of but has no affect on the amount of time it takes for an individual passing event.

5.4 Conclusions

We have characterized the properties and kinetics of particle rearrangements in driven optical matter. We found that in order for a particle rearrangement to occur the particles must be

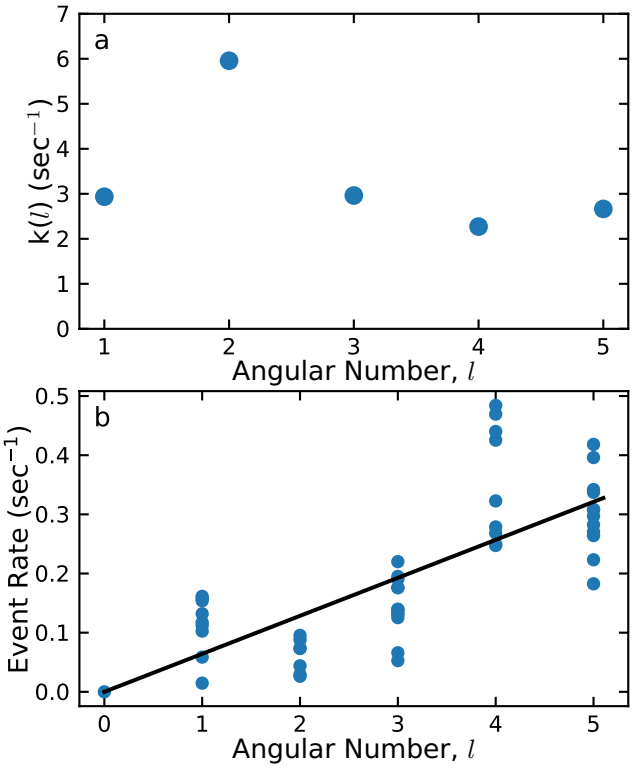

Figure 5.7: Dwell time for each event and frequency of passing events. (a) The l dependent rate of passing events calculated from when a pair of particles crossing from $\Delta\theta$ of $|\Delta\theta| < 0.26$ rad to when the particles pass. (b) The frequency of passing events for each l (blue markers) with a best fit line to all the points (black line). The frequency of is calculated by dividing the number of events in an experiment by the number of frames and dividing by the number of combinatorial of pairs of particles in each experiment. The best fit line has the y-intercept fixed at 0.

located on the ring trap at specific positions and that one particle must remain in the trap in order for the drive force to push it past the other particle involved in the rearrangement. This mechanism of particle rearrangement may rely on the electrodynamic interaction between the pair of nanoparticles in order for the reaction to take place. We believe that the particle rearrangements in driven optical matter fit the class of kinetics that is dominated by an oscillating barrier [174, 177].

We also found that the rate of particle passing events are independent of the applied drive force on the particles even though the number of passing events occurring in a time window increases. We believe that increasing the drive force only increases the number of attempts at a passing event but does not affect the rate of two particles engaging and passing one another. When a pair of particles get close enough to each other so that they may pass, they must travel as a pair until they reach the appropriate location where the electrodynamic pair interactions stabilize the particle rearrangement. Craven et al. [174] discuss the effects of a periodically modulated force has on a chemical reaction and they determined that the rate of the reaction depends directly on the stability of the transition state. If the transition state of our particle rearrangements depend on the electrodynamic interactions, and therefore, the power of the trapping laser, then perhaps if the power of the laser was increased for these experiments then more particle rearrangements would occur and keeping the laser power constant for these experiments allowed us to only sample on reaction rate for particle passing events. However, increasing the laser power increases the strength of the trap which competes with the stability of particles out of the center of the ring trap, which we show is an essential part of particle rearrangements in Figure 5.4. Using an optical ring vortex that is de-focused or is more diffuse in the radial direction may allow better probing of reaction rates stabilized by the transition state and not by the azimuthal drive force.

CHAPTER 6

SINGLE-PIXEL INTERIOR FILLING FUNCTION (SPIFF) APPROACH FOR DETECTING AND CORRECTING ERRORS IN PARTICLE TRACKING

Reproduced in part with permission from: Stanislav Burov, Patrick Figliozzi, Binhua Lin, Stuart A. Rice, Norbert F. Scherer, and Aaron R. Dinner. Single-pixel interior filling function approach for detecting and correcting errors in particle tracking. *Proc. Natl. Acad. Sci.*, (20):201619104, 2016. doi: 10.1073/pnas.1619104114. Copywright Proceedings of the National Academy of Sciences of the United States of America [93]. Author contributions: S.B., N.F.S., and A.R.D. designed research; S.B., P.F., and B.L. performed research; S.B. and P.F. analyzed data; and S.B., S.A.R., N.F.S., and A.R.D. wrote the paper.

6.1 Introduction

In an optical imaging experiment the photons that are detected to create a digital image of an object are distributed according to the point spread function (PSF) of the instrument used [178, 179]. By exploiting specific properties of the PSF it is possible to determine the positions of particles with subpixel precision. This idea is used extensively for tracking single molecules [179, 180] and colloidal particles [71] and stars [181]. The approaches used include special techniques that exploit photoactivation and photobleaching properties of fluorophores to achieve resolutions that can exceed the Abbe diffraction limit, fluorescence imaging with 1-nm accuracy [182], nanometer-localized multiple single molecules [183], photoactivated localization microscopy [184], stochastic optical reconstruction microscopy [185], and bleaching-assisted localization microscopy [186]. In all of these techniques a key ingredient is the tracking algorithm that transforms the data from intensities at the detector pixels into individual particle positions.

A tracking algorithm is a mathematical procedure that assigns the position of the center of

an emitter based on the recorded distribution of the photons across multiple pixels. Different algorithms make different assumptions that affect the tracking performance. Some methods exploit the symmetry of the PSF to localize emitters [71, 73, 180, 187–191]; these include the CrockerGrier method, which estimates the center of mass directly from an average that is weighted by pixel intensities [71], and another recent method that exploits triangulation [73]. Some methods specifically model the PSF as a Gaussian function [187]; these include least-squares (Gaussian) fitting [180] and the maximal likelihood method [188].

Experimental realities can limit both tracking accuracy and precision to considerably lower resolution than often appreciated (e.g., pixel-level, rather than subpixel). Undersampling and inadequate magnification mainly affect the accuracy [74, 192], whereas poor signal-to-noise mainly affects precision [73, 74]. Optical intensity overlaps that arise when emitters are closely spaced decrease both accuracy and precision [73]. Unfortunately, there is no agreed-upon standard benchmark with which to evaluate tracking performance. Even worse, trajectories with erroneous information can lead to inference of behavior that is an artifact of the tracking algorithm [193]. Moreover, because determining the assumptions made by a proprietary implementation of an algorithm can be challenging, it is important to have tools that can establish the quality of the estimated particle positions directly from the output. The common strategy of checking the variation in tracked positions of motionless reference markers has several drawbacks [74]: (i) The field of view of interest may not contain suitable markers; (ii) markers may not be motionless; and (iii) the true positions of the markers with respect to the reference frame of the imaging system are unknown, so they cannot be used to quantify systematic errors. The need for a general method for validation was made clear in a recent comparison of algorithms for a range of different data types [194]. The general problem of proper linking of tracked locations in various experimental situations [195] that stimulated this comparison is significantly affected by the proper estimation of locations in a single frame.

Here we develop an approach that can reveal, quantify, and correct bias in tracked po-

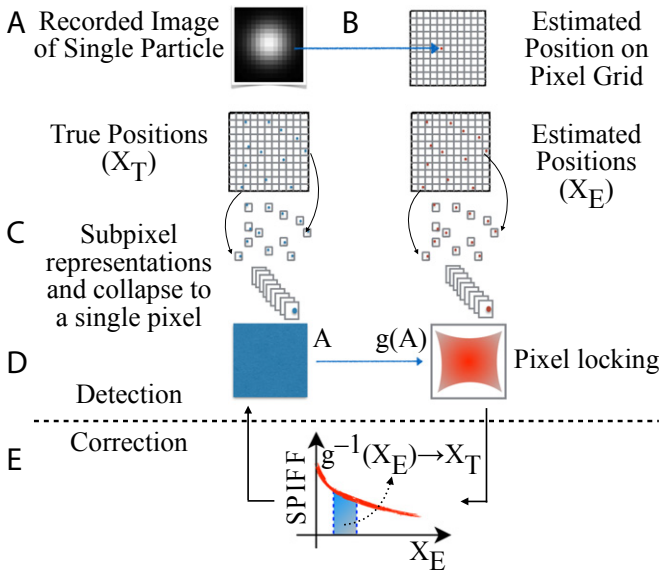

Figure 6.1: Schematic representation of the tracking process and its relation to the SPIFF. (A) The distribution of intensities in pixels of the detector forms an image of each particle. (B) A tracking algorithm transforms the distribution of intensities into estimated particle positions with subpixel resolution. The estimated positions can differ from the true positions. (C) We construct a histogram of positions within pixels, the SPIFF. The SPIFF aggregates statistical information from many particle localizations. (D) The SPIFF of the true positions is uniform, whereas that of a biased algorithm is nonuniform (Eq. 6.2). The region of all of the true positions, A, is transformed into the region $g(\mathrm{A})$ of estimated positions. (E) Correction of the bias detected by discovery of a nonuniform SPIFF profile obtained from experiment. Integration of the SPIFF (red line) is used to determine the inverse function g^{-1} (i.e., calculating the area under the SPIFF, represented by the blue region), which is used to transform the estimated positions to true positions by rescaling of the SPIFF to have a uniform distribution over the entire pixel.

sitions. Our approach involves constructing the distribution of estimated positions within pixel interiors, which we term the single-pixel interior filling function (SPIFF; Figure 6.1). Bias of the SPIFF toward the center of pixels is related to an effect known as "pixel locking" [75, 76] and "pixel biasing" [71, 196–198]. We formulate the SPIFF approach in terms of two axioms: (I) the probability of finding particles in a region of the image should be conserved by an unbiased tracking procedure and (II) the estimated particle positions should be uncorrelated with the boundaries between pixels of the detection system. We test for satisfaction of these constraints by constructing the SPIFF, a histogram of output positions. Any deviation of the SPIFF from a uniform distribution indicates bias in the tracking algorithm.

We use simulated data to illustrate how our approach can correct tracking errors arising from undersampling and intensity overlaps in crowded systems. The latter situation is of particular interest owing to its frequent occurrence in measurements and the lack of alternative means of controlling these errors. Moreover, we show that the SPIFF-based correction is capable of achieving and even exceeding the unbiased Cramér-Rao lower bound (CRLB), the standard by which tracking algorithms are commonly judged. Our approach contrasts with the standard approach of minimizing pixel locking by expanding the sampling region, which introduces additional noise to the measurement. Additional situations are considered in the Chapter Appendix. In particular, we analyze experimental data for quasi-2D colloidal suspensions and show how tracking errors can introduce artificial correlations in successive particle displacements that the SPIFF-based approach corrects (Chapter Appendix, section 6.6.1).

6.2 Axioms and the SPIFF

The combination of an imaging experiment and tracking algorithm can be viewed as a mapping of the true particle position, X_T (in Cartesian coordinates due to the pixel grid), to an estimated particle position, X_E:$g(X_T) \rightarrow X_E$. The mapping generates an estimate of the true position but with unknown accuracy. To reconstruct the true position without loss of information, g must be injective, that is, a function that preserves distinctness of elements in its domain. Because ideally $X_E = X_T$, g should be the identity function. In practice, algorithms in current use exhibit systematic errors, and g deviates significantly from the identity function in those cases. Moreover, because X_T varies continuously, the identity property of an unbiased algorithm means that g is also differentiable. Differentiability, in turn, implies that connected regions are mapped to connected regions, even if the mapping is not one-to-one (Figure 6.1D). X_T can be described as a random variable, and the probability for X_T to attain a value in some region A is transformed to the probability for X_E to attain a value in the region g(A). The conservation of probability enables us to write our first

axiom:

> **Axiom I.** *For any unbiased tracking algorithm g, the probability that the true position X_T has a value in some region A is equal to the probability that the estimated position X_E has a value in the region $g(A)$.*

In the absence of feedback between the pixel grid of the detector and the system being imaged, we have a second axiom:

> **Axiom II.** *For any unbiased algorithm g, the probability for X_E to obtain a particular value is independent of the specific coordinates of the pixel grid. This assumes that there is no aberration (over the field of view) that causes bias in the detected intensities themselves.*

We now combine these axioms to define an essential condition for X_E to represent the tracking results of an unbiased algorithm. Let $\{X_E(i)\}$ be a series of estimated positions of $\{X_T(i)\}$. This series includes time traces that are produced by the tracking algorithm g for different particles. Each $X_T(i)$ can be written as $X_T(i) = \hat{X}_T(i) + a(i)$, where $a(i)$ is the coordinate of the center of the pixel corresponding to $X_T(i)$ and $\hat{X}_T(i)$ is the subpixel position; $\hat{X}_T(i)$ is mapped by the algorithm g to $g(X_T(i)) - a(i) = X_E(i) - a(i) = \hat{X}_E(i)$. Using axiom I we write the conservation of probability (in one dimension for simplicity) as

$$P_T(\hat{X}_T(i))d\hat{X}_T(i) = P_E(\hat{X}_E(i))d\hat{X}_E(i) \tag{6.1}$$

where P is the SPIFF density function and dX is the differential of X. Subscripts E and T refer to the SPIFF obtained for the estimated and true positions. By axiom II, the SPIFF, P_T, is uniform, that is, $P_T(\hat{X}_T(i)) = 1 \; \forall \; \hat{X}_T(i)$. From Eq. 6.1 it then follows that

$$P_E(\hat{X}_E(i)) = \left| \frac{dg^{-1}(\hat{X}_E(i))}{d\hat{X}_E(i)} \right| \tag{6.2}$$

where g^1 is the inverse function of g. The term on the right-hand side of Eq. 2 is the

Jacobian of the inverse function g^1. It assumes that g acts identically in each pixel. For an unbiased tracking algorithm, g is the identity function and thus an essential condition for any tracked data to accurately represent the true positions is

$$P_E(\hat{X}_E(i)) = 1 \tag{6.3}$$

The SPIFF is obtained from tracked data by building a histogram of the shifted positions $\hat{X}_E(i)$ (Figure 6.1). Eq. 6.3 then tells us that deviations of the SPIFF (histogram) from a constant value (i.e., uniform filling) indicate the presence of bias in the tracking algorithm and inaccuracy of the derived coordinates. This indicator is independent of the specific tracking algorithm used and can be applied to any kind of tracked data given a sufficient number of sampled positions (Chapter Appendix, section 6.6.2). Although one can theoretically study the performance of a specific algorithm with simulated PSFs, the exact experimental conditions are never known completely and thus may not be well represented. The SPIFF provides an essential validation test and indicates whether an algorithm produces biased results. Figure 6.1D shows a hypothetical case when inaccuracies in g are manifest as failure of the tracked positions to fill the pixels.

Figure 6.2 shows an example of the SPIFF for particle positions that are obtained from the CrockerGrier center-of-mass algorithm [71] applied to experimental data. The experimental system consists of a moderately dense quasi-2D aqueous suspension of colloid particles (diameter $1.57 \pm 0.02\,\mu\text{m}$) [199]. A digital camera was used to record the particle motions with temporal resolution of 200 frames per second. The image analysis was performed using a Python implementation of the CrockerGrier method [71]. We see that the tracked positions cluster toward the centers of the pixels. This deviation from a uniform distribution can be caused by various factors, including intensity overlaps of nearby particles and background noise. Regardless of the cause, the SPIFF shows that the subpixel positions are biased. This inaccuracy is important and different from the precision of the algorithm. Loss of precision

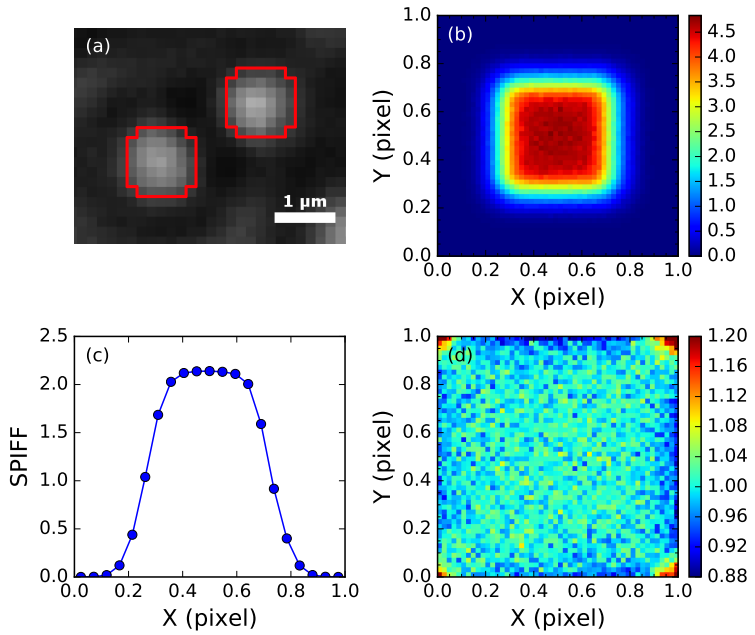

Figure 6.2: Illustration of pixel locking and correction with experimentally acquired images of colloid particles in a quasi-2D suspension. (A) Image of two colloid particles. The window functions used to localize the particles are marked in red. (B) The SPIFF obtained from a center-of-mass algorithm. (C) Projection of B onto the x axis. (D) The SPIFF after correction. In D the color scale was restricted to 0.88–1.20; the full corrected SPIFF is shown in the Chapter Appendix, section 6.6.1, where we discuss consequences of the bias for data interpretation.

usually arises from randomly distributed errors, whereas inaccuracy can arise from correlations. In the Chapter Appendix, section 6.6.1 we show how the inaccuracy displayed in Figure 6.2 introduces artificial memory to colloidal dynamics on short time scales (0.1 s, less than the time between collisions).

6.3 Using the SPIFF to Correct Bias in Tracked Positions

The errors discussed above can be removed by inverting the mapping associated with the tracking algorithm: $X_T = g^{-1}(X_E)$. The explicit form of g^{-1} is easily found noting that the Jacobian of g^{-1} is simply the SPIFF itself. In 1D it is a matter of integration of P_E in Eq. 6.2 to obtain g^{-1}, under the condition that g^{-1} is monotonic. In higher dimensions this task is also possible under certain constraints. In 1D the mapping g^{-1} is from a scalar to a

scalar, whereas in higher dimensions it maps a vector to a vector. Knowledge of the Jacobian of the transformation provides us with a scalar quantity, which is generally insufficient to reconstruct the vector mapping. However, when the mapping has a specific symmetry (or is bounded by constraints), we can simplify the integration of P_E. In the Chapter Appendix, section 6.6.3 we show how to obtain g^{-1} for several cases. In the following we assume P_E is factorizable–that is, $P_E(x, y) = P_E(x)P_E(y)$; in this case, the Jacobian in Eq. 6.2 is also factorizable, and we integrate over the dimensions independently (Chapter Appendix, section 6.6.3). This process is indicated schematically in Figure 6.1D. Inverting the mapping is always possible if g is injective, for example when a tracking algorithm has only systematic bias. However, when the bias is not systematic, noise can distort the SPIFF to an extent that there is a loss of information, and there is no longer a one-to-one relation between X_E and X_T.

In the following two subsections, we use simulated data to illustrate two common situations (undersampling and overlapping PSFs) that give rise to artifacts in particle tracking and show how the SPIFF can be used to correct them. We consider a third situation (background noise) in the Chapter Appendix, section 6.6.4. In the examples we use the Crocker-Grier method [71] as the tracking algorithm, and a Gaussian for the PSF, but our findings apply to any tracking output without needing knowledge of the algorithm.

6.3.1 Nyquist-Shannon Bias

In signal processing the NyquistShannon sampling theorem states that a band-limited function can be perfectly reconstructed from a series of samples if the bandwidth B is less than or equal to half the sampling rate [200]. A similar restriction applies for correct determination of the location of the center of a (point) light source [190]. The intensity of the point source must span a sufficient number of pixels to properly reconstruct the position of the center. If the Crocker-Grier method [71] is used, undersampling leads to systematic errors in the tracking algorithm [191, 192]. These errors can be detected and corrected for sufficiently

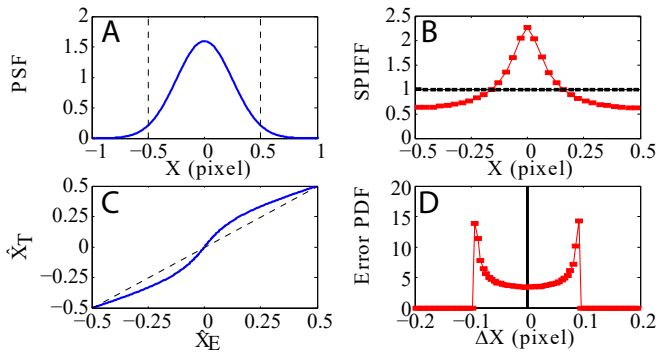

Figure 6.3: Tracking error resulting from undersampling and its correction. (A) Gaussian PSF in the x direction with $\sigma = 0.25$ (blue curve). Dashed vertical lines represent the boundaries of a pixel where the maximum of the PSF is located. Over 90% of the intensity is located within a single pixel. (B) SPIFF (x direction) for locations obtained by Eq. 6.6 (red) and SPIFF (black) for corrected locations. (C) g^{-1} as obtained from simulated data (thick line) and for the identity function expected for an unbiased tracking algorithm (dashed line). (D) Error probability density function for estimated (red) and corrected (black) locations. The error values are computed by comparison with the true positions of the particles (i.e., ΔX is the difference between the blue solid and black dashed lines in C). The distribution of the errors for corrected locations is centered at 0 and has a second moment of 10^{-7} pixels^2.

large signal-to-noise using the SPIFF.

To demonstrate the NyquistShannon bias, we generate 10^6 random positions $X_T = (x_c, y_c)$ and for each position generate pixel intensities that correspond to a Gaussian PSF with SD σ:

$$I_{k,m} = \frac{1}{4}\left[\mathrm{erf}\left(\frac{k+\frac{1}{2}-x_c}{\sqrt{2}\sigma}\right) - \mathrm{erf}\left(\frac{k-\frac{1}{2}-x_c}{\sqrt{2}\sigma}\right)\right] \times \left[\mathrm{erf}\left(\frac{m+\frac{1}{2}-y_c}{\sqrt{2}\sigma}\right) - \mathrm{erf}\left(\frac{m-\frac{1}{2}-y_c}{\sqrt{2}\sigma}\right)\right] \tag{6.4}$$

To model undersampling we used $\sigma = 0.25$ pixels, such that the intensity is mainly concentrated in one pixel (Figure 6.3A).

The center-of-mass algorithm for determining the position of the center of a (point) light source is a simple averaging procedure. Let $I_{k,m}$ be the recorded intensity in pixel (k, m), and choose the coordinate system such that the maximum intensity of the light source (in the absence of other nearby emitters) is at pixel $(0, 0)$. Here, the size of a pixel is taken to be 1 and the pixel centers have integer locations. The position of the center of the light source

(x, y) is then estimated to be [71]

$$(x, y) = \frac{\sum_{k=-w}^{k=w} \sum_{m=-w}^{m=w} (k, m) I_{k,m}}{\sum_{k=-w}^{k=w} \sum_{m=-w}^{m=w} (k, m)} \tag{6.5}$$

where the size of the region (in pixels^2) that is used to determine the position of the particle is $(2w + 1) \times (2w + 1)$. We use $w = 10$.

The factorizability of $I_{k,m}$ and the form of Eq. 6.5 allow treating the x and y directions separately. A transformation $X_E \rightarrow \hat{X}$ is performed and the SPIFF is plotted in Figure 6.3B. Owing to the symmetry of the problem and the factorizability of the PSF, we present our analysis in terms of only the x direction; statistically identical results hold for the y direction. Figure 6.3B shows a large deviation from the uniform distribution, indicating bias in the tracking; the $\hat{X}_E(i)$ are systematically shifted toward the center of the pixel. This arises because discrete pixels effectively average the PSF within their interiors, so that undersampling results in a loss of information about the PSF. Because we generated the simulated data, we can determine the actual errors made in the detection of particle positions. The distribution of errors is bimodal with peaks at ± 0.1 pixels (Figure 6.3D).

The SPIFF can be constructed without knowledge of the true particle positions and thus can easily be used to test for bias. Moreover, for the case of undersampling the bias is systematic and thus can be corrected. Due to the symmetry of the PSF and the form of Eq. 6.5 the point $X_T = (0, 0)$ at the center of a given pixel is a fixed point of the mapping algorithm. The existence of such a fixed point establishes it as a lower bound for the integration of $P(\hat{X}_E)$. Therefore, the true particle position is given by

$$\hat{X}_T = g^{-1}(\hat{X}_E) = \pm \int_0^{\hat{X}_E} P(\hat{X}'_E) d\hat{X}'_E \tag{6.6}$$

The integral on the right-hand side of Eq. 6.6 is the cumulative distribution; it is easily obtained from the estimated values $\hat{X}_E$ by calculating the fraction of estimated values in the range $(0, \hat{X}_E)$ relative to the total number of estimated positions. The minus sign in Eq. 6.6

applies for the case $\hat{X}_E < 0$. We plot the inverse transformation as obtained from sampling 10^6 different positions of the particle in Figure 6.3C. $\hat{X}_T$ deviates strongly from the identity function (dashed line). We calculate a new SPIFF for the corrected positions and find that it is uniform as desired (Figure 6.3B, horizontal line with black symbols). Correspondingly, the error distribution of the corrected positions is almost a δ-function at 0 (Figure 6.3D, black). The precision of the corrected positions is determined by the density of the samples and is 1 part in 10^3. These results demonstrate the benefit of the SPIFF with respect to both detecting errors and correcting them by inverting the mapping. The ability to correct errors arising from undersampling exists because we can compensate for the lack of information in a single frame with statistical information accumulated over time or across the ensemble. The SPIFF pools the information from many determinations of the PSF center, which, in turn, enables detection and correction of errors.

6.3.2 Intensity Overlap of Adjacent Objects

In the previous example, the bias in the tracking algorithm was systematic. We now show how actively generating such errors coupled with the SPIFF correction technique can help to overcome the effect of a nonsystematic bias. To this end, we consider pixel intensities that result from multiple emitters that are in close proximity. The resulting overlap of the PSFs affects the inferred locations of the particles by asymmetrically altering parts of the individual particle images. This form of error and means to address it have been considered previously in measurements of interactions between colloidal particles [200]. Although no general method is likely to be able to correct this error in all situations, the approach that we discuss shows promise for certain experimental regimes.

To demonstrate the effect of overlap and its correction via the SPIFF, we do the following. We construct a pair of particles with a separation of 15.2 pixels and assign them Gaussian PSFs with $\sigma = 1.96$ pixels (Figure 6.4 A and B), a separation large enough that one would not suspect that intensity overlap plays a role in the tracking process. For this fixed distance

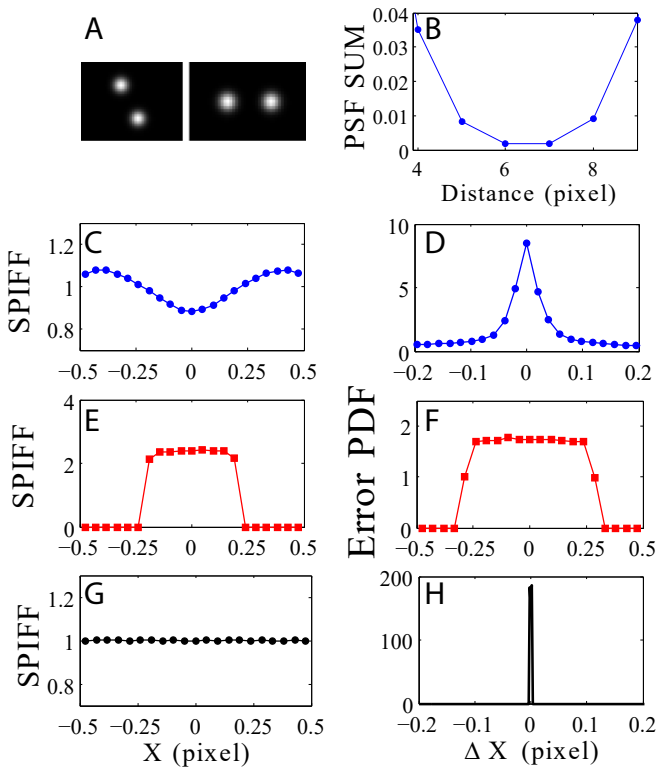

Figure 6.4: Tracking error resulting from PSF overlap of two particles and its correction. (A) Two different realizations of the system of two particles with Gaussian PSF ($\sigma = 1.96$ pixels) and center-to-center distance of 15.2 pixels. The intensity was scaled such that the pixel value with maximal intensity is equal to 1 (arbitrary units) and the overlap of the two PSFs is not detectable by eye. (B) Sum of the PSFs along the center-to-center distance showing nonzero intensity at the midpoint between the particles. (C and E) SPIFF for the estimated particle positions (x direction) obtained with $w = 9$ (C) and $w = 2$ (E) in the center-of-mass algorithm. (D and F) Error probability density functions for the estimated positions, corresponding to C and E. (G) SPIFF after correcting the positions by inverting the mapping based on the SPIFF in E. (H) Error probability density function corresponding to G.

between the particles we generate 100 different random orientations of the pair. For each of these orientations, we then translate the pair relative to the pixel grid by allowing the center-of-mass to undergo Brownian motion for 100 steps with step sizes obtained from a Gaussian distribution with zero mean and SD of 0.2 pixels in x and y. Given the resulting simulated intensities, we track the particle positions using Eq. 6.5 with $w = 9$.

We plot the SPIFF for the x direction in Figure 6.4C. There is a clear preference for positions toward the edges of the pixel. Figure 6.4D shows the distribution of errors. Although the peak of the distribution is at zero, there is a significant probability of errors of 0.1 pixel

or larger. In the Chapter Appendix, section 6.6.1 we show that for this case the inferred dynamics is non-Brownian, in contradiction with the true simulated motion. The correlated interaction of the particle images in the tracked results gives a mean square displacement that varies nonlinearly with time. In fact, an order parameter for directional motion [201] indicates an inertial effect. Both effects are inconsistent with the simulated motion.

In the previous example, with systematic bias, we corrected the positions by transforming the SPIFF into a uniform distribution, but the nonsystematic bias that derives from overlaps prevents us from using the same procedure. Instead, we decrease w in the tracking algorithm and consequently decrease the effect of the intensities coming from nearby particles. Figure 6.4 E and F show the outcome of performing center-of-mass analysis with $w = 2$ (vs. $w = 9$ used in Figure 6.4 C and D; see also the Chapter Appendix, section 6.6.5). Figure 6.4E shows that the deviations from a uniform distribution are larger than the ones shown in Figure 6.4B, and Figure 6.4F shows that limiting the number of pixels included significantly broadens the error distribution and thus the probability of significant errors. Nevertheless, the SPIFF can now be used to invert the mapping as in the previous example. Upon doing so, the SPIFF becomes uniform (Figure 6.4G), and the errors are corrected (Figure 6.4H).

We have implemented the strategy outlined in this section for the experimental data shown in Figure 6.2 and the Chapter Appendix, Figures 6.6 and 6.7. From the images we selected colloid pairs in close proximity. The presence of additional nearby particles limits the window size that can be chosen for the tracking, which results in a strong systematic bias that we can correct with the SPIFF. The results show a significant improvement in the mean square displacement as a result of SPIFF correction.

6.4 Noise and the CRLB

Although we have shown that the SPIFF enables nearly perfect reconstruction of particle positions in the absence of noise, the presence of noise limits the certainty in the particle

positions. This limit, known as the CRLB [202], depends on the PSF and the type of noise present. For an unbiased estimator, the CRLB is $\mathrm{Var}(X_T) \leq 1/\mathrm{I}(X_T)$, where $\mathrm{I}(X_T)$ is the Fisher information. The unbiased CRLB is often used as the standard for evaluating particle-tracking algorithms [203–207]. In this section, we consider the effect of noise on the performance of the SPIFF in correcting errors and show that, because it is a biased estimator, it can actually achieve a precision that exceeds the standard unbiased CRLB.

To this end, we performed simulations like those in *Using the SPIFF to Correct Bias in Tracked Positions* (section 6.3) and *Nyquist-Shannon Bias* (section 6.3.1) except that now the intensity at each pixel (k, m) is drawn randomly from a Poisson distribution with a mean of $N_S\, I_{k,m} + N_B$, where N_S is the total number of photons expected per particle (for the whole image), $I_{k,m}$ is obtained from Eq. 6.4, and N_B is the average intensity of the background noise. We set N_B to be 10 photons (per pixel), similar to other studies [205], and we study the performance of the algorithm as we vary N_S from 10^2 to 2×10^4 photons (per image). We then estimate the particle positions by applying the Crocker-Grier method with the SPIFF correction. The results are shown in Figure 6.5. In Figure 6.5A the optimal window size (Chapter Appendix, section 6.6.6) was used for each particle size (σ), and we see that the precision is close to the CRLB. In Figure 6.5B we observe the case of a minimal window size ($w = 1$), which is relevant for *Using the SPIFF to Correct Bias in Tracked Positions* (section 6.3), and *Intensity Overlap of Adjacent Objects* (section 6.3.2). We see that for some particle sizes (σ values) our method achieves better precision than the unbiased CRLB. This is possible because the Crocker-Grier algorithm is biased.

We now want to understand this result mathematically. In general, the Cramér-Rao bound is given by

$$\mathrm{Var}(X_T) \geq \frac{(d\langle g(X_T)\rangle/dX_T)^2}{\mathrm{I}(X_T)}, \tag{6.7}$$

where $\mathrm{I}(X_T)$ is the Fisher information as above, and $\langle g(X_T)\rangle$ is the output of the tracking algorithm (the subpixel part of the position estimate), averaged over noise. In the case of an unbiased algorithm, there is a one-to-one mapping between the true positions and the

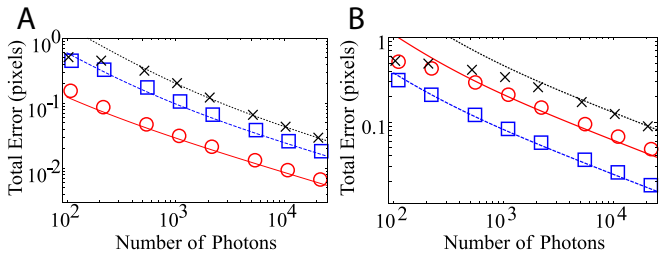

Figure 6.5: Precision of the corrected Crocker-Grier center-of-mass for simulated data with experimental-like noise compared with the CRLB. The results are averaged over 104 images; the number of photons is per image, not per estimating window. In each case the symbols represent the simulation results and the lines represent the unbiased CRLBs. (A) Positions are estimated with optimal window sizes of $2\sigma \times 2\sigma$ for each particle size (Chapter Appendix, section 6.6.6), as specified by σ in the Gaussian PSF: $\sigma = 0.5$ (red circles), $\sigma = 1.5$ (blue squares), and $\sigma = 2.5$ (black crosses), all in pixels. (B) Positions are estimated with a fixed window size of 3×3 pixels ($w = 1$); $\sigma = 1$ (blue squares), $\sigma = 1.5$ (red circles), and $\sigma = 2$ (black crosses).

output of the tracking algorithm, so the numerator on the right-hand side is 1. For a biased estimator, we can have $|d\langle g(X_T)\rangle/dX_T| \leq 1$. Specifically, for the case of the Crocker-Grier algorithm, we have seen that the algorithm systematically biases the positions toward the center of the pixel, such that $|d\langle g(X_T)\rangle/dX_T| \leq 1$. By itself, this increase in precision is not useful because the accuracy is lower. However, when we correct the results with the SPIFF, we are able to remove the systematic error and take advantage of the decrease in variance implied by the biased CRLB. The SPIFF actually mitigates this decrease, but not so much as to lose the effect. In this way, we exceed the unbiased CRLB and thus the performance of most tracking algorithms. In this regard, it should be noted that maximum-likelihood methods also approach the CRLB [205], but they are computationally costly. Here, we achieve comparable or better results with minimal computational effort—both the Crocker-Grier algorithm and the SPIFF correction are fast. A more extended discussion of the role of noise and the removal of its effects can be found in the Chapter Appendix, section 6.6.7.

6.5 Conclusions

Algorithms that use information from PSFs to localize emitters with subpixel resolution now play an essential role in many different areas of science [180, 199, 201, 208–211]. Here we propose a simple validation method that only requires knowledge of the estimated particle positions. Our approach is based on the SPIFF. Because the positions of the objects being imaged are independent of the detection system, the SPIFF is a uniform distribution when the tracking algorithm is unbiased. The SPIFF is essentially a measure of pixel locking [196], and we show how its quantification can be used to invert the tracking algorithm mapping to correct errors.

Our key physical insight is that ergodicity of the physical processes being imaged allows pooling information from multiple times and/or emitters that compensates for limited sampling of the PSF over pixels (Nyquist-Shannon bias) and/or intensities (e.g., owing to a confounding background signal or nonsystematic noise). This additional information allows us to introduce a unique strategy for treating errors that arise when pixel intensities derive from multiple emitters [186], which is common in dense systems [210]. In such cases, we limit our use of image information to the pixels nearest to the peak intensities; although this introduces a systematic pixel-locking bias (error), we demonstrate how that effect can be removed by integrating the SPIFF. Indeed, this strategy enables us to exceed the unbiased Cramér-Rao bound [73, 188] for a given signal-to-noise. The noise properties of this strategy differ fundamentally from those of the standard strategy of increasing the range of pixels included for each emitter. There is of course a limit to this procedure—if particles are too close, their signals cannot be separated, and the correction procedure homogenizes the SPIFF but does not yield accurate positions. We characterize this limit as a function of the width of the PSF and the extent of the noise in the Chapter Appendix, Figures 6.18–6.20.

Remarkably, our procedure for detecting and correcting systematic errors requires only the tracked positions and does not require explicit knowledge of the PSF or independent knowledge of the extent to which the intensities from different emitters are overlapping. We

have illustrated our approach with the center-of-mass method [71] owing to its popularity. However, our results are general and applicable to the output from all tracking algorithms, regardless of the source of the data or the mathematical operations performed.

The main limitations of our approach are that the particle positions must be well sampled with respect to the pixel boundaries, and the particle positions must be consistently generated from one pixel to another. We note that experimental realities (optical aberrations, variations in illumination and focus, etc.) can affect the latter. In our experience, proper calibration of the imaging system can mitigate these issues sufficiently to construct the SPIFF, but there are other situations that we have not explored and therefore for which we cannot guarantee the accuracy of the error correction (e.g., tracking 3D data where the focusing and relative particle positions create new challenges). It is also important to note that the SPIFF correction we propose does not solve all problems related to extraction of data from trajectories. For example, it is not designed to deal with nonsystematic errors such as those that arise from mixing of information coming from different sources. Nevertheless, we believe that many experiments will be in a regime that permits application of the SPIFF approach.

6.6 Chapter Appendix

6.6.1 Correlations in dynamics arising from particle tracking errors

Here we describe one consequence of tracking errors for interpreting particle dynamics especially when striving for sub-pixel accuracy in localization. While the static properties that are described in the main text concern data from a single frame, the dynamics can be influenced by errors correlated over several frames. For example, when the particle displacement between two successive frames is small compared to the pixel size, the true locations of the particle in both frames can be shifted in a systematic fashion. This gives rise to artificial correlations. In the following we provide several examples of such behavior for the systems

discussed in the main text.

The tools that we use for quantification of the dynamical properties of the estimated motion are the mean squared displacement (MSD = $\langle (X(t) - X(0))^2 \rangle$, where $\langle \ldots \rangle$ indicates ensemble averaging, and the relative angle distribution, $P(\theta; \Delta)$. While characterization of a trajectory with the MSD is a standard method, the use of $P(\theta; \Delta)$ has only recently been introduced [201]. $P(\theta; \Delta)$ is defined as follows: a displacement of a particle in a time interval Δ is defined as $V(t; \Delta) = X(t+\Delta) - X(t)$, where $X(t)$ is the position of the particle recorded at time t. The angle $\theta(t; \Delta)$ is defined as

$$\theta(t; \Delta) = \cos^{-1} \left(\frac{V(t; \Delta) \cdot V(t + \Delta; \Delta)}{|V(t; \Delta)| \, |V(t + \Delta; \Delta)|} \right), \tag{6.8}$$

where the numerator is a dot product. By computing θ for all possible time points t in a given particle trajectory, and repeating the procedure for all particles, we can construct the distribution of the angle θ given the temporal interval Δ. This distribution is $P(\theta; \Delta)$; it is capable of elucidating subtle properties of the motion. In Burov et al. [201] several properties of $P(\theta; \Delta)$ are described for different underlying transport mechanisms. We now explore the dynamic properties of some of the examples considered in the main text.

Experimental data for a quasi-2D colloidal suspension

The system that we study is the same as the one used to generate Figure 6.2 in the main text. We show an example of the raw data in Figure 6.6. In Figures 6.7 and 6.8, we construct the SPIFF and the MSD for two choices of the Crocker-Grier algorithm window size. In both cases, the SPIFF has an inhomogeneous profile and consequently the positions of all the particles, before correction, include systematic tracking errors. Given the size of the particles (1.57 µm diameter), we expect simple diffusion. In the absence of correction, the tracking error causes a deviation from the expected linear behavior of the MSD that is quite noticeable at short times. Note that the pixel locking and the short-time deviation of

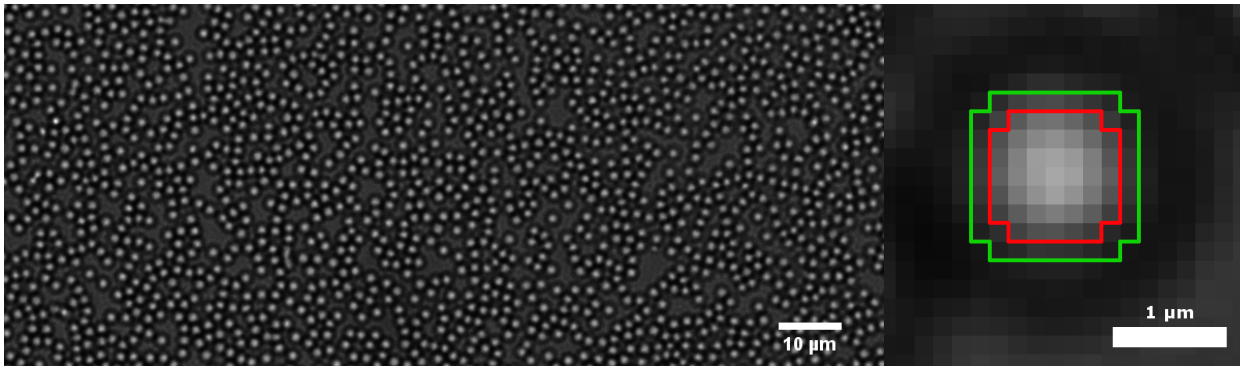

Figure 6.6: Raw image used to obtain the colloid tracking data used in Figure 6.2 in the main text. Particles are 1.57 µm silica beads sandwiched between coverslips separated by $<$ 2 µm. The density in this quasi-2D system corresponds to an area fraction of 0.34. (left) One third of the field of view; the full field of view extends an amount equal to the view shown to the left and right. (right) Expanded view of a single colloid particle showing the window sizes used for center of mass localization. The red outline represents a window of 7 pixels ($w = 3$) while the green outline represents a window of 9 pixels ($w = 4$).

the mean square displacement (MSD) from the linear fit are less pronounced in Figure 6.8 compared with Figure 6.7, but intensity overlaps can make it problematic to increase the window size, as discussed in the main text. With SPIFF-based correction, both the MSD plots are linear as expected, demonstrating that the correction procedure eliminates the artificial correlations in particle displacements.

Mean-square displacement (MSD) simulation

In Section 6.3.1 of the main text we treated the Nyquist-Shannon bias that arises when the point spread function (PSF) is narrower than a pixel. To generate simulated dynamics to illustrate the effect of this bias on interpretation of the dynamics of a tracked object we repeatedly shift the center of the PSF with respect to its previous position by $(0.03\zeta_1, 0.03\zeta_2)$, where $\zeta_1(\zeta_2)$ is a random variable with a Gaussian distribution (standard deviation $\sigma =$ 1 pixel) with zero mean. The starting points of the trajectories are uniformly distributed over the interior of a pixel. The expected behavior of the PSF center is linear growth of the MSD with time (Figure 6.9, red line). The behavior observed after performing center-of-mass tracking, as described in Section 6.3.1 of the main text, deviates from the true behavior at

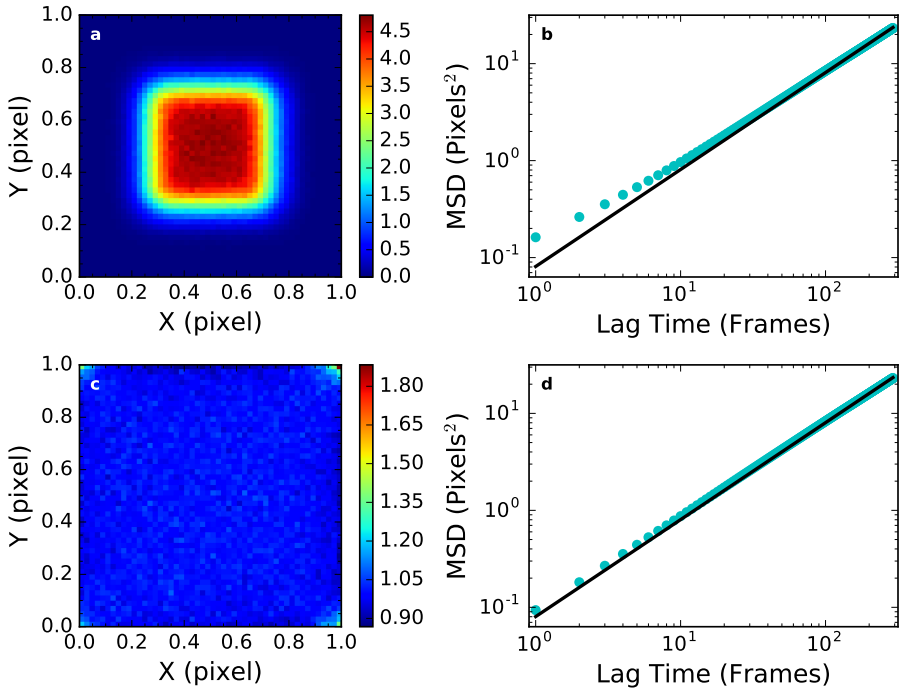

Figure 6.7: The SPIFF and the MSD from the quasi-2D colloidal suspension shown in Figure 6.6: analysis with a window size of 7 pixels ($w = 3$). (a) The SPIFF generated by the localization algorithm. (b) The mean square displacement (MSD) using the positions obtained from the Crocker-Grier algorithm. (c) The SPIFF following correction. (d) The MSD obtained from the corrected positions. Note that the SPIFF is nearly uniform (as shown in Figure 6.2) except for a few pixels in the corners. The black lines in (b) and (d) show the linear behavior of the MSD at long times; they are best fit lines to the last 200 data points in each case. The MSDs shown in (b) and (d) only go to lag times of one third the total time in the experiment.

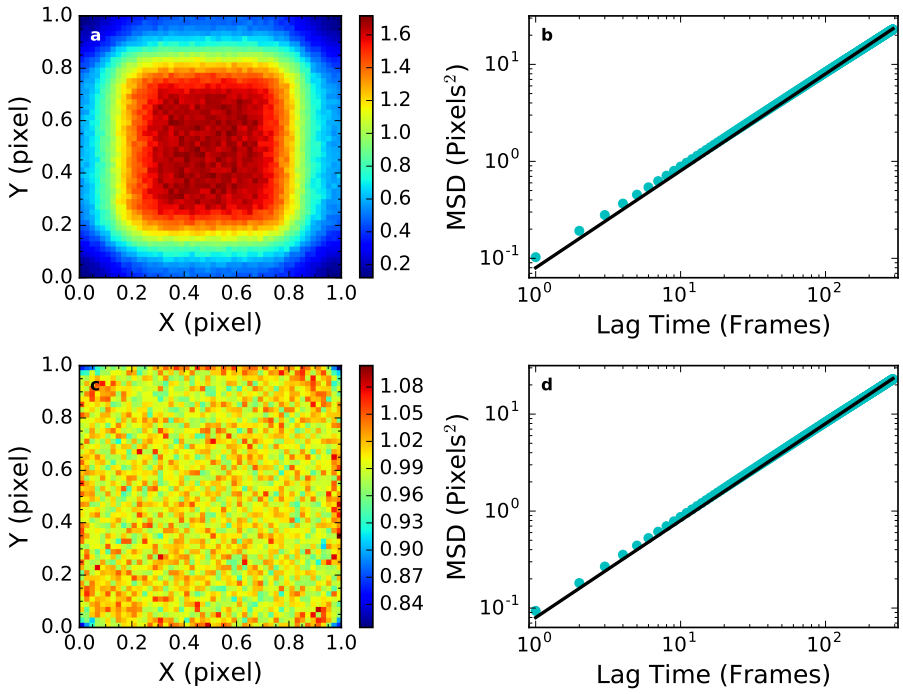

Figure 6.8: Same as Figure 6.7 but with a window size of 9 pixels ($w = 4$).

short times (Figure 6.9, dashed blue line), rendering the MSD non-linear. This phenomenon is also obtained for tracking where the position of the particle is biased towards the center of a pixel in a similar fashion to the one described in Section 6.6.1 of the Chapter Appendix and Section 6.3.2 of the main text. In the simulation described above each true subpixel position is multiplied by 0.7. The result is presented in Figure 6.9 (dotted line). We note that apparent super-diffusion (as opposed to the apparent subdiffusion indicated by the dotted black curve in Figure 6.9) can be attributed to dynamical error [198].

SPIFF correction after restricting the window size

In Section 6.3.2 of the main text we introduced a method for correcting errors that appear due to overlap of the images of neighboring particles. In that method, we intentionally restricted the data used during tracking, resulting in an inhomogeneous SPIFF, and then corrected the ensuing errors by applying the inverse mapping g^{-1} obtained by integrating the SPIFF. Here we show that the original properties of the dynamics (i.e., unbiased dynamics) are restored

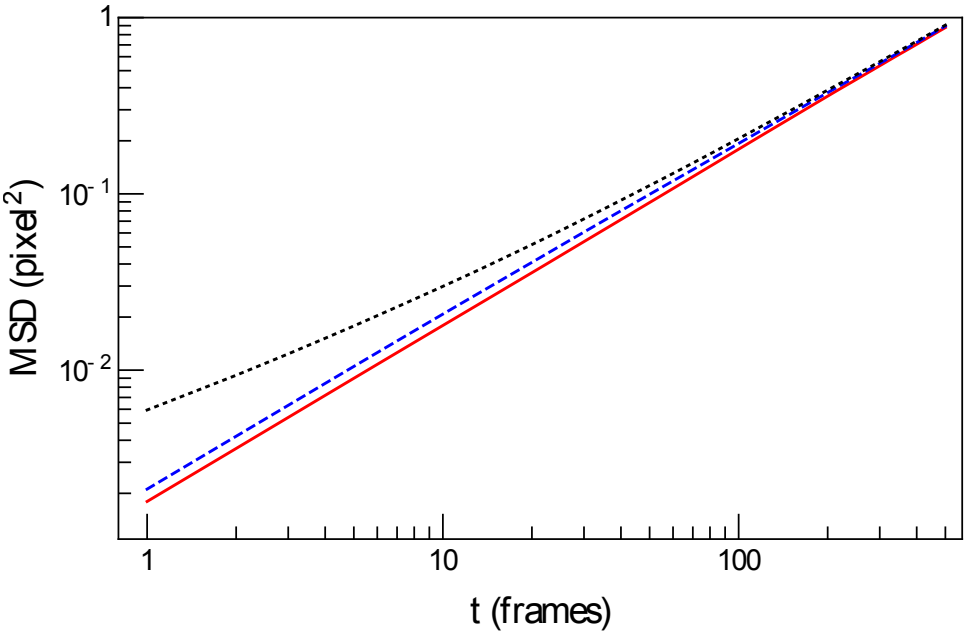

Figure 6.9: The MSD as a function of time for the case of biased tracking. The red line displays the simple diffusion of the PSF center modeled in the simulation, calculated from 1000 trajectories with 1000 samples each. The dashed blue curve shows the behavior for data points obtained from the tracking method as described in Section 6.3.1 of the main text (*Nyquist-Shannon bias*). The dotted black curve shows the behavior of artificial bias towards the center of a pixel as described in Section 6.6.1 of the Chapter Appendix. For large enough t the behaviors coincide and the subpixel resolution errors become insignificant.

by this strategy. In the model presented in Section 6.3.2, the pair of particles move together in a Brownian fashion such that the orientation of the pair is unchanged. We used 1000 trajectories of 1000 samples each to determine the dynamics. Figure 6.10 shows $P(\theta;\Delta)$ for $\Delta = 1$. Figure 6.10a shows the behavior for the tracked positions obtained with the Crocker-Grier algorithm with $w = 10$ pixels. The peak in $P(\theta;\Delta)$ at $\theta = \pi$ indicates a preference for reversals even for the shortest time scale. This definitely is an erroneous result since the true motion is Brownian and $P(\theta;\Delta)$ should be uniform. When we limit the algorithm to $w = 2$, the correlations become more pronounced (Figure 6.10b). When we correct the tracked positions, $P(\theta;\Delta)$ becomes uniform (Figure 6.10c), which is the expected distribution for Brownian dynamics. This result shows that the correction procedure implemented in the main text also improves and corrects the statistical properties of the dynamics.

6.6.2 Precision of the correction procedure

The number of sampled points limits the precision of the correction procedure. Indeed, if only a single position of a particle was recorded it is impossible to properly construct the SPIFF and in turn g^{-1}. In principle the precision depends on the assumption that the sub-pixel region is homogeneously covered by N different positions of a particle (or N different positions of several particles). This assumption fails if the sampled particle position is not changing with time, or is specifically limited to a spatial region smaller than a pixel. Even when this is not the case, the fact that N is finite will impose an additional constraint. Since the positions are randomly chosen homogeneous coverage of the sub-pixel region holds only on average, and random fluctuations will impose small inhomogeneities. The size of the fluctuations in an uncorrelated random coverage is proportional to $1/\sqrt{\mathrm{N}}$. Accordingly, we expect that the error in the SPIFF reconstruction, when photon shot noise is not present, will decay in the same manner. We demonstrate that this is indeed the case numerically in Figure 6.11.

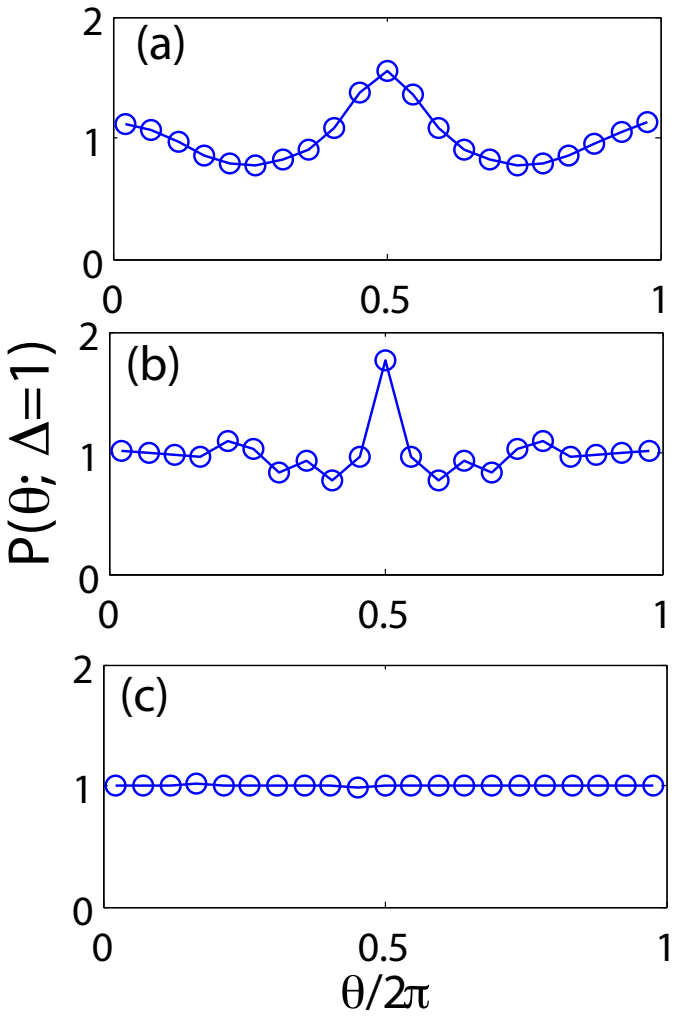

Figure 6.10: Probability density of relative angles, $P(\theta; \Delta = 1 \text{ frame})$, for the system in Section 6.3.2 of the main text (Intensity Overlap). Results shown are for particle tracking with (a) $w = 10$ pixels, (b) $w = 2$ pixels, or (c) $w = 2$ pixels followed by the SPIFF-based correction.

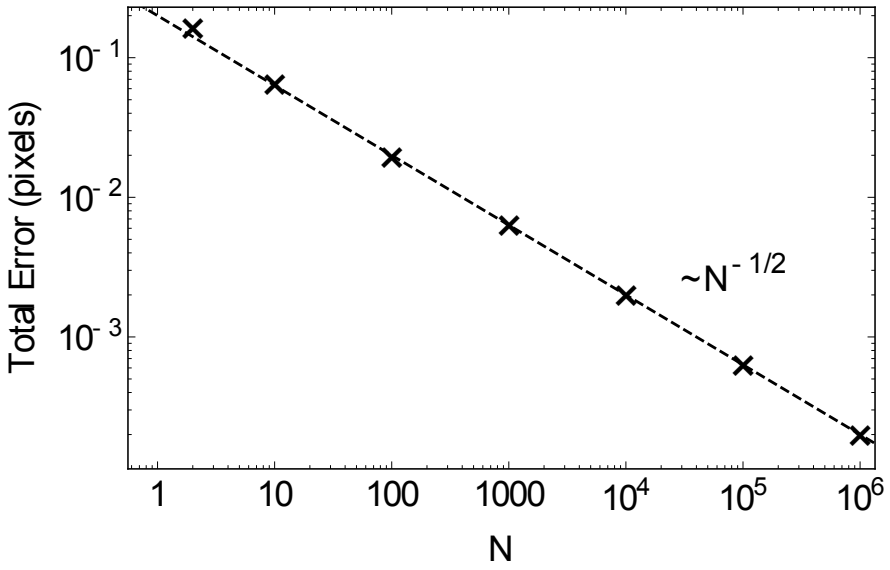

Figure 6.11: Reconstruction error as a function of the number of images, N. The crosses are the result of a simulation averaged over 10^3 different realizations for each N. The dashed line fits the simulated behavior with $0.2\sqrt{\mathrm{N}}$. No photon shot noise was present in this reconstruction process.

6.6.3 The inverse mapping g^{-1}

In the main text we show that the SPIFF provides explicit knowledge of the g^{-1} Jacobian determinant:

$$P_E(\hat{X}_E(i)) = \left| \frac{dg^{-1}(\hat{X}_E(i))}{d\hat{X}_E(i)} \right| \tag{6.9}$$

Here we explicitly discuss how to obtain g^{-1} using the available knowledge of P_E.

The function g^{-1} is a mapping from the space of estimated positions $\hat{X}_E = (x_E, y_E)$ to the space of true positions $\hat{X}_T = (x_T, y_T)$ and is assumed to be injective on the whole space of estimated positions. By writing the Taylor expansion of g^{-1}

$$\begin{aligned} g^{-1}(x_E + \delta x_E, y_E + \delta y_E) &= \begin{pmatrix} g_x^{-1}(x_E + \delta x_E, y_E + \delta y_E) \\ g_y^{-1}(x_E + \delta x_E, y_E + \delta y_E) \end{pmatrix} \\ &= \begin{pmatrix} g_x^{-1}(x_E, y_E) \\ g_y^{-1}(x_E, y_E) \end{pmatrix} + \begin{pmatrix} \frac{\partial g_x^{-1}}{\partial x_E} & \frac{\partial g_x^{-1}}{\partial y_E} \\ \frac{\partial g_y^{-1}}{\partial x_E} & \frac{\partial g_y^{-1}}{\partial y_E} \end{pmatrix} \begin{pmatrix} \delta x_E \\ \delta y_E \end{pmatrix} \end{aligned} \tag{6.10}$$

we see that there are two ingredients for reconstruction of g^{-1}: (i) existence of a specific point (x_E^0, y_E^0) such that $(x_T^0, y_T^0) = g^{-1}(x_E^0, y_E^0)$ is known, and (ii) explicit knowledge of all the entries in the Jacobian matrix. To obtain each ingredient we rely on symmetries in the tracking algorithm, i.e., the mapping g. For the point (x_E^0, y_E^0) we usually take the point (0,0), the center of the pixel. Our starting assumption is that given a symmetric PSF located exactly at the center of a pixel the mapping g will exert no bias, since the bias usually occurs due to nonsymmetric integration of intensities in the nearby pixels. If the SPIFF center of symmetry is not located at the center of the pixel, we assume that the point (0,0) is mapped onto the center of symmetry in the space of estimated positions. Our treatment of the second point also exploits symmetries. Since $\left| dg^{-1}/d\hat{X}_E \right|$ is a one-dimensional quantity, we are limited to cases where symmetries (or constraints imposed on g^{-1}) exist and can effectively reduce the dimensionality of the mapping.

We now describe two cases where the assumed symmetries enable explicit construction of g^{-1}. The first case is a mapping that (i) transforms straight lines in the space of true positions to straight lines in the space of estimated positions and (ii) preserves the orientation of those lines with respect to the x and y axes. One can imagine such a transformation as a mapping that compresses everything towards the center of each pixel (fixed point (0,0)). With this mapping some regions can be distorted more than others as long as conditions (i) and (ii) are conserved. Performing the integration in the space of estimated positions over the rectangle $(0, x_E) \times (0, y_E)$ yields an area of $x_T y_T$ in the space of true positions since the boundaries in the space of estimated positions are straight lines and are transformed to straight lines in the space of true positions. Property (ii) of the mapping g ensures that the rectangle boundaries coincide with the axes in the space of true positions. Since integration over $(0, x'_E) \times (0, y_E)$ corresponds to $x'_T y_T$ and integration over $(0, x''_E) \times (0, y_E)$ corresponds to $x''_T y_T$, we see that the any mapping that fulfills (i) and (ii) decouples the treatments of the x and y axes in the pixel. The functions g_x^{-1} and g_y^{-1} in Eq. 6.10 depend only on x and y, respectively.

A second example is provided by the case of rotational symmetry; the mapping g from the space of true positions to the space of estimated positions depends only on the distance of (x_T, y_T) from the center of the pixel. For such a case, integration over a circle with a center of the space of estimated positions at (0,0) and a radius R_E, corresponds to a circle in the space of true positions with a center at (0,0) and a radius R_T (see Figure 6.12). The radius R_T is deduced from the outcome of the integration in the space of estimated positions, A_R, by the simple formula $R_T = \sqrt{A_R/\pi}$. Any point (x_E, y_E) that is at distance R_E from the origin is transformed to a point (x_T, y_T) that is distance R_T from the origin and lies on the same line as the line that crosses (x_E, y_E) and (0,0). When the radius R_T is greater than 1/2, the circle in the space of true positions will include points outside the pixel. Since those points are not part of the domain of g, they cannot appear in the space of estimated positions. This phenomenon will manifest as regions in the space of estimated positions where the SPIFF is zero, similar to the example in Figure 6.1E of the main text. The mapping is always between a circle in the space of estimated positions to a circle in the space of true positions while only the points that are bound to a single pixel in both spaces are transformed. The correspondence will be the intersection between a circle and a square in the space of estimated positions and the intersection between a circle and a square in the space of true positions (see Figure 6.12).

It should be possible to deduce procedures for inverting additional mappings with other symmetries (e.g., elliptical) based on the information in the SPIFF. The general idea is the same: the symmetries of the mapping allow us to reduce the correspondence between the points in the spaces of estimated and true positions to a one-dimensional correspondence between the areas in the two spaces. The symmetries of the mapping g depend on the specific tracking algorithm and are obtained by exploration and determination of the bias that the algorithm imposes on theoretically constructed images.

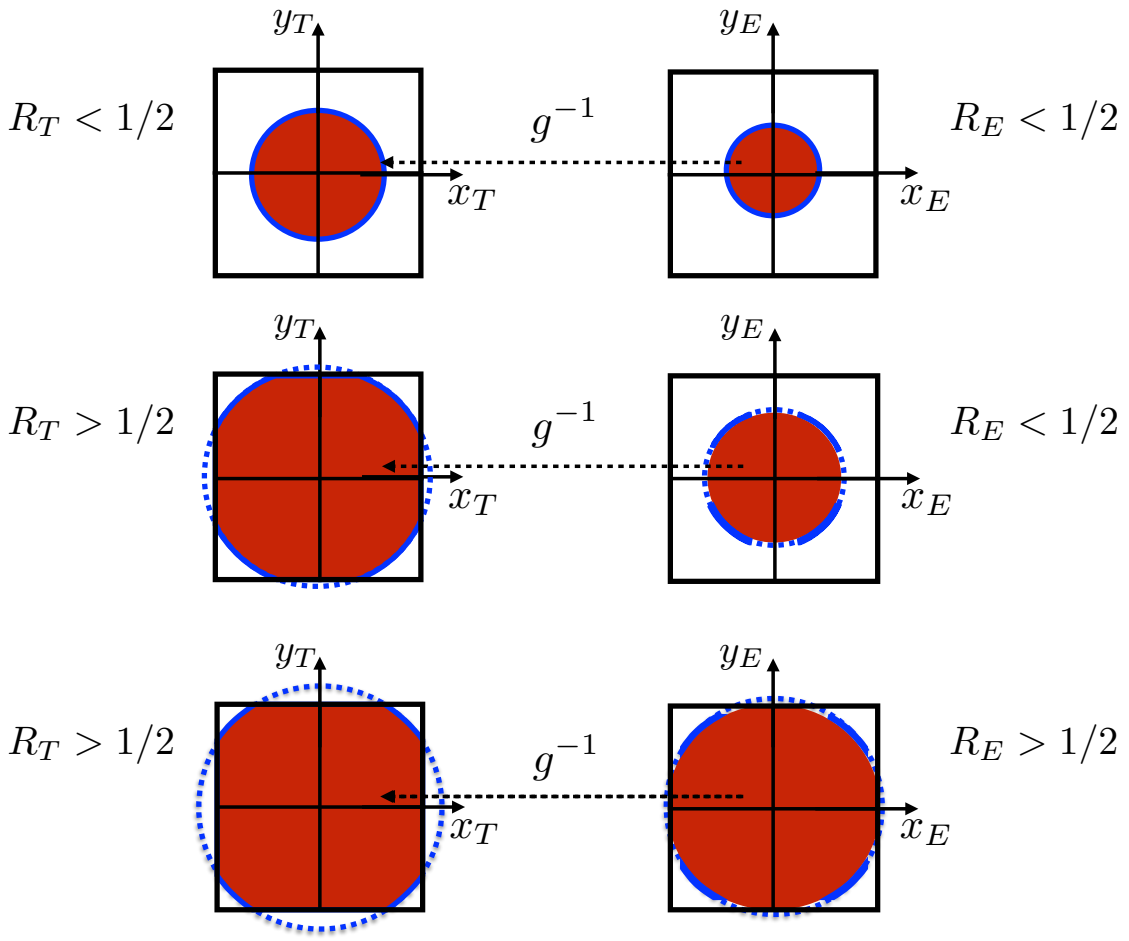

Figure 6.12: Example of a mapping g^{-1} with rotational symmetry. A circle in the space of estimated positions is transformed to a circle in the space of true positions. The area of integration in the space of estimated positions (red, right) is transformed to an area in the space of true positions (red, left) under the constraint that this area is inside the boundary of a single pixel (black square). The correspondence between the areas relates the boundary of the circle in the space of estimated positions (blue, right) to the boundary in the space of true positions (blue, left), i.e., g^{-1}. For the situations when the corresponding radius in the space of true positions, R_T, is greater than 1/2, part of the circle boundary is located outside the pixel in the space of true positions (dotted blue, left). Those points may or may not be inside a single pixel in the space of estimated positions (dotted blue). Regardless of the value of R_E, the value of the SPIFF in the space of estimated positions for such points (dotted blue) must be zero since the corresponding points in the space of true positions are outside of the domain of g.

6.6.4 *Effect of background noise*

Here we examine the effect of background noise on the reduction of trajectory data. It is known that background noise causes the center-of-mass algorithm to bias the estimated locations of the particles toward the center of a pixel [71]. As in Section 6.3.1 of the main text, we generate simulated data with a Gaussian PSF (Figure 6.13a); in this case, $\sigma = 2.5$, and we scale the intensities by multiplying the values by a factor of 10. In addition, we add a small amount of Gaussian noise with mean 0.1 and standard deviation 0.05 to all the pixel intensities. We estimate the positions with the Crocker-Grier method as above (with $w = 10$). The resulting SPIFF (x-direction) is plotted in Figure 6.13b. The background noise biases X_E (and consequently $\hat{X}_E$) towards the pixel centers, and the SPIFF goes to zero near the pixel boundaries. The error distribution is plotted in Figure 6.13d. The errors in the positions are highly non-Gaussian in the range $0.1 < X < 0.1$, in contrast to the Gaussian distribution that one would expect if the errors were uncorrelated. We invert the mapping by integrating the SPIFF to obtain Figure 6.13c. After using g^{-1} to correct the estimated positions, the SPIFF becomes uniform (Figure 6.13b, horizontal line with black symbols). Moreover, the error distribution narrows significantly (Figure 6.13d) and becomes Gaussian with a standard deviation (0.018). Thus, even with random noise in the data, the SPIFF can be used to both detect and correct biases in the tracking algorithm.

6.6.5 *The effect of undersampling*

Care must be used in implementing the strategy of decreasing the window size w to avoid introducing the undersampling (Nyquist-Shannon) bias discussed in the main text. The estimated center of a one-dimensional Gaussian with a center at $x_c = 1/2$, $g_{w,\sigma}(1/2)$, is, according to Eq. 6.6 of the main text,

$$g_{w,\sigma}\left(\frac{1}{2}\right) = \frac{(w+1)\,\mathrm{erf}\left(\frac{w}{\sqrt{2}\sigma}\right) - w \cdot \mathrm{erf}\left(\frac{w+1}{\sqrt{2}\sigma}\right)}{\mathrm{erf}\left(\frac{w}{\sqrt{2}\sigma}\right) + \mathrm{erf}\left(\frac{w+1}{\sqrt{2}\sigma}\right)} \tag{6.11}$$

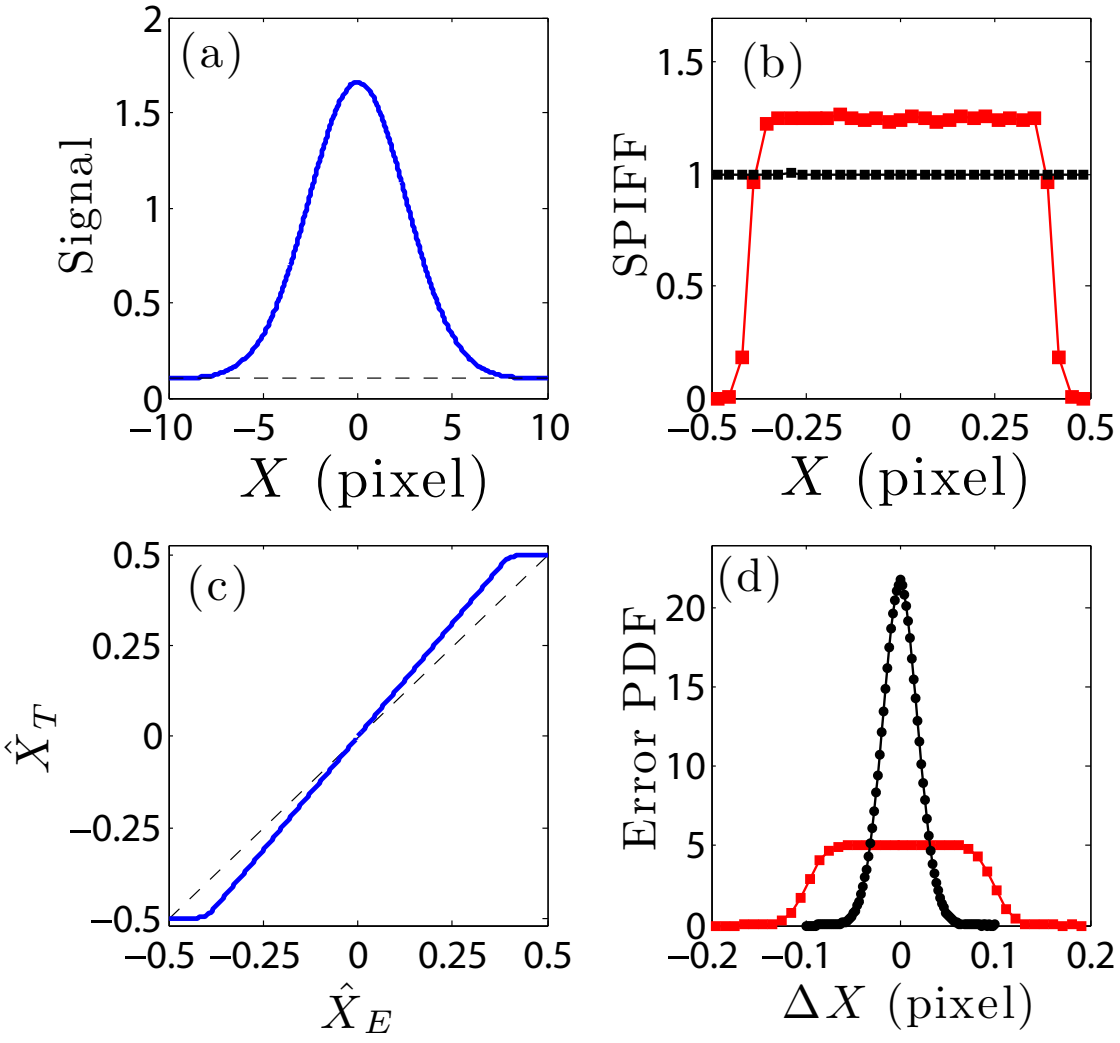

Figure 6.13: Tracking error resulting from background noise and its correction. (a) The signal obtained from a Gaussian PSF (x-axis) with $\sigma = 2.5$ (thick line) and background noise. The dashed line represents the mean value of the (non-zero) background noise. (b) SPIFF (x-direction) for estimated (red squares) and corrected (black squares) locations. (c) g^{-1} as obtained from simulated data (thick line) and prediction for the identity function expected for unbiased data (dashed line). (d) Error probability density function for estimated (red squares) and corrected (black circles) locations.

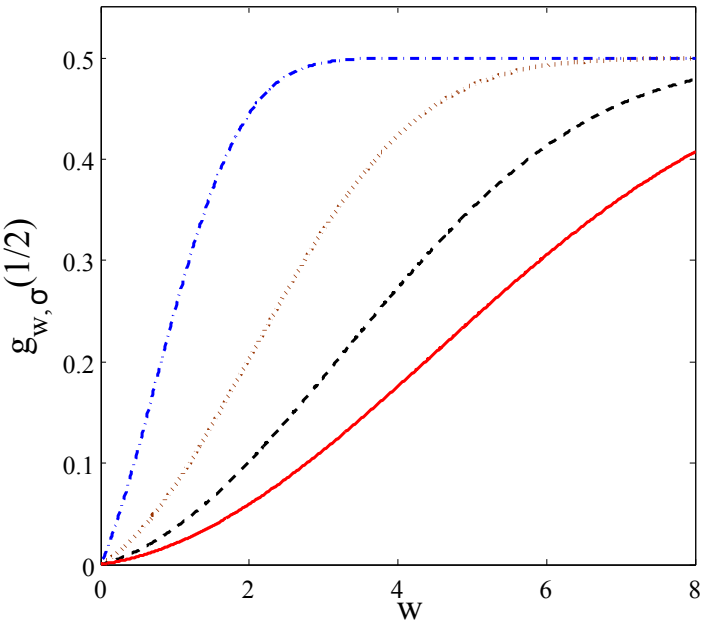

Figure 6.14: Minimal number of pixels needed for the Crocker-Grier algorithm to avoid pixel locking. We plot the estimated x location of an emitter with a Gaussian PSF centered on the pixel boundary ($g_{w,\sigma}(x = 1/2)$, as defined by Eq. 6.11) for $\sigma = 1$ (blue dot-dashed line), $\sigma = 2$ (brown dotted line), $\sigma = 3$ (black dashed line), $\sigma = 4$ (red solid line). Values of w yielding results close to $g_{w,\sigma} = 1/2$ are desirable.

In Figure 6.14, we show $g_{w,\sigma}(1/2)$ as a function of w for various σ. For a given σ there is a minimal w that must be used to avoid shifting the tracked positions towards the pixel centers. When the SPIFF-based correction is used, this shift toward the center would be automatically corrected.

6.6.6 Choosing the right region size

Tracking algorithms use local information to estimate the position of each particle. The Crocker-Grier algorithm uses a rectangular area that consists of $(2w+1)\times(2w+1)$ pixels. The choice of the size of this region is important. Not only does the computational effort depend on it, but so does the signal-to-noise. Larger regions have more background photons. Smaller regions contain less information about the PSF. From examination of several examples with Gaussian PSFs and using the SPIFF based Crocker-Grier algorithm, we observe that a size that represents a good compromise between these limiting noise and limiting signal exists

(Figure 6.15). The point where the error is minimal always occurs around the value $w = 2\sigma$.

6.6.7 Further exploration of the effects of noise

We simulate the effects of noise that is representative of experimental measurements. The intensity at each pixel (k, m) is constructed from three terms: (i) the signal $N_S I_{k,m}$ (N_S is the expected number of photons per measurement and $I_{k,m}$ is given by Eq. 6.4); (ii) the average intensity of the background noise, N_B; and (iii) Gaussian noise, G. All three contributions are random: the Gaussian noise is explicitly so, and, generally, $N_S I_{k,m}$ and N_B are averages of random variables with Poisson distributions. The simulations are performed as described in Section 6.4 of the main text, except that when (iii) is present, an additional random variable $G \sim \mathcal{N}(A_G, \sigma_G)$ (normal distribution with mean A_G and variance σ_G) is added at each pixel. The results are compared to an appropriate unbiased Cramér-Rao Lower Bound (CRLB). In all the simulations we used 10^5 different realizations of the signal center position.

From the calculations shown in Figures 6.16 – 6.20 it is clear that application of the SPIFF procedure produces results comparable to, and sometimes better than, the appropriate unbiased CRLB. The best cases are those where the bias in the original Crocker-Grier localization was most pronounced (large σ and small w). For such cases, as explained in the main text, the presence of a large bias decreases the error variance, while the SPIFF correction subsequently removes the bias. We note that the error in Figure 6.16 can be further decreased by increasing the number of realizations. For example, in Figure 6.16c the value for $\sigma_G = 0.1$ is decreased by a factor of $\approx 1/2$ if the number of realizations is multiplied by 10.

When considering adjacent particles, both noise and PSF overlap complicate localization. As immediately above, we explored two cases: (i) the case when only Gaussian noise is present and (ii) the case when the signal fluctuates according to a Poisson distribution in addition to Gaussian noise. The simulations were performed as described in Sections 6.3.2 and 6.4 of

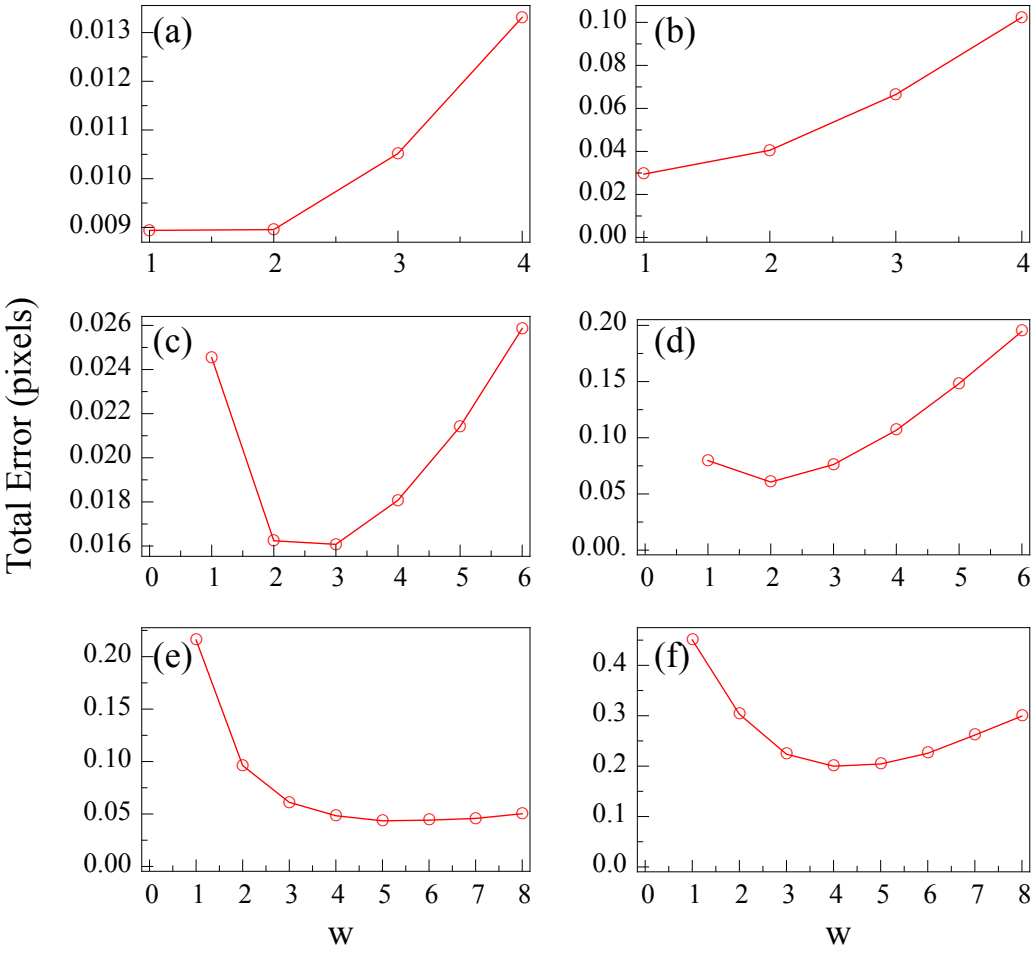

Figure 6.15: Measured error as a function of the choice of w in the Crocker-Grier algorithm. Each row represents a different standard deviation for a Gaussian PSF: $\sigma = 0.5$ pixels (a and b), $\sigma = 1$ pixels (c and d), and $\sigma = 2.5$ pixels (e and f). Each column represents a different number of photons per particle: $N_S = 10^4$ on the left (a, c, and e) and $N_S = 10^3$ on the right (b, d, and f). For all the cases the background noise was taken to be Poissonian with mean of $N_B = 10$ photons per pixel. 10^4 realizations were used to compute each error value.

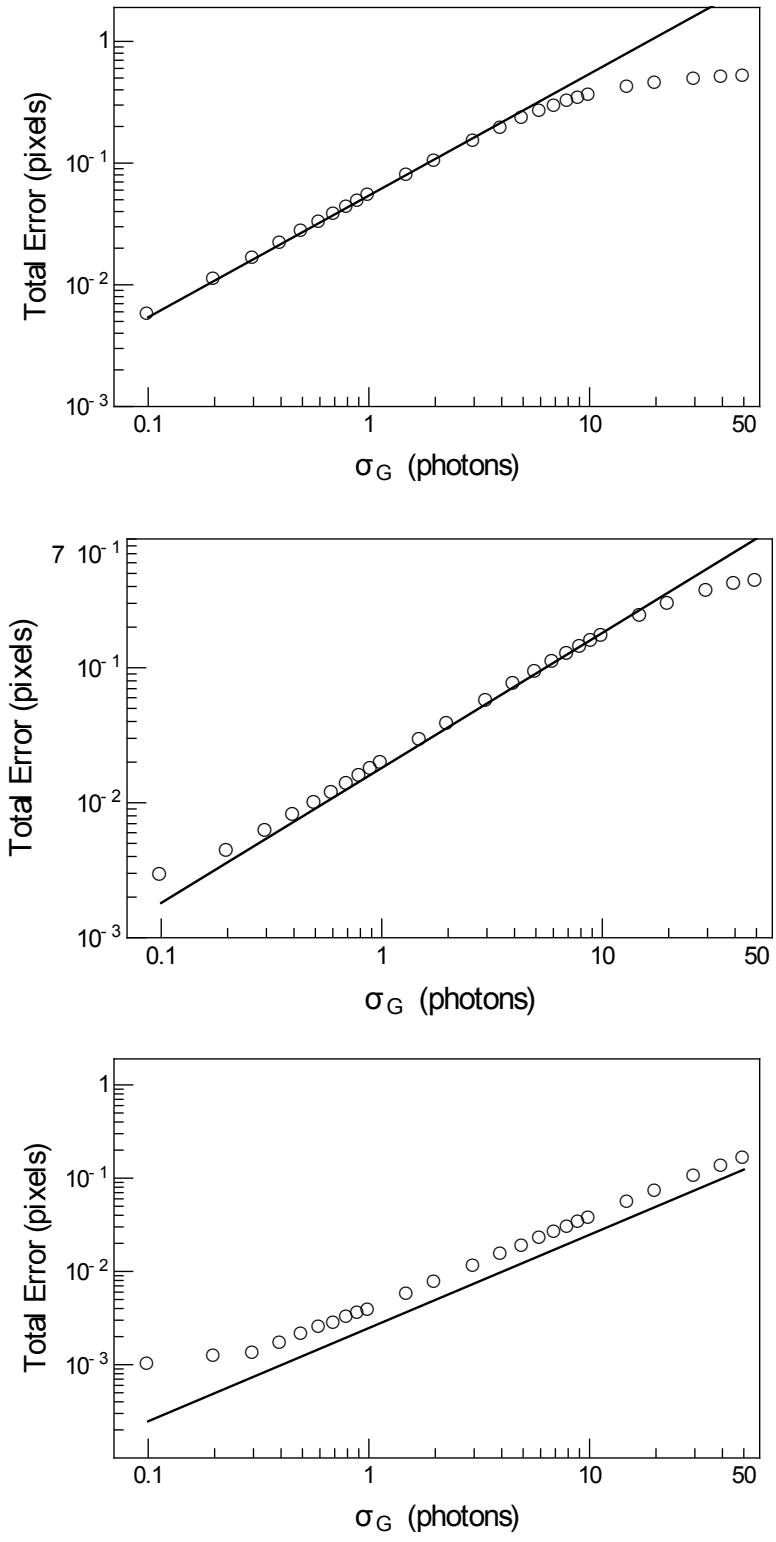

Figure 6.16: Dependence of the error on the extent of Gaussian noise in the absence of Poisson fluctuations. $N_S = 1000$, $N_B = 0$, $A_G = 100$. Simulation results are indicated by symbols and the corresponding unbiased CRLBs are indicated by lines. (a) PSF $\sigma = 2.5$ pixels, $w = 3$ pixels; (b) PSF $\sigma = 1.5$ pixels, $w = 2$ pixels; (c) PSF $\sigma = 0.5$ pixels, $w = 1$ pixel.

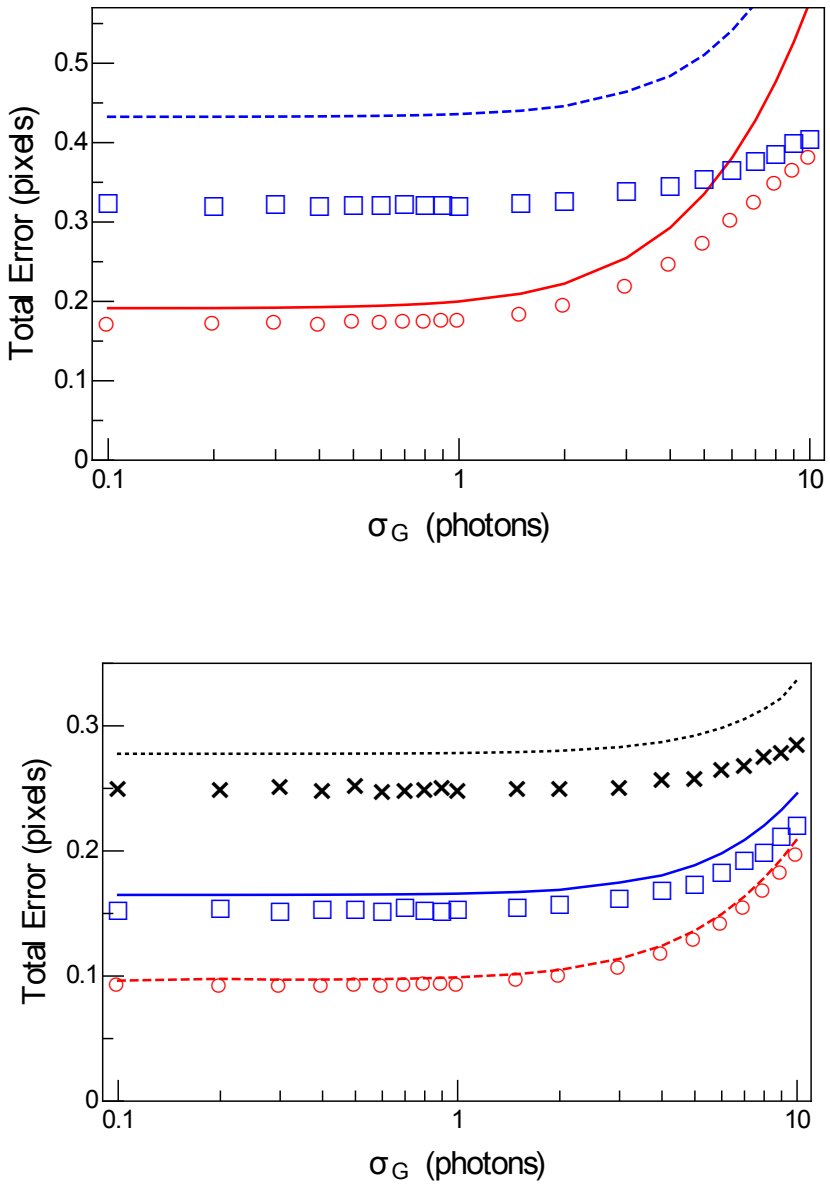

Figure 6.17: Dependence of the error on the extent of Gaussian noise in the presence of Poisson fluctuations. $N_S = 1000$ and $A_G = 100$. Simulation results are indicated by symbols and the corresponding unbiased CRLBs are indicated by lines. (a) PSF $\sigma = 2.5$ pixels; window size $w = 3$ pixels; $N_B = 0$ photons (circles) or $N_B = 50$ photons (squares). (b) PSF $\sigma = 1.5$ pixels; window size $w = 2$ pixels; $N_B = 0$ photons (circles), $N_B = 50$ photons (squares) or $N_B = 200$ photons (crosses).

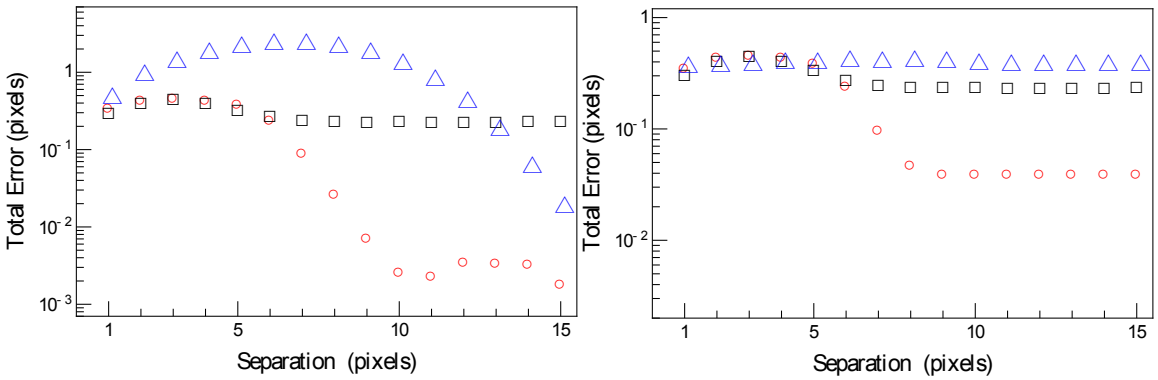

Figure 6.18: Total error as a function of pair separation, with and without SPIFF correction. (left) No noise added and (right) Gaussian noise with $\sigma_G = 1$ photons added. The simulation results were obtained for signal spread of $\sigma = 2$ pixels. The results with the SPIFF correction (circles) are obtained for window size $w = 2$ pixels and compared to results without the SPIFF correction for window size $w = 2$ pixels (squares) and $w = 7$ pixels (triangles).

the main text and the noise was introduced as just described; we calculated the localization error as a function of particle-particle separation, for different noise levels. As expected, the error increases as the noise increases and generally decreases with particle separation. While the SPIFF approach works at large particle separations, below a threshold separation, which depends on the PSF σ, the overlap of two nearby particles signals destroys the localization precision. We have not compared our results, displayed in Figures 6.18–6.20, to a theoretical precision bound due to a lack of existence of such a bound appropriate for two signal sources.

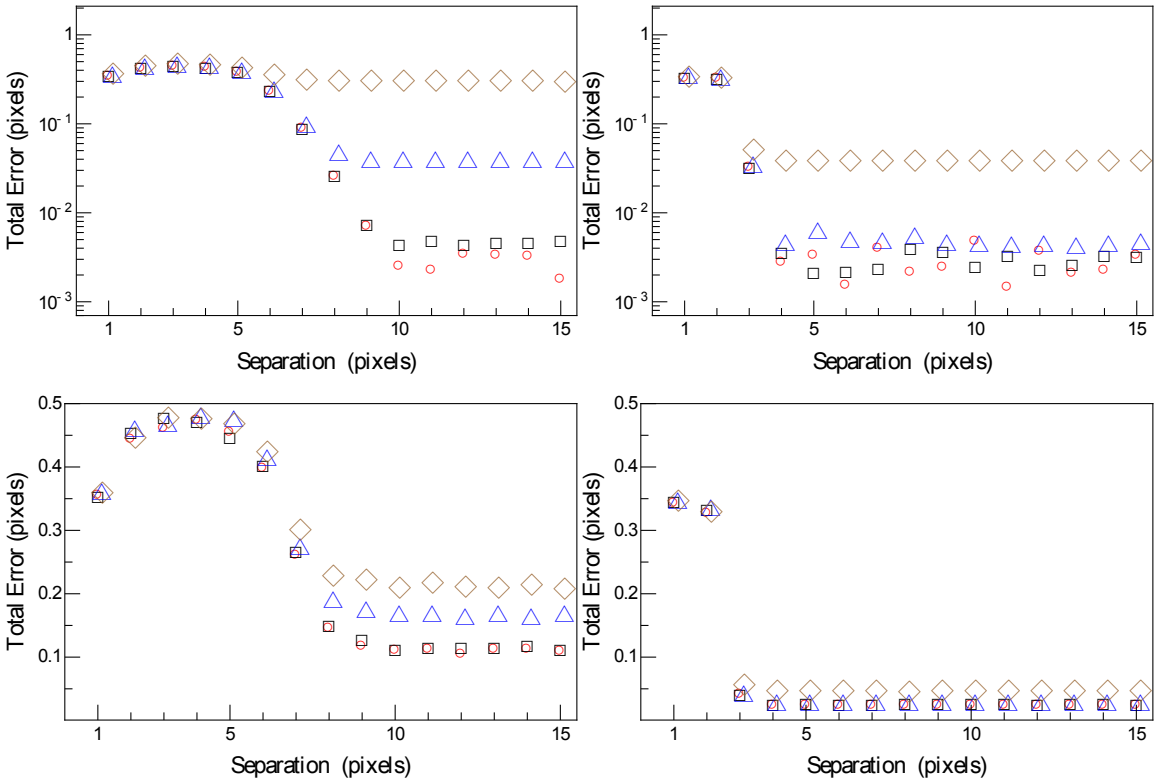

Figure 6.19: Total error as a function of particle-particle separation with varying noise: (circles) no noise, (squares) $\sigma_G = 0.1$ photons, (triangles) $\sigma_G = 1$ photons, and (diamonds) $\sigma_G = 10$ photons. (upper row) Gaussian noise only. (lower row) Gaussian noise and Poisson fluctuations. (left column) The simulation results were obtained for a PSF spread of $\sigma = 2$ pixels (upper) or $\sigma = 3$ pixels (lower), and all the results were obtained with application of the SPIFF correction with window size $w = 2$ pixels. (right column) PSF spread of $\sigma = 0.5$ pixels and window size $w = 1$ pixels.

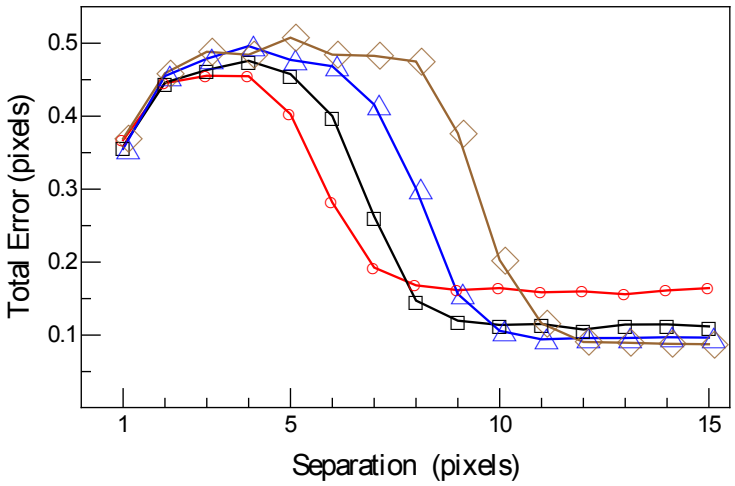

Figure 6.20: Total error as a function of particle-particle separation for several values of the window size w. Only Poisson fluctuations of the signal were included. The simulation results were obtained for PSF $\sigma = 2$ pixels. All the results were obtained with application with SPIFF correction for window size $w = 2$ pixels (circles), $w = 3$ pixels (squares), $w = 4$ pixels (triangles) and $w = 5$ pixels (diamonds). Lines have been added to guide the eye.

REFERENCES

[1] "Chemistry". Dictionary.com Unabridged, 2017. URL `http://www.dictionary.com/browse/chemistry`.

[2] R. White. *Chromatography/Fourier transform infrared spectroscopy and its applications*. Marcel Dekker, New York, NY, 1990.

[3] H. Förster. UV/VIS Spectroscopy. In *Molecular Sieves - Science and Technology*, volume 4, pages 337–426. Springer, Berlin, Heidelberg, 2004. doi: 10.1007/b94239.

[4] R. M. Silverstein, F. X. Webster, and D. Kiemle. Infared Spectroscopy. In *Spectrometric Identification of Organic Compounds*, chapter 2, pages 72–126. John Wiley & Sons, 7th edition, 2005.

[5] R. M. Silverstein, F. X. Webster, and D. Kiemle. Mass Spectrometry. In *Spectrometric Identification of Organic Compounds*, chapter 1, pages 1–71. John Wiley & Sons, 2005.

[6] L. G. Wade. The Origins of Organic Chemistry. In *Organic Chemistry*, pages 1–2. Pearson Prentice Hall, Upper Saddle River, NJ, sixth edition, 2006.

[7] M. S. Silberberg. The Major Classes of Chemical Reactions. In *Chemistry: The Molecular Nature of Mattter and Change*, chapter 4, pages 134–175. McGraw-Hill, New York, NY, fourth edition, 2006.

[8] M. S. Silberberg. Properties of Matter. In *Chemistry: The Molecular Nature of Mattter and Change*, chapter 1, pages 2–3. McGraw-Hill, New York, NY, sixth edition, 2006.

[9] G. Binnig and H. Rohrer. Scanning tunneling microscopy. *IBM Journal of Research and Development*, 30(4):355–369, 1986.

[10] G. Binnig, C. F. Quate, and C. Gerber. Atomic Force Microscope. *Phys. Rev. Lett.*, 56(9):930–933, 1986. doi: 10.1103/PhysRevLett.56.930.

[11] S. Arrhenius. Über die Dissociationswärme und den Einfluss der Temperatur auf den Dissociationsgrad der Elektrolyte. *Zeitschrift für Phys. Chemie*, 4(1):96–116, 1889. doi: 10.1515/zpch-1889-0108.

[12] B. J. Alder and T. E. Wainwright. Studies in Molecular Dynamics. I. General Method. *J. Chem. Phys.*, 31(2):459–466, 1959. doi: 10.1063/1.1730376.

[13] M. Levitt and A. Warshel. Computer simulation of protein folding. *Nature*, 253(5494): 694–698, 1975. doi: 10.1038/253694a0.

[14] A. Warshel and M. Levitt. Theoretical studies of enzymic reactions: Dielectric, electrostatic and steric stabilization of the carbonium ion in the reaction of lysozyme. *J. Mol. Biol.*, 103(2):227–249, 1976. doi: 10.1016/0022-2836(76)90311-9.

[15] B. Uluta, T. Haliloglu, and I. Bozma. Folding pathways explored with artificial potential functions. *Phys. Biol.*, 6(3):036008, 2009. doi: 10.1088/1478-3975/6/3/036008.

[16] L. Sutto, M. D'Abramo, and F. L. Gervasio. Comparing the Efficiency of Biased and Unbiased Molecular Dynamics in Reconstructing the Free Energy Landscape of Met-Enkephalin. *J. Chem. Theory Comput.*, 6(12):3640–3646, 2010. doi: 10.1021/ct100413b.

[17] E. Paci and M. Karplus. Forced unfolding of fibronectin type 3 modules: an analysis by biased molecular dynamics simulations. *J. Mol. Biol.*, 288(3):441–459, 1999. doi: 10.1006/jmbi.1999.2670.

[18] M. M. Burns, J. M. Fournier, and J. A. Golovchenko. Optical matter: crystallization and binding in intense optical fields. *Science*, 249(4970):749–54, 1990. doi: 10.1126/science.249.4970.749.

[19] F. J. García De Abajo. Collective oscillations in optical matter. *Opt. Express*, 15(18):11082, 2007. doi: 10.1364/OE.15.011082.

[20] A. Ashkin. Acceleration and Trapping of Particles by Radiation Pressure. *Phys. Rev. Lett.*, 24(4):156–159, 1970. doi: 10.1103/PhysRevLett.24.156.

[21] D. G. Grier. A revolution in optical manipulation. *Nature*, 424(August):810–816, 2003. doi: 10.1038/nature01935.

[22] A. Einstein. Über die Entwicklung unserer Anschauungen über das Wesen und die Konstitution der Strahlung. *Physikalische Zeitschrift*, 10:817–825, 1909.

[23] A. Einstein. Zur Quantentheorie der Strahlung. *Mitteilungen der Phys. Gesellshaft zu Zürich*, 16:47, 1916.

[24] A. H. Compton. A Quantum Theory of the Scattering of X Rays By Light Elements. *Phys. Rev.*, 21(5):483–502, 1923. doi: 10.1103/PhysRev.21.483.

[25] A. Ashkin, J. M. Dziedzic, J. E. Bjorkholm, and S. Chu. Observation of a single-beam gradient force optical trap for dielectric particles. *Opt. Lett.*, 11(5):288, 1986. doi: 10.1364/OL.11.000288.

[26] K. Svoboda and S. M. Block. Optical trapping of metallic Rayleigh particles. *Opt. Lett.*, 19(13):930, 1994. doi: 10.1364/OL.19.000930.

[27] A. Lehmuskero, P. Johansson, H. Rubinsztein-Dunlop, L. Tong, and M. Käll. Laser Trapping of Colloidal Metal Nanoparticles. *ACS Nano*, 9(4):3453–3469, 2015. doi: 10.1021/acsnano.5b00286.

[28] M. Duocastella and C. Arnold. Bessel and annular beams for materials processing. *Laser Photon. Rev.*, 6(5):607–621, 2012. doi: 10.1002/lpor.201100031.

[29] E. R. Dufresne and D. G. Grier. Optical tweezer arrays and optical substrates created with diffractive optics. *Rev. Sci. Instrum.*, 69(5):1974–1977, 1998. doi: 10.1063/1.1148883.

[30] J. Liesener, M. Reicherter, T. Haist, and H. Tiziani. Multi-functional optical tweezers using computer-generated holograms. *Opt. Commun.*, 185(1-3):77–82, 2000. doi: 10.1016/S0030-4018(00)00990-1.

[31] E. R. Dufresne, G. C. Spalding, M. T. Dearing, S. A. Sheets, and D. G. Grier. Computer-generated holographic optical tweezer arrays. *Rev. Sci. Instrum.*, 72(3):1810, 2001. doi: 10.1063/1.1344176.

[32] J. Arlt, V. Garces-Chavez, W. Sibbett, and K. Dholakia. Optical micromanipulation using a Bessel light beam. *Opt. Commun.*, 197(4-6):239–245, 2001. doi: 10.1016/S0030-4018(01)01479-1.

[33] J. Leach, G. Sinclair, P. Jordan, J. Courtial, M. J. Padgett, J. Cooper, and Z. J. Laczik. 3D manipulation of particles into crystal structures using holographic optical tweezers. *Opt. Express*, 12(1):220, 2004. doi: 10.1364/OPEX.12.000220.

[34] D. G. Grier and Y. Roichman. Holographic optical trapping. *Appl. Opt.*, 45(5):880, 2006. doi: 10.1364/AO.45.000880.

[35] P. L. Biancaniello and J. C. Crocker. Line optical tweezers instrument for measuring nanoscale interactions and kinetics. *Rev. Sci. Instrum.*, 77(11):113702, 2006. doi: 10.1063/1.2387893.

[36] G. R. Fowles. Diffraction. In *Modern Optics*, chapter 5, pages 105–150. Dover, New York, NY, 2nd edition, 1975.

[37] S. Wu and C. Wu. Highspeed liquidcrystal modulators using transient nematic effect. *J. Appl. Phys.*, 65(2):527–532, 1989. doi: 10.1063/1.343135.

[38] M. Reicherter, T. Haist, E. U. Wagemann, and H. J. Tiziani. Optical particle trapping with computer-generated holograms written on a liquid-crystal display. *Opt. Lett.*, 24 (9):608, 1999. doi: 10.1364/OL.24.000608.

[39] Y. Roichman, B. Sun, Y. Roichman, J. Amato-Grill, and D. G. Grier. Optical Forces Arising from Phase Gradients. *Phys. Rev. Lett.*, 100(1):013602, 2008. doi: 10.1103/PhysRevLett.100.013602.

[40] M. M. Burns, J. M. Fournier, and J. A. Golovchenko. Optical binding. *Phys. Rev. Lett.*, 63(12):1233–1236, 1989. doi: 10.1103/PhysRevLett.63.1233.

[41] O. Brzobohatý, T. Čižmár, V. Karásek, M. Šiler, K. Dholakia, and P. Zemánek. Experimental and theoretical determination of optical binding forces. *Opt. Express*, 18 (24):25389–25402, 2010. doi: 10.1364/OE.18.025389.

[42] K. S. Yee. Numerical solution of initial boundary value problems involving maxwell's equations in isotropic media. *IEEE Trans. Antennas Propag.*, 14(3):302–307, 1966. doi: 10.1109/TAP.1966.1138693.

[43] V. Demergis and E. L. Florin. Ultrastrong optical binding of metallic nanoparticles. *Nano Lett.*, 12(11):5756–5760, 2012. doi: 10.1021/nl303035p.

[44] Z. Yan, R. A. Shah, G. Chado, S. K. Gray, M. Pelton, and N. F. Scherer. Guiding spatial arrangements of silver nanoparticles by optical binding interactions in shaped light fields. *ACS Nano*, 7(2):1790–1802, 2013. doi: 10.1021/nn3059407.

[45] Z. Yan, S. K. Gray, and N. F. Scherer. Potential energy surfaces and reaction pathways for light-mediated self-organization of metal nanoparticle clusters. *Nat. Commun.*, 5 (May):3751, 2014. doi: 10.1038/ncomms4751.

[46] E. J. Heilweil and R. M. Hochstrasser. Nonlinear spectroscopy and picosecond transient grating study of colloidal gold. *J. Chem. Phys.*, 82(1985):4762, 1985. doi: 10.1063/1.448693.

[47] M. Maroncelli and G. R. Fleming. Computer simulation of the dynamics of aqueous solvation. *J. Chem. Phys.*, 89(8):5044, 1988. doi: 10.1063/1.455649.

[48] G. R. Fleming and P. G. Wolynes. Chemical dynamics in solution. *Physics Today*, 43 (5):36–43, 1990. doi: 10.1063/1.881234.

[49] B. Sclavi, M. Sullivan, M. R. Chance, M. Brenowitz, and S. A. Woodson. RNA folding at millisecond intervals by synchroton hydroxyl radical footprinting. *Science*, 279(January):1940–1943, 1998.

[50] J. Liphardt, B. Onoa, S. B. Smith, I. Tinoco, and C. Bustamante. Reversible unfolding of single RNA molecules by mechanical force. *Science*, 292(5517):733–7, 2001. doi: 10.1126/science.1058498.

[51] R. A. Nome, J. M. Zhao, W. D. Hoff, and N. F. Scherer. Axis-dependent anisotropy in protein unfolding from integrated nonequilibrium single-molecule experiments, analysis, and simulation. *Proc. Natl. Acad. Sci. USA*, 104(52):20799–804, 2007. doi: 10.1073/pnas.0701281105.

[52] G. J. Smith, K. T. Lee, X. Qu, Z. Xie, J. Pesic, T. R. Sosnick, T. Pan, and N. F. Scherer. A large collapsed-state RNA can exhibit simple exponential single-molecule dynamics. *J. Mol. Biol.*, 378(4):943–53, 2008. doi: 10.1016/j.jmb.2008.01.078.

[53] P.-h. Wang, R. B. Best, and J. Blumberger. Multiscale simulation reveals multiple pathways for H2 and O2 transport in a [NiFe]-hydrogenase. *J. Am. Chem. Soc.*, 133 (10):3548–3556, 2011. doi: 10.1021/ja109712q.

[54] Y. Zhang and O. K. Dudko. Statistical mechanics of viral entry. *Phys. Rev. Lett.*, 114 (1):1–5, 2015. doi: 10.1103/PhysRevLett.114.018104.

[55] E. V. Anslyn and D. A. Dougherty. Transition State Theory and Related Topics. In *Modern Physical Organic Chemistry*, pages 365–373. University Science Books, Sausalito, CA, 2006.

[56] H. Eyring. The Activated Complex in Chemical Reactions. *J. Chem. Phys.*, 3(2): 107–115, 1935. doi: 10.1063/1.1749604.

[57] M. G. Evans and M. Polanyi. Some applications of the transition state method to the calculation of reaction velocities, especially in solution. *T. Faraday Soc.*, 31:875, 1935. doi: 10.1039/tf9353100875.

[58] K. J. Laidler and M. C. King. Development of transition-state theory. *J. Phys. Chem.*, 87(15):2657–2664, 1983. doi: 10.1021/j100238a002.

[59] H. Kramers. Brownian motion in a field of force and the diffusion model of chemical reactions. *Physica*, 7(4):284–304, 1940. doi: 10.1016/S0031-8914(40)90098-2.

[60] R. Zwanzig. *Nonequilibrium statistical mechanics*. Oxford University Press, 2001.

[61] G. Hummer and A. Szabo. Kinetics from Nonequilibrium Single-Molecule Pulling Experiments. *Biophys. J.*, 85(1):5–15, 2003. doi: 10.1016/S0006-3495(03)74449-X.

[62] O. K. Dudko, G. Hummer, and A. Szabo. Intrinsic rates and activation free energies from single-molecule pulling experiments. *Phys. Rev. Lett.*, 96(10):1–4, 2006. doi: 10.1103/PhysRevLett.96.108101.

[63] C. M. Pitsillides, E. K. Joe, X. Wei, R. R. Anderson, and C. P. Lin. Selective Cell Targeting with Light-Absorbing Microparticles and Nanoparticles. *Biophys. J.*, 84(6): 4023–4032, 2003. doi: 10.1016/S0006-3495(03)75128-5.

[64] X. Nan, P. A. Sims, P. Chen, and X. Sunney Xie. Observation of individual microtubule motor steps in living cells with endocytosed quantum dots. *J. Phys. Chem. B*, 109(51): 24220–24224, 2005. doi: 10.1021/jp056360w.

[65] B. Cui, B. Lin, and S. A. Rice. Dynamical heterogeneity in a dense quasi-two-dimensional colloidal liquid. *J. Chem. Phys.*, 114(20):9142, 2001. doi: 10.1063/1.1369129.

[66] B. Cui. *Structure and diffusion in dense confined colloidal suspensions*. PhD thesis, University of Chicago, 2002.

[67] Y. Sokolov, D. Frydel, D. G. Grier, H. Diamant, and Y. Roichman. Hydrodynamic pair attractions between driven colloidal particles. *Phys. Rev. Lett.*, 107(15):158302, 2011. doi: 10.1103/PhysRevLett.107.158302.

[68] J. Pesic, J. Z. Terdik, X. Xu, Y. Tian, A. Lopez, S. A. Rice, A. R. Dinner, and N. F. Scherer. Structural responses of quasi-two-dimensional colloidal fluids to excitations elicited by nonequilibrium perturbations. *Phys. Rev. E*, 86(3):031403, 2012. doi: 10.1103/PhysRevE.86.031403.

[69] P. Vallotton and S. Olivier. Tri-track: Free Software for Large-Scale Particle Tracking. *Microsc. Microanal.*, 19(02):451–460, 2013. doi: 10.1017/S1431927612014328.

[70] C. A. Schneider, W. S. Rasband, and K. W. Eliceiri. NIH Image to ImageJ: 25 years of image analysis. *Nat. Methods*, 9(7):671–675, 2012. doi: 10.1038/nmeth.2089.

[71] J. Crocker and D. Grier. Methods of digital video microscopy for colloidal studies. *J. Colloid Interface Sci.*, 310(179):298–310, 1996.

[72] I. F. Sbalzarini and P. Koumoutsakos. Feature point tracking and trajectory analysis for video imaging in cell biology. *J. Struct. Biol.*, 151(2):182–195, 2005. doi: 10.1016/j.jsb.2005.06.002.

[73] R. Parthasarathy. Rapid, accurate particle tracking by calculation of radial symmetry centers. *Nat. Methods*, 9(7):724–6, 2012. doi: 10.1038/nmeth.2071.

[74] M. K. Cheezum, W. F. Walker, and W. H. Guilford. Quantitative Comparison of Algorithms for Tracking Single Fluorescent Particles. *Biophys. J.*, 81(4):2378–2388, 2001. doi: 10.1016/S0006-3495(01)75884-5.

[75] Y. Feng, J. Goree, and B. Liu. Accurate particle position measurement from images. *Rev. Sci. Instrum.*, 78(5), 2007. doi: 10.1063/1.2735920.

[76] H. Nobach and M. Honkanen. Two-dimensional Gaussian regression for sub-pixel displacement estimation in particle image velocimetry or particle position estimation in particle tracking velocimetry. *Exp. Fluids*, 38(4):511–515, 2005. doi: 10.1007/s00348-005-0942-3.

[77] M. J. Guffey. *Optical Trapping and Direct Optical Patterning of Plasmonic Nanoparticle Assemblies*. PhD thesis, University of Chicago, 2010.

[78] J.-H. Lee, K. Kamada, N. Enomoto, and J. Hojo. Polyhedral Gold Nanoplate: High Fraction Synthesis of Two-Dimensional Nanoparticles through Rapid Heating Process. *Cryst. Growth Des.*, 8(8):2638–2645, 2008. doi: 10.1021/cg0702075.

[79] H. Liu and Q. Yang. A two-step temperature-raising process to gold nanoplates with optical and surface enhanced Raman spectrum properties. *CrystEngComm*, 13(7):2281, 2011. doi: 10.1039/c0ce00432d.

[80] T. A. Major, M. S. Devadas, S. S. Lo, and G. V. Hartland. Optical and Dynamical Properties of Chemically Synthesized Gold Nanoplates. *J. Phys. Chem. C*, 117(3):1447–1452, 2013. doi: 10.1021/jp311470t.

[81] D. Allan, T. Caswell, N. Keim, and C. Van Der Wel. Trackpy v0.3.2, 2016. doi: 10.5281/ZENODO.60550.

[82] Hamamatsu. Phase spatial light modulator LCOS-SLM. URL `https://www.hamamatsu.com/resources/pdf/ssd/e12_handbook_lcos_slm.pdf`.

[83] A. Jesacher. *Applications of spatial light modulators for optical trapping and image processing*. PhD thesis, Leopold-Franzens University, 2007.

[84] A. A. Michelson and E. W. Morley. On the relative motion of the Earth and the luminiferous ether. *Am. J. Sci.*, s3-34(203):333–345, 1887. doi: 10.2475/ajs.s3-34.203.333.

[85] P. Hariharan, B. F. Oreb, and T. Eiju. Digital phase-shifting interferometry: a simple error-compensating phase calculation algorithm. *Appl. Opt.*, 26(13):2504, 1987. doi: 10.1364/AO.26.002504.

[86] F. von Zernike. Beugungstheorie des schneidenver-fahrens und seiner verbesserten form, der phasenkontrastmethode. *Physica*, 1(7-12):689–704, 1934. doi: 10.1016/S0031-8914(34)80259-5.

[87] R. J. Noll. Zernike polynomials and atmospheric turbulence. *J. Opt. Soc. Am.*, 66(3):207, 1976. doi: 10.1364/JOSA.66.000207.

[88] Y. Roichman and D. G. Grier. Projecting extended optical traps with shape-phase holography. *Opt. Lett.*, 31(11):1675, 2006. doi: 10.1364/OL.31.001675.

[89] Y. Roichman and D. G. Grier. Three-dimensional holographic ring traps. In D. L. Andrews, E. J. Galvez, and G. Nienhuis, editors, *Proc. SPIE*, volume 6483, page 64830F, 2007. doi: 10.1117/12.701034.

[90] J. E. Curtis and D. G. Grier. Structure of Optical Vortices. *Phys. Rev. Lett.*, 90(13):133901, 2003. doi: 10.1103/PhysRevLett.90.133901.

[91] Y. Roichman, D. G. Grier, and G. Zaslavsky. Anomalous collective dynamics in optically driven colloidal rings. *Phys. Rev. E*, 75(2):020401, 2007. doi: 10.1103/PhysRevE.75.020401.

[92] R. W. Gerchberg and W. O. Saxton. A practical algorithm for the determination of phase from image and diffraction plane pictures. *Optik*, 35:237–246, 1972.

[93] P. Figliozzi, N. Sule, Z. Yan, Y. Bao, S. Burov, S. K. Gray, S. A. Rice, S. Vaikuntanathan, and N. F. Scherer. Driven optical matter: Dynamics of electrodynamically coupled nanoparticles in an optical ring vortex. *Phys. Rev. E*, 95(2):022604, 2017. doi: 10.1103/PhysRevE.95.022604.

[94] M. Reichert and H. Stark. Circling particles and drafting in optical vortices. *J. Phys. Condens. Matter*, 16(38):S4085–S4094, 2004. doi: 10.1088/0953-8984/16/38/023.

[95] S. Okubo, S. Shibata, Y. S. Kawamura, M. Ichikawa, and Y. Kimura. Dynamic clustering of driven colloidal particles on a circular path. *Phys. Rev. E*, 92(3):032303, 2015. doi: 10.1103/PhysRevE.92.032303.

[96] E. Lauga and T. R. Powers. The hydrodynamics of swimming microorganisms. *Rep. Prog. Phys.*, 72(9):96601, 2009. doi: 10.1088/0034-4885/72/9/096601.

[97] T. Vicsek and A. Zafeiris. Collective motion. *Phys. Rep.*, 517(3-4):71–140, 2012. doi: 10.1016/j.physrep.2012.03.004.

[98] M. C. Marchetti, J. F. Joanny, S. Ramaswamy, T. B. Liverpool, J. Prost, M. Rao, and R. A. Simha. Hydrodynamics of soft active matter. *Rev. Mod. Phys.*, 85(3):1143–1189, 2013. doi: 10.1103/RevModPhys.85.1143.

[99] J. Palacci, S. Sacanna, A. P. Steinberg, D. J. Pine, and P. M. Chaikin. Living crystals of light-activated colloidal surfers. *Science*, 339(6122):936–40, 2013. doi: 10.1126/science.1230020.

[100] Z. Yan, M. Sajjan, and N. F. Scherer. Fabrication of a Material Assembly of Silver Nanoparticles Using the Phase Gradients of Optical Tweezers. *Phys. Rev. Lett.*, 114 (14):143901, 2015. doi: 10.1103/PhysRevLett.114.143901.

[101] O. M. Marago, P. H. Jones, P. G. Gucciardi, G. Volpe, and A. C. Ferrari. Optical trapping and manipulation of nanostructures. *Nat. Nanotech.*, 8(11):807–819, 2013. doi: 10.1038/nnano.2013.208.

[102] R. A. Beth. Mechanical Detection and Measurement of the Angular Momentum of Light. *Phys. Rev.*, 50(2):115–125, 1936.

[103] L. Allen, M. W. Beijersbergen, R. J. C. Spreeuw, and J. P. Woerdman. Orbital Angular Momentum of Light and the Transformation of Laguerre-Gaussian Laser Modes. *Phys. Rev. A*, 45(11):8185–8189, 1992.

[104] M. Dienerowitz, M. Mazilu, P. J. Reece, T. F. Krauss, and K. Dholakia. Optical Vortex Trap for Resonant Confinement of Metal Nanoparticles. *Opt. Express*, 16(7): 4991–4999, 2008. doi: 10.1364/oe.16.004991.

[105] L. Tong, V. D. Miljkovic, and M. Käll. Alignment, Rotation, and Spinning of Single Plasmonic Nanoparticles and Nanowires Using Polarization Dependent Optical Forces. *Nano Lett.*, 10(1):268–273, 2010. doi: 10.1021/nl9034434.

[106] Z. Yan and N. F. Scherer. Optical Vortex Induced Rotation of Silver Nanowires. *J. Phys. Chem. Lett.*, 4(17):2937–2942, 2013. doi: 10.1021/jz401381e.

[107] M. Nieto-Vesperinas. Optical theorem for the conservation of electromagnetic helicity: Significance for molecular energy transfer and enantiomeric discrimination by circular dichroism. *Phys. Rev. A*, 92(2):023813, 2015. doi: 10.1103/PhysRevA.92.023813.

[108] H. He, M. E. J. Friese, N. R. Heckenberg, and H. Rubinsztein-Dunlop. Direct Observation of Transfer of Angular Momentum to Absorptive Particles from a Laser Beam with a Phase Singularity. *Phys. Rev. Lett.*, 75(5):826–829, 1995.

[109] K. T. Gahagan and G. A. Swartzlander. Optical vortex trapping of particles. *Opt. Lett.*, 21(11):827–829, 1996. doi: 10.1364/ol.21.000827.

[110] M. E. J. Friese, J. Enger, H. Rubinsztein-Dunlop, and N. R. Heckenberg. Optical Angular-Momentum Transfer to Trapped Absorbing Particles. *Phys. Rev. A*, 54(2): 1593–1596, 1996.

[111] N. B. Simpson, K. Dholakia, L. Allen, and M. J. Padgett. Mechanical equivalence of spin and orbital angular momentum of light: an optical spanner. *Opt. Lett.*, 22(1): 52–54, 1997. doi: 10.1364/ol.22.000052.

[112] L. Paterson, M. P. MacDonald, J. Arlt, W. Sibbett, P. E. Bryant, and K. Dholakia. Controlled Rotation of Optically Trapped Microscopic Particles. *Science*, 292(5518): 912–914, 2001. doi: 10.1126/science.1058591.

[113] K. Ladavac and D. G. Grier. Microoptomechanical pumps assembled and driven by holographic optical vortex arrays. *Opt. Express*, 12(6):1144, 2004. doi: 10.1364/OPEX.12.001144.

[114] K. Ladavac and D. G. Grier. Colloidal hydrodynamic coupling in concentric optical vortices. *Europhys. Lett.*, 70(4):548–554, 2005. doi: 10.1209/epl/i2005-10022-6.

[115] S. H. Tao, X.-C. C. Yuan, J. Lin, and Y. Y. Sun. Influence of geometric shape of optically trapped particles on the optical rotation induced by vortex beams. *J. Appl. Phys.*, 100(4):043105, 2006. doi: 10.1063/1.2260823.

[116] R. Di Leonardo, S. Keen, J. Leach, C. D. Saunter, G. D. Love, G. Ruocco, and M. J. Padgett. Eigenmodes of a hydrodynamically coupled micron-size multiple-particle ring. *Phys. Rev. E*, 76(6):061402, 2007. doi: 10.1103/PhysRevE.76.061402.

[117] S. H. Simpson and S. Hanna. Optical Angular Momentum Transfer by Laguerre-Gaussian Beams. *J. Opt. Soc. Am. A*, 26(3):625–638, 2009.

[118] J. Ng, Z. Lin, and C. T. Chan. Theory of Optical Trapping by an Optical Vortex Beam. *Phys. Rev. Lett.*, 104(10):103601, 2010.

[119] A. Lehmuskero, Y. Li, P. Johansson, and M. Käll. Plasmonic particles set into fast orbital motion by an optical vortex beam. *Opt. Express*, 22(4):4349–56, 2014. doi: 10.1364/OE.22.004349.

[120] M. Li, S. Yan, B. Yao, Y. Liang, and P. Zhang. Spinning and orbiting motion of particles in vortex beams with circular or radial polarizations. *Opt. Express*, 24(18): 20604, 2016. doi: 10.1364/OE.24.020604.

[121] J. Kotar, M. Leoni, B. Bassetti, M. C. Lagomarsino, and P. Cicuta. Hydrodynamic synchronization of colloidal oscillators. *Proc. Natl. Acad. Sci. USA*, 107(17):7669–7673, 2010. doi: 10.1073/pnas.0912455107.

[122] Y. Sassa, S. Shibata, Y. Iwashita, and Y. Kimura. Hydrodynamically induced rhythmic motion of optically driven colloidal particles on a ring. *Phys. Rev. E*, 85(6):061402, 2012. doi: 10.1103/PhysRevE.85.061402.

[123] H. Nagar and Y. Roichman. Collective excitations of hydrodynamically coupled driven colloidal particles. *Phys. Rev. E*, 90(4):042302, 2014.

[124] A. S. Ostrovsky, C. Rickenstorff-Parrao, and V. Arrizón. Generation of the perfect optical vortex using a liquid-crystal spatial light modulator. *Opt. Lett.*, 38(4):534, 2013. doi: 10.1364/OL.38.000534.

[125] M. Chen, M. Mazilu, Y. Arita, E. M. Wright, and K. Dholakia. Dynamics of microparticles trapped in a perfect vortex beam. *Opt. Lett.*, 38(22):4919–4922, 2013. doi: 10.1364/ol.38.004919.

[126] P. C. Chaumet and M. Nieto-Vesperinas. Optical binding of particles with or without the presence of a flat dielectric surface. *Phys. Rev. B*, 64(3):035422, 2001. doi: 10.1103/PhysRevB.64.035422.

[127] S. A. Tatarkova, A. E. Carruthers, and K. Dholakia. One-dimensional optically bound arrays of microscopic particles. *Phys. Rev. Lett.*, 89(28 Pt 1):283901, 2002. doi: 10.1103/PhysRevLett.89.283901.

[128] S. Mohanty, J. Andrews, and P. Gupta. Optical binding between dielectric particles. *Opt. Express*, 12(12):2746–2753, 2004. doi: 10.1364/OPEX.12.002746.

[129] D. S. Bradshaw and D. L. Andrews. Optically induced forces and torques: Interactions between nanoparticles in a laser beam. *Phys. Rev. A*, 72(3):033816, 2005. doi: 10.1103/PhysRevA.72.033816.

[130] K. Dholakia and P. Zemánek. Colloquium: Gripped by light: Optical binding. *Rev. Mod. Phys.*, 82(2):1767–1791, 2010. doi: 10.1103/RevModPhys.82.1767.

[131] Z. Yan, Y. Bao, U. Manna, R. A. Shah, and N. F. Scherer. Enhancing nanoparticle electrodynamics with gold nanoplate mirrors. *Nano Lett.*, 14(5):2436–2442, 2014. doi: 10.1021/nl500107w.

[132] N. Sule, S. A. Rice, S. K. Gray, and N. F. Scherer. An electrodynamics-Langevin dynamics (ED-LD) approach to simulate metal nanoparticle interactions and motion. *Opt. Express*, 23(23):29978–29992, 2015. doi: 10.1364/OE.23.029978.

[133] D. B. Ruffner and D. G. Grier. Comment on "Scattering Forces from the Curl of the Spin Angular Momentum of a Light Field". *Phys. Rev. Lett.*, 111(5):059301, 2013.

[134] W. Mu, Z. Liu, L. Luan, G. Wang, G. C. Spalding, and J. B. Ketterson. Enhanced particle transport in an oscillating sinusoidal optical potential. *New J. Phys.*, 11(10):103017, 2009. doi: 10.1088/1367-2630/11/10/103017.

[135] M. Bandyopadhyay, S. Dattagupta, and M. Sanyal. Diffusion enhancement in a periodic potential under high-frequency space-dependent forcing. *Phys. Rev. E*, 73(5):051108, 2006. doi: 10.1103/PhysRevE.73.051108.

[136] T. Li. Physical Principle of Optical Tweezers. In *Fundamental Tests of Physics with Optically Trapped Microspheres*, pages 9–21. Springer New York, New York, NY, 2013. doi: 10.1007/978-1-4614-6031-2.

[137] M. A. Bevan and D. C. Prieve. Hindered diffusion of colloidal particles very near to a wall: Revisited. *J. Chem. Phys.*, 113(3):1228–1236, 2000. doi: 10.1063/1.481900.

[138] P. Reimann, R. Bartussek, R. Häußler, and P. Hänggi. Brownian motors driven by temperature oscillations. *Phys. Lett. A*, 215(1-2):26–31, 1996. doi: 10.1016/0375-9601(96)00222-8.

[139] P. Reimann, C. Van den Broeck, H. Linke, P. Hänggi, J. M. Rubi, and A. Pérez-Madrid. Diffusion in tilted periodic potentials: Enhancement, universality, and scaling. *Phys. Rev. E*, 65(3):031104, 2002. doi: 10.1103/PhysRevE.65.031104.

[140] S. H. Lee and D. G. Grier. Giant colloidal diffusivity on corrugated optical vortices. *Phys. Rev. Lett.*, 96(19):190601, 2006. doi: 10.1103/PhysRevLett.96.190601.

[141] M. Evstigneev, O. Zvyagolskaya, S. Bleil, R. Eichhorn, C. Bechinger, and P. Reimann. Diffusion of colloidal particles in a tilted periodic potential: Theory versus experiment. *Phys. Rev. E*, 77(4):041107, 2008. doi: 10.1103/PhysRevE.77.041107.

[142] S. Albaladejo, M. I. Marqués, F. Scheffold, and J. J. Sáenz. Giant Enhanced Diffusion of Gold Nanoparticles in Optical Vortex Fields. *Nano Lett.*, 9(10):3527–3531, 2009.

[143] M. Khoury, A. M. Lacasta, J. M. Sancho, and K. Lindenberg. Weak disorder: Anomalous transport and diffusion are normal yet again. *Phys. Rev. Lett.*, 106(9):090602, 2011. doi: 10.1103/PhysRevLett.106.090602.

[144] P. Reimann, C. Van den Broeck, H. Linke, P. Hänggi, J. M. Rubi, and A. Pérez-Madrid. Giant acceleration of free diffusion by use of tilted periodic potentials. *Phys. Rev. Lett.*, 87(9):010602, 2001. doi: 10.1103/PhysRevLett.87.010602.

[145] W. Sun, S. Pan, and Y. Jiang. Computation of the optical trapping force on small particles illuminated with a focused light beam using a FDTD method. *J. Mod. Opt.*, 53(18):2691–2700, 2006.

[146] S.-C. Kong, J. J. Simpson, and V. Backman. ADE-FDTD Scattered-Field Formulation for Dispersive Materials. *IEEE Microw. Wirel. Co.*, 18(1):4–6, 2008. doi: 10.1109/LMWC.2007.911970.

[147] H.-J. Butt, K. Graf, and M. Kappl. Surface Forces. In *Physics and Chemistry of Interfaces*, pages 80–117. Wiley-VCH, Weinheim, FRG, second edition, 2006. doi: 10.1002/3527602313.ch6.

[148] H. Hamaker. The London-Van der Waals attraction between spherical particles. *Physica*, 4(10):1058–1072, 1937. doi: 10.1016/S0031-8914(37)80203-7.

[149] E. Lifshitz and M. Hamermesh. The theory of molecular attractive forces between solids. In *Perspectives in Theoretical Physics*, pages 329–349. Pergamon, 1992. doi: 10.1016/B978-0-08-036364-6.50031-4.

[150] I. Dzyaloshinskii, E. Lifshitz, and L. Pitaevskii. The general theory of Van der Waals forces. *Adv. Phys.*, 10(38):165–209, 1961. doi: 10.1080/00018736100101281.

[151] J. N. Israelachvili. Van der Waals Forces between Particles and Surfaces. In *Intermolecular and Surface Forces*, pages 253–289. Elsevier, Waltham, MA, third edition, 2011. doi: 10.1016/B978-0-12-391927-4.10013-1.

[152] S. G. Flicker, J. L. Tipa, and S. G. Bike. Quantifying Double-Layer Repulsion between a Colloidal Sphere and a Glass Plate Using Total Internal Reflection Microscopy. *J. Colloid Interface Sci.*, 158(2):317–325, 1993. doi: 10.1006/jcis.1993.1262.

[153] A. Sze, D. Erickson, L. Ren, and D. Li. Zeta-potential measurement using the Smoluchowski equation and the slope of the current-time relationship in electroosmotic flow. *J. Colloid Interface Sci.*, 261(2):402–410, 2003. doi: 10.1016/S0021-9797(03)00142-5.

[154] A. D. McNaught and A. Wilkinson. *ζ-potential*. IUPAC, Research Triangle Park, NC, second edition, 1997. doi: 10.1351/goldbook.Z06735.

[155] G. Gouesbet, B. Maheu, and G. Gréhan. Light scattering from a sphere arbitrarily located in a Gaussian beam, using a Bromwich formulation. *J. Opt. Soc. Am. A*, 5(9): 1427, 1988. doi: 10.1364/JOSAA.5.001427.

[156] G. M. Hale and M. R. Querry. Optical constants of water in the 200nm to 200mm wavelength region. *Appl. Opt.*, 12(3):555–563, 1973. doi: 10.1364/AO.12.000555.

[157] P. B. Johnson and R. W. Christry. Optical Constants of the Noble Metals. *Phys. Rev. B*, 6(12):4370–4379, 1972. doi: 10.1103/PhysRevB.6.4370.

[158] H. S. Chung, K. McHale, J. M. Louis, and W. A. Eaton. Single-Molecule Fluorescence Experiments Determine Protein Folding Transition Path Times. *Science*, 335(6071): 981–984, 2012. doi: 10.1126/science.1215768.

[159] G. I. Bell. Models for the Specific Adhesion of Cells to Cells. 618(1978), 2007. doi: 10.1126/science.347575.

[160] E. Evans and K. Ritchie. Dynamic strength of molecular adhesion bonds. *Biophys. J.*, 72(4):1541–1555, 1997. doi: 10.1016/S0006-3495(97)78802-7.

[161] O. K. Dudko, J. Mathé, A. Szabo, A. Meller, and G. Hummer. Extracting Kinetics from Single-Molecule Force Spectroscopy: Nanopore Unzipping of DNA Hairpins. *Biophys. J.*, 92(12):4188–4195, 2007. doi: 10.1529/biophysj.106.102855.

[162] S. Garcia-Manyes, L. Dougan, C. L. Badilla, J. Brujic, and J. M. Fernandez. Direct observation of an ensemble of stable collapsed states in the mechanical folding of ubiquitin. *Proc. Natl. Acad. Sci. USA*, 106(26):10534–10539, 2009. doi: 10.1073/pnas.0901213106.

[163] C. Pangali, M. Rao, and B. J. Berne. A Monte Carlo simulation of the hydrophobic interaction. *J. Chem. Phys.*, 71(7):2975, 1979. doi: 10.1063/1.438701.

[164] E. H. Thiede, B. Van Koten, J. Weare, and A. R. Dinner. Eigenvector method for umbrella sampling enables error analysis. *J. Chem. Phys.*, 145(8):084115, 2016. doi: 10.1063/1.4960649.

[165] J. T. Bullerjahn, S. Sturm, and K. Kroy. Theory of rapid force spectroscopy. *Nat. Commun.*, 5:4463, 2014. doi: 10.1038/ncomms5463.

[166] A. Szabo, K. Schulten, and Z. Schulten. First passage time approach to diffusion controlled reactions. *J. Chem. Phys.*, 72(1980):4350–7, 1980. doi: 10.1063/1.439715.

[167] R. Belousov, E. G. D. Cohen, and L. Rondoni. The Langevin equation for systems with a preferred spatial direction. *Phys. Rev. E*, 94(1):032127, 2016. doi: 10.1103/PhysRevE.94.032127.

[168] G. Hummer and A. Szabo. Free energy reconstruction from nonequilibrium single-molecule pulling experiments. *Proc. Natl. Acad. Sci. USA*, 98(7):3658–3661, 2001. doi: 10.1073/pnas.071034098.

[169] G. Hummer and A. Szabo. Free energy surfaces from single-molecule force spectroscopy. *Acc. Chem. Res.*, 38(7):504, 2005. doi: 10.1021/ar040148d.

[170] C. Jarzynski. Nonequilibrium Equality for Free Energy Differences. *Phys. Rev. Lett.*, 78(14):2690–2693, 1997. doi: 10.1103/PhysRevLett.78.2690.

[171] D. M. Golden. The Reaction Cl + NO 2 ClONO and ClNO 2 . *J. Phys. Chem. A*, 111(29):6772–6780, 2007. doi: 10.1021/jp069000x.

[172] S. Kawai and T. Komatsuzaki. Dynamic pathways to mediate reactions buried in thermal fluctuations. I. Time-dependent normal form theory for multidimensional Langevin equation. *J. Chem. Phys.*, 131(22), 2009. doi: 10.1063/1.3268621.

[173] Z. Hu, L. Cheng, and B. J. Berne. First passage time distribution in stochastic processes with moving and static absorbing boundaries with application to biological rupture experiments. *J. Chem. Phys.*, 133(3), 2010. doi: 10.1063/1.3456556.

[174] G. T. Craven, T. Bartsch, and R. Hernandez. Communication: Transition state trajectory stability determines barrier crossing rates in chemical reactions induced by time-dependent oscillating fields. *J. Chem. Phys.*, 141(4):041106, 2014. doi: 10.1063/1.4891471.

[175] C. van der Wel and D. J. Kraft. Automated tracking of colloidal clusters with sub-pixel accuracy and precision. *J. Phys. Condens. Matter*, 29(4):044001, 2017. doi: 10.1088/1361-648X/29/4/044001.

[176] S. Burov, P. Figliozzi, B. Lin, S. A. Rice, N. F. Scherer, and A. R. Dinner. Single-pixel interior filling function approach for detecting and correcting errors in particle tracking. *Proc. Natl. Acad. Sci. USA*, (20):201619104, 2016. doi: 10.1073/pnas.1619104114.

[177] E. Pollak and P. Pechukas. Transition states, trapped trajectories, and classical bound states embedded in the continuum. *J. Chem. Phys.*, 69(3):1218, 1978. doi: 10.1063/1.436658.

[178] M. Born and E. Wolf. *Principles of Optics: Electromagnetic Theory of Propagation, Interference and Diffraction of Light*. Cambridge Univ Press, Cambridge, UK, 1999.

[179] L. Novonty and B. Hecht. *Principles of Nano-Optics*. Cambridge Univ Press, Cambridge, UK, 2006.

[180] R. E. Thompson, D. R. Larson, and W. W. Webb. Precise nanometer localization analysis for individual fluorescent probes. *Biophys. J.*, 82(5):2775–2783, 2002.

[181] C. C. Liebe. Accuracy performance of star trackers - A tutorial. *IEEE Trans. Aerosp. Electron. Syst.*, 38(2):587–599, 2002. doi: 10.1109/TAES.2002.1008988.

[182] A. Yildiz. Myosin V Walks Hand-Over-Hand: Single Fluorophore Imaging with 1.5-nm Localization. *Science*, 300(5628):2061–2065, 2003. doi: 10.1126/science.1084398.

[183] X. H. Qu, D. Wu, L. Mets, and N. F. Scherer. Nanometer-localized multiple single-molecule fluorescence microscopy. *Proc. Natl. Acad. Sci. USA*, 101(31):11298–11303, 2004. doi: 10.1073/pnas.0402155101.

[184] E. Betzig, G. H. Patterson, R. Sougrat, O. W. Lindwasser, S. Olenych, J. S. Bonifacino, M. W. Davidson, J. Lippincott-Schwartz, and H. F. Hess. Imaging intracellular fluorescent proteins at nanometer resolution. *Science*, 313(5793):1642–1645, 2006. doi: 10.1126/science.1127344.

[185] M. J. Rust, M. Bates, and X. Zhuang. Sub-diffraction-limit imaging by stochastic optical reconstruction microscopy (STORM). *Nat. Methods*, 3(10):793–795, 2006. doi: 10.1038/nmeth929.

[186] D. T. Burnette, P. Sengupta, Y. Dai, J. Lippincott-Schwartz, and B. Kachar. Bleaching/blinking assisted localization microscopy for superresolution imaging using standard fluorescent molecules. *Proc. Natl. Acad. Sci. USA*, 108(52):21081–21086, 2011. doi: 10.1073/pnas.1117430109.

[187] S. Stallinga and B. Rieger. Accuracy of the Gaussian Point Spread Function model in 2D localization microscopy. *Opt. Express*, 18(24):24461–24476, 2010. doi: 10.1364/OE.18.024461.

[188] K. I. Mortensen, L. S. Churchman, J. A. Spudich, and H. Flyvbjerg. Optimized localization analysis for single-molecule tracking and super-resolution microscopy. *Nat. Methods*, 7(5):377–U59, 2010. doi: 10.1038/NMETH.1447.

[189] A. J. Berglund, M. D. McMahon, J. J. McClelland, and J. A. Liddle. Fast, bias-free algorithm for tracking single particles with variable size and shape. *Opt. Express*, 16 (18):14064–14075, 2008. doi: 10.1364/OE.16.014064.

[190] S. B. Andersson. Localization of a fluorescent source without numerical fitting. *Opt. Express*, 16(23):18714–18724, 2008. doi: 10.1364/OE.16.018714.

[191] M. T. J. van Loenhout, J. W. J. Kerssemakers, I. De Vlaminck, and C. Dekker. Non-Bias-Limited Tracking of Spherical Particles, Enabling Nanometer Resolution at Low Magnification. *Biophys. J.*, 102(10):2362–2371, 2012. doi: 10.1016/j.bpj.2012.03.073.

[192] B. F. Alexander. Elimination of systematic error in subpixel accuracy centroid estimation. *Opt. Eng.*, 30(9):1320, 1991. doi: 10.1117/12.55947.

[193] C. W. Harland, M. J. Bradley, and R. Parthasarathy. Phospholipid bilayers are viscoelastic. *Proc. Natl. Acad. Sci. USA*, 107(45):19146–19150, 2010. doi: 10.1073/pnas.1010700107.

[194] N. Chenouard, I. Smal, F. de Chaumont, M. Maška, I. F. Sbalzarini, Y. Gong, J. Cardinale, C. Carthel, S. Coraluppi, M. Winter, A. R. Cohen, W. J. Godinez, K. Rohr, Y. Kalaidzidis, L. Liang, J. Duncan, H. Shen, Y. Xu, K. E. G. Magnusson, J. Jaldén, H. M. Blau, P. Paul-Gilloteaux, P. Roudot, C. Kervrann, F. Waharte, J.-Y. Tinevez, S. L. Shorte, J. Willemse, K. Celler, G. P. van Wezel, H.-W. Dan, Y.-S. Tsai, C. O. de Solórzano, J.-C. Olivo-Marin, and E. Meijering. Objective comparison of particle tracking methods. *Nat. Methods*, 11(3):281–289, 2014. doi: 10.1038/nmeth.2808.

[195] M. J. Saxton. Single-particle tracking: connecting the dots. *Nat. Methods*, 5(8):671–672, 2008. doi: 10.1038/nmeth0808-671.

[196] Y. Gao and M. L. Kilfoil. Accurate detection and complete tracking of large populations of features in three dimensions. *Opt. Express*, 17(6):4685–4704, 2009. doi: 10.1364/OE.17.004685.

[197] J. C. Crocker and E. R. Weeks. Explanation of tracking macros, 2016. URL `http://www.physics.emory.edu/faculty/weeks//idl/tracking.html`.

[198] J. C. Crocker and B. D. Hoffman. Multiple-Particle Tracking and Two-Point Microrheology in Cells. *Methods Cell Biol.*, 83:141–178, 2007. doi: 10.1016/S0091-679X(07)83007-X.

[199] B. Cui, H. Diamant, B. Lin, and S. A. Rice. Anomalous hydrodynamic interaction in a Quasi-two-dimensional suspension. *Phys. Rev. Lett.*, 92(25 I):258301–1, 2004. doi: 10.1103/PhysRevLett.92.258301.

[200] C. Shannon. Communication in the Presence of Noise. *Proc. IRE*, 37(1):10–21, 1949. doi: 10.1109/JRPROC.1949.232969.

[201] S. Burov, S. M. A. Tabei, T. Huynh, M. P. Murrell, L. H. Philipson, S. A. Rice, M. L. Gardel, N. F. Scherer, and A. R. Dinner. Distribution of directional change as a signature of complex dynamics. *Proc. Natl. Acad. Sci. USA*, 110(49):19689–19694, 2013. doi: 10.1073/pnas.1319473110.

[202] S. Kay. *Fundamentals of Statistical Signal Processing: Estimation Theory*. Prentice Hall, Englewood Cliffs, NJ, vol 1 edition, 1993.

[203] M. Wernet and A. Pline. Particle displacement tracking technique and Cramer-Rao lower bound error in centroid estimates from CCD imagery. *Exp. Fluids*, 15-15(4-5): 295–307, 1993. doi: 10.1007/BF00223407.

[204] R. J. Ober, S. Ram, and E. S. Ward. Localization accuracy in single-molecule microscopy. *Biophys. J.*, 86(2):1185–1200, 2004.

[205] C. S. Smith, N. Joseph, B. Rieger, and K. A. Lidke. Fast, single-molecule localization that achieves theoretically minimum uncertainty. *Nat. Methods*, 7(5):373–375, 2010. doi: 10.1038/nmeth.1449.

[206] A. R. Small and R. Parthasarathy. Superresolution Localization Methods. In T. Johnson, MA and Martinez, editor, *Annu. Rev. Phys. Chem.*, volume 65 of *Annual Review of Physical Chemistry*, pages 107–125. 2014. doi: 10.1146/annurev-physchem-040513-103735.

[207] A. Small and S. Stahlheber. Fluorophore localization algorithms for super-resolution microscopy. *Nat. Methods*, 11(3):267–279, 2014. doi: 10.1038/NMETH.2844.

[208] A. V. Weigel, B. Simon, M. M. Tamkun, and D. Krapf. Ergodic and nonergodic processes coexist in the plasma membrane as observed by single-molecule tracking. *Proc. Natl. Acad. Sci. USA*, 108(16):6438–6443, 2011. doi: 10.1073/pnas.1016325108.

[209] S. M. A. Tabei, S. Burov, H. Y. Kim, A. Kuznetsov, T. Huynh, J. Jureller, L. H. Philipson, A. R. Dinner, and N. F. Scherer. Intracellular transport of insulin granules is a subordinated random walk. *Proc. Natl. Acad. Sci. USA*, 110(13):4911–4916, 2013. doi: 10.1073/pnas.1221962110.

[210] T. A. Caswell, Z. Zhang, M. L. Gardel, and S. R. Nagel. Observation and characterization of the vestige of the jamming transition in a thermal three-dimensional system. *Phys. Rev. E*, 87(1), 2013. doi: 10.1103/PhysRevE.87.012303.

[211] M. Gai, D. Carollo, M. Delbò, M. G. Lattanzi, G. Massone, F. Bertinetto, G. Mana, and S. Cesare. Location accuracy limitations for CCD cameras. *Astron. Astrophys.*, 367(1):362–370, 2001. doi: 10.1051/0004-6361:20000339.

APPENDIX A

PROPERTIES OF AG NANOPARTICLES

A.1 Zeta Potential and Size measurements of 150 nm Ag Nanoparticles

Ag nanoparticle zeta potentials and sizes were characterized with a Zetasizer (Malvern, Nano-ZS, Zen3600) in December 2014. Several stock solutions of nanoparticles (all from NanoComposix) were characterized using solutions with the same product numbers but received at different times. Also, for nanoparticles that were citrate capped, a comparison was made between dilution in 18 MΩ water and a 2 mM citrate buffer. Table A.1 names and outlines the different measurements performed.

Table A.1: Ag nanoparticles characterized with zetasizer measurements.

Name	Dilution	Product Number	Date Received
Old Citrate	150x with 18 MΩ H_2O	KJW1606	05/29/13
New Citrate	150x with 18 MΩ H_2O	KJW1606	11/25/14
PVP	150x with 18 MΩ H_2O	KJW1882	10/25/14
Old Citrate Buffered	150x with 2 mM Citrate Buffer	KJW1606	05/29/13
New Citrate Buffered	150x with 2 mM Citrate Buffer	KJW1606	11/25/14

A.1.1 Size Measurements of Ag Nanoparticles

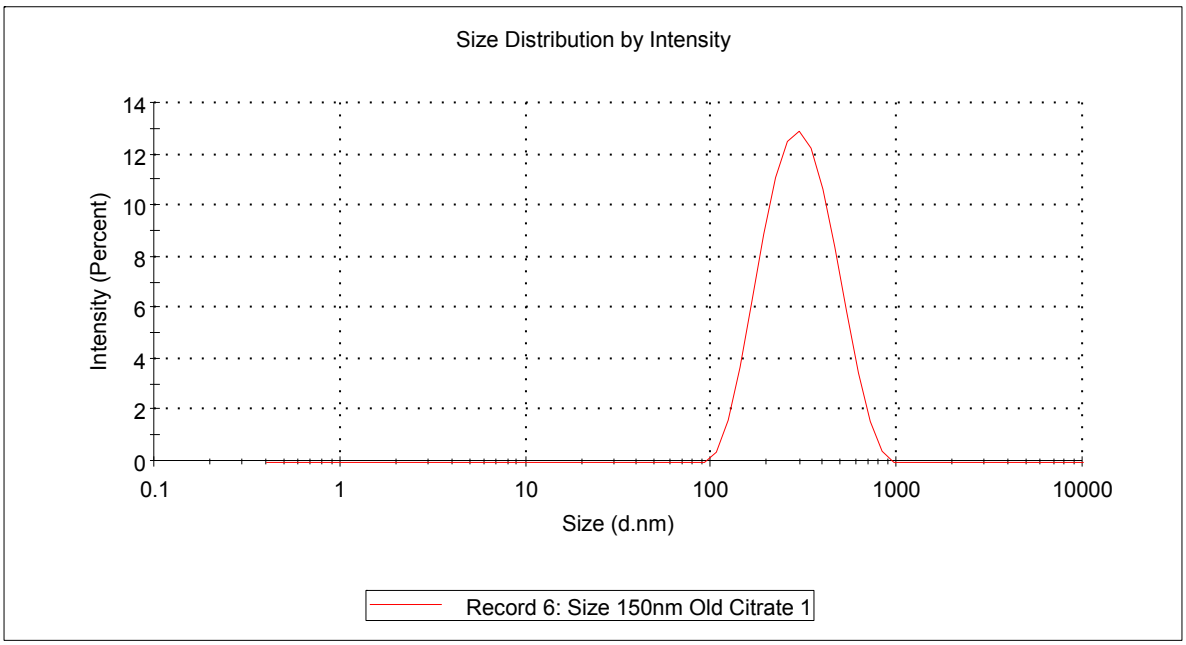

Figure A.1: Size distribution of Old Citrate 150 nm Ag nanoparticles diluted 150x in 18 MΩ water. Peak is at 319 nm.

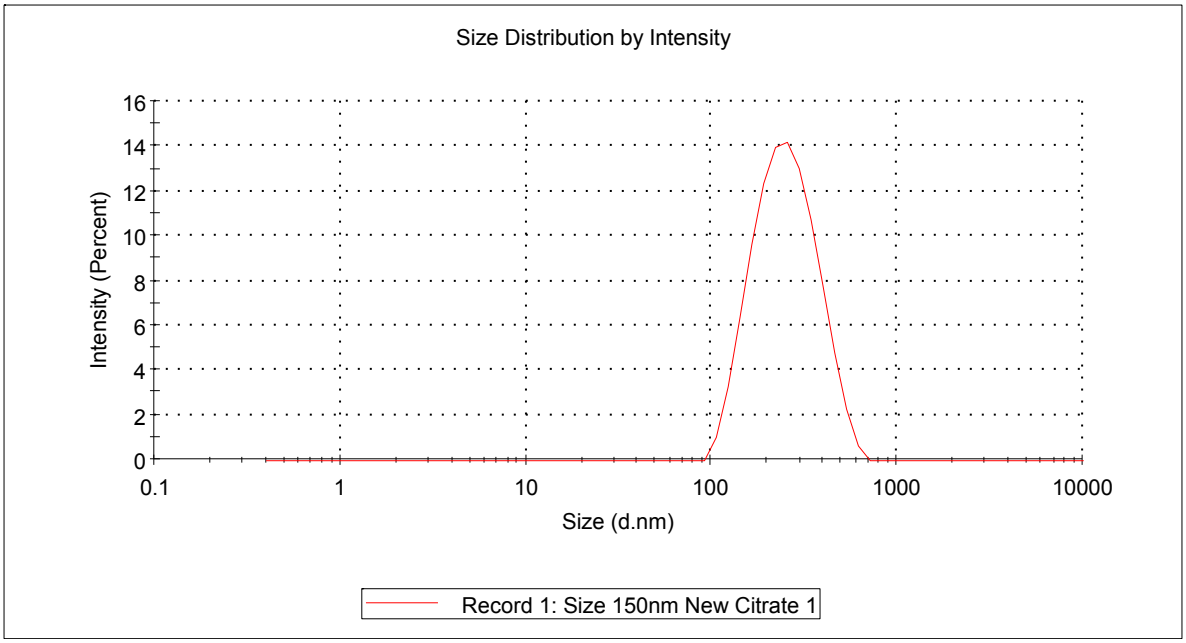

Figure A.2: Size distribution of New Citrate 150 nm Ag nanoparticles diluted 150x in 18 MΩ water. Peak is at 264 nm.

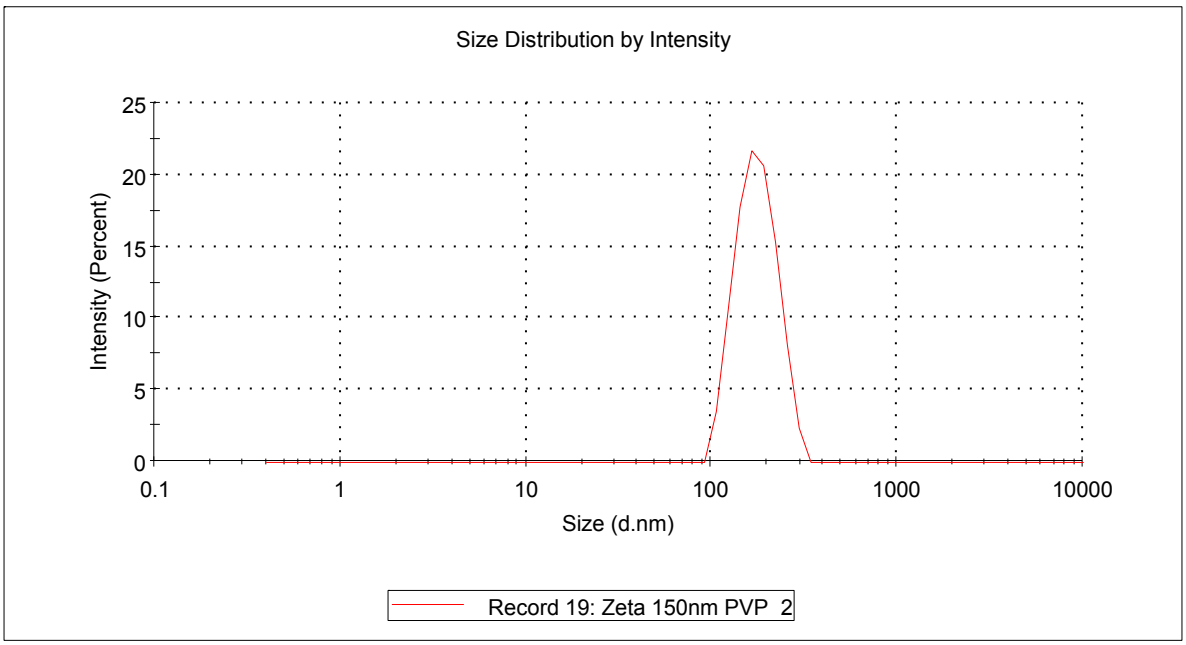

Figure A.3: Size distribution of PVP 150 nm Ag nanoparticles diluted 150x in 18 MΩ water. Peak is at 178 nm.

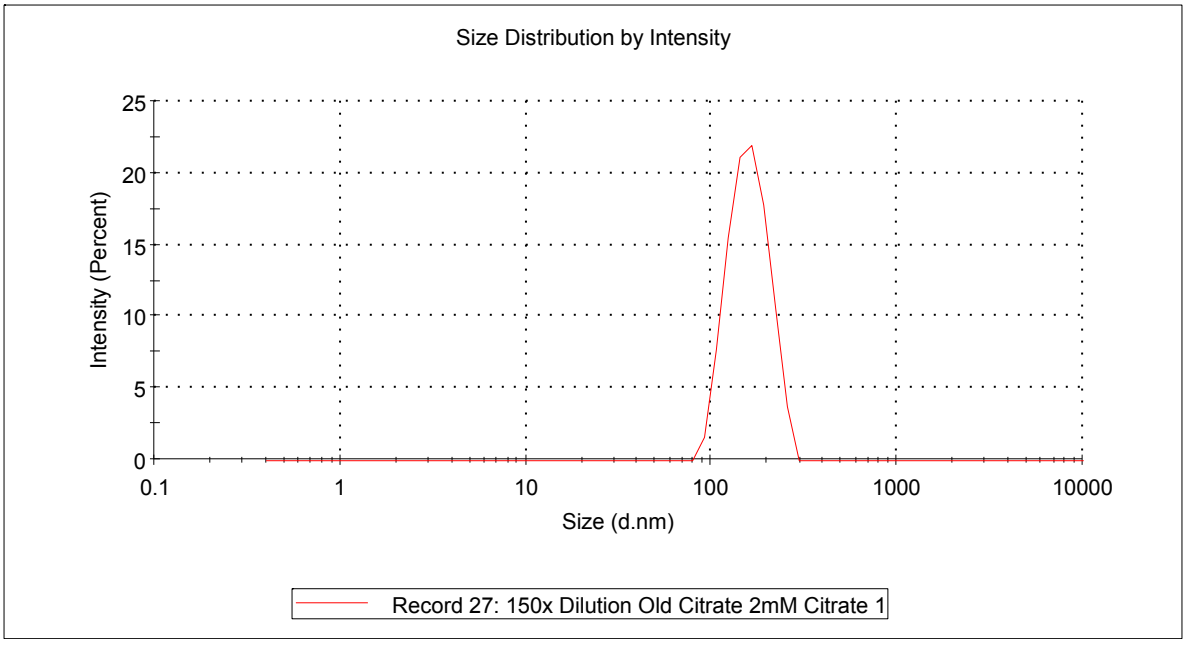

Figure A.4: Size distribution of Old Citrate Buffered 150 nm Ag nanoparticles diluted 150x in 2 mM citrate buffer solution. Peak is at 161 nm.

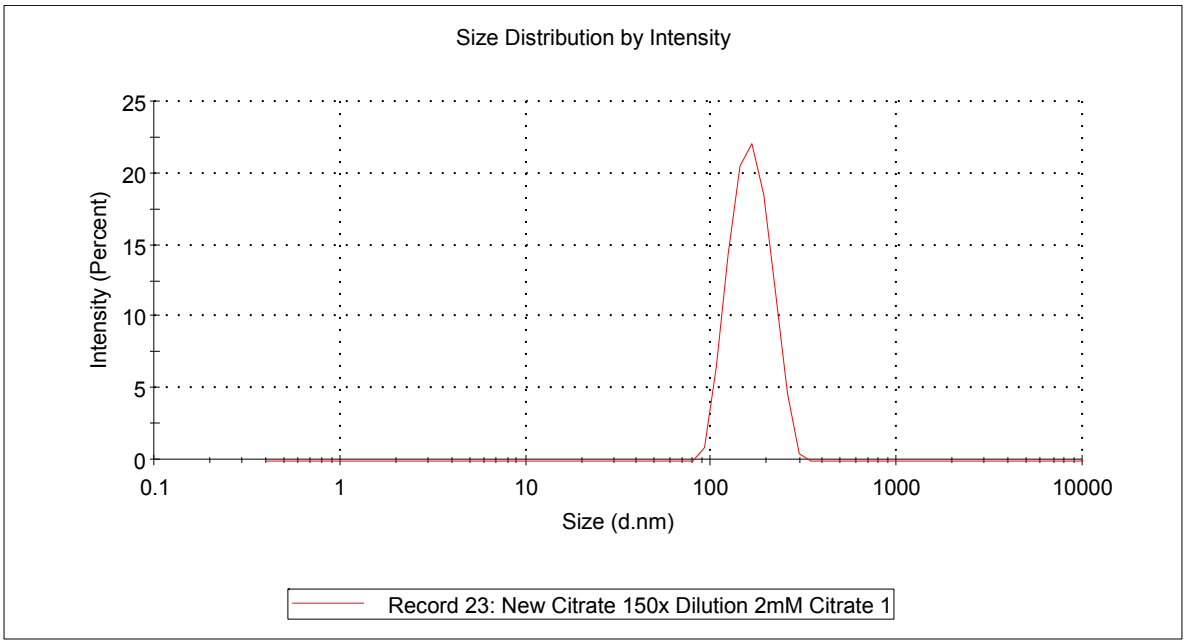

Figure A.5: Size distribution of New Citrate Buffered 150 nm Ag nanoparticles diluted 150x in 2 mM citrate buffer solution. Peak is at 165 nm.

A.1.2 Zeta Potential Measurements of Ag Nanoparticles

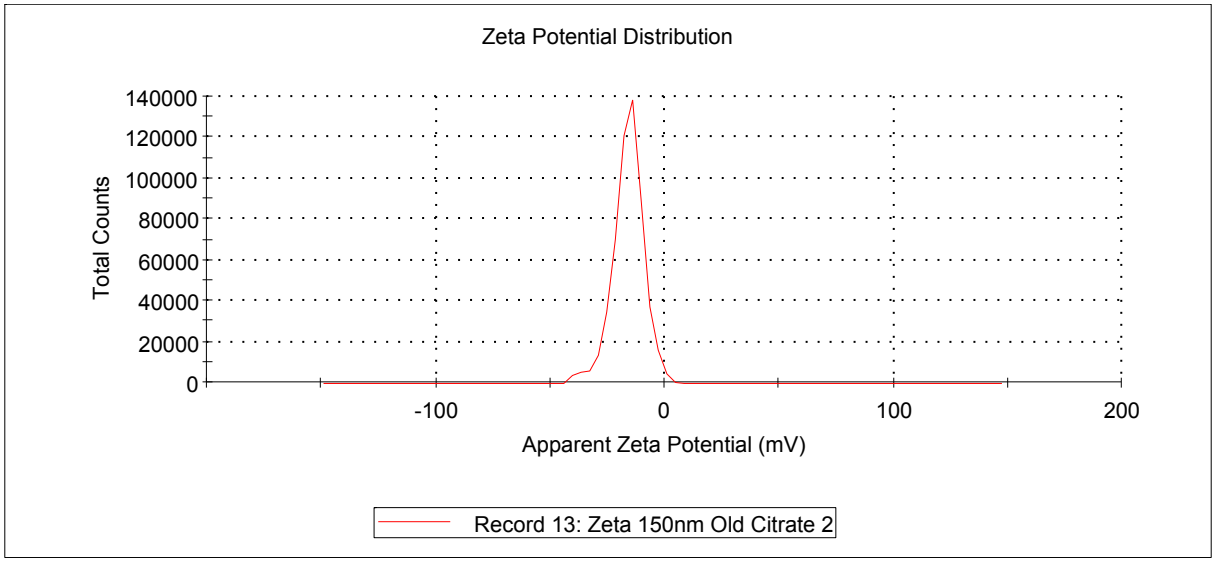

Figure A.6: Zeta potential of Old Citrate 150 nm Ag nanoparticles diluted 150x in 18 MΩ water. Peak is at −16 mV.

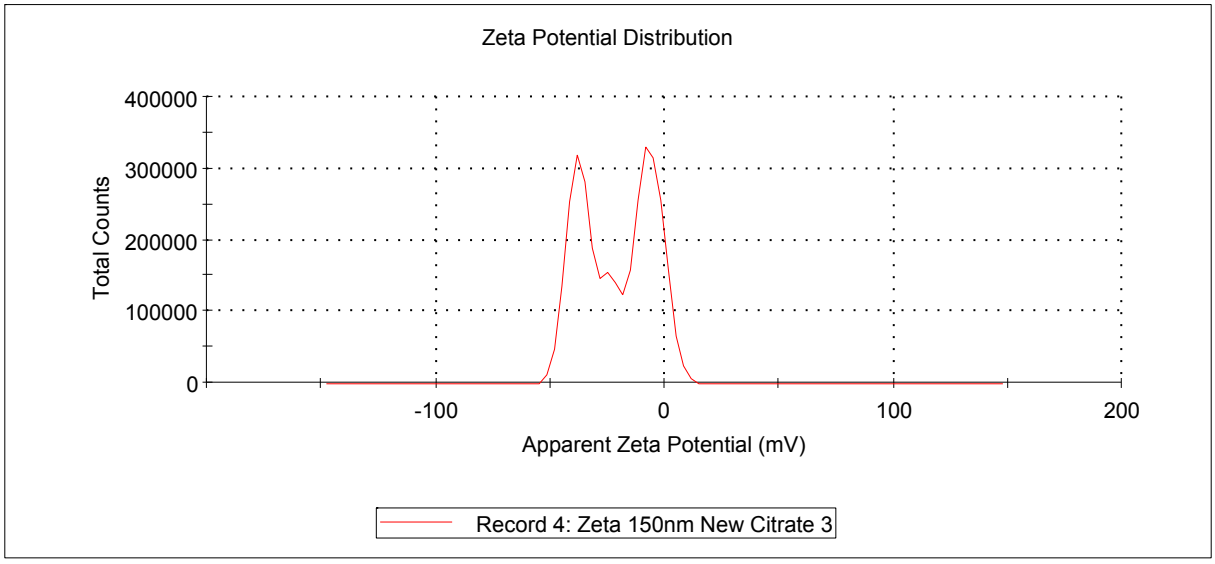

Figure A.7: Zeta potential of New Citrate 150 nm Ag nanoparticles diluted 150x in 18 MΩ water. Peaks are at −37 mV and −6.9 mV.

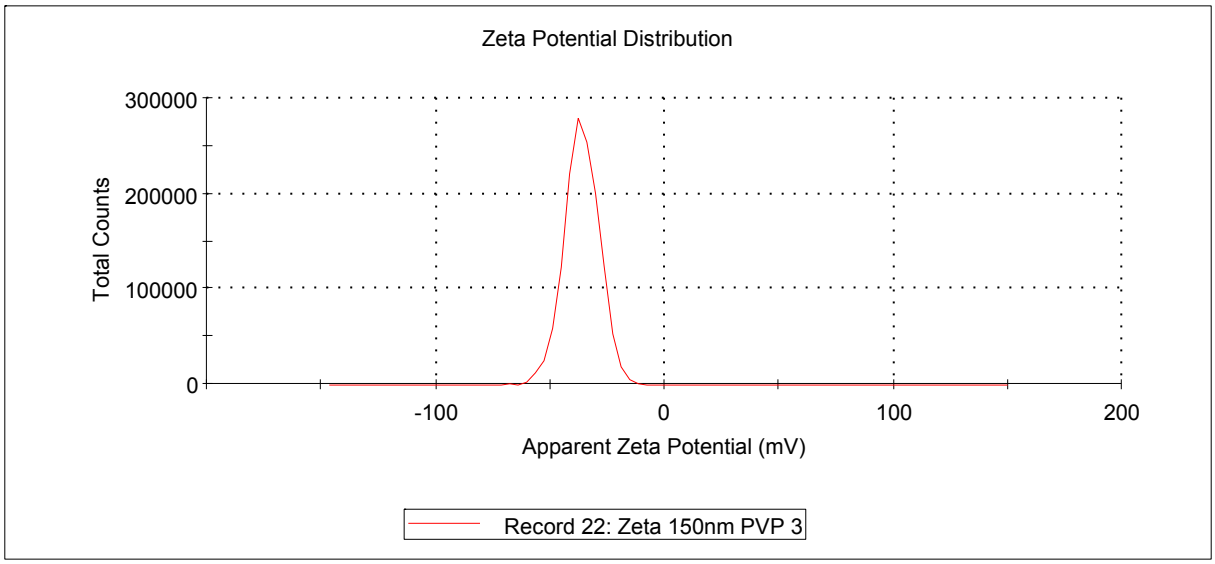

Figure A.8: Size distribution of PVP 150 nm Ag nanoparticles diluted 150x in 18 MΩ water. Peak is at −36 mV.

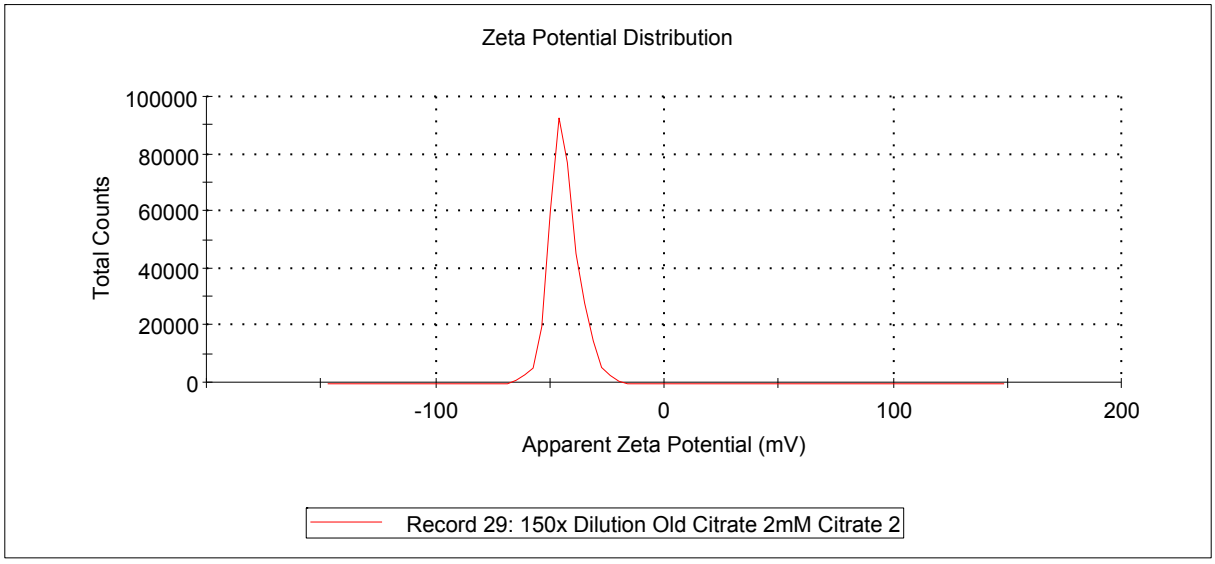

Figure A.9: Zeta potential of Old Citrate Buffered 150 nm Ag nanoparticles diluted 150x in 2 mM citrate buffer solution. Peak is at −44 mV.

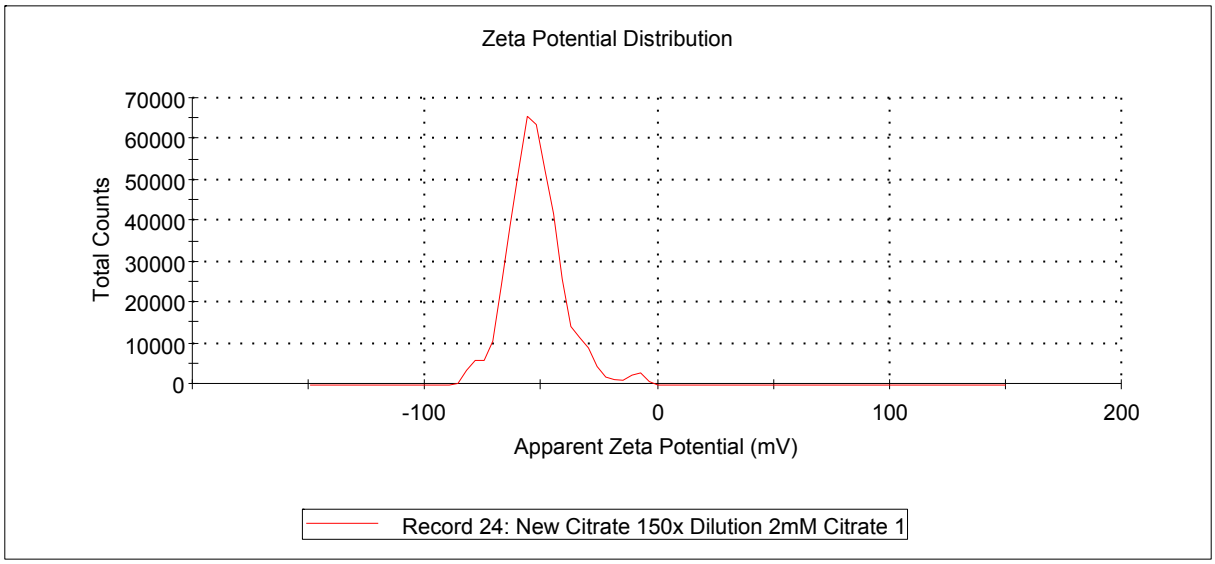

Figure A.10: Zeta potential of New Citrate Buffered 150 nm Ag nanoparticles diluted 150x in 2 mM citrate buffer solution. Peak is at −53 mV.

A.2 TEM Images of 150 nm Ag Nanoparticles

The citrate capped Ag nanoparticles (NanoComposix, NanoXact KJW1606) received on 05/29/13 were imaged using transmission electron microscopy (TEM). This section has sample images of the particles at different scales.

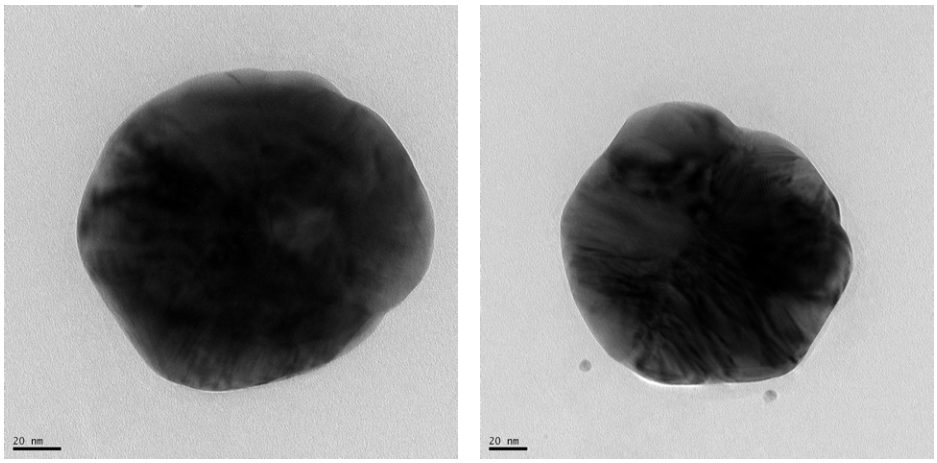

Figure A.11: TEM images of individual 150 nm Ag nanoparticles. Scale bar in bottom left is 20 nm.

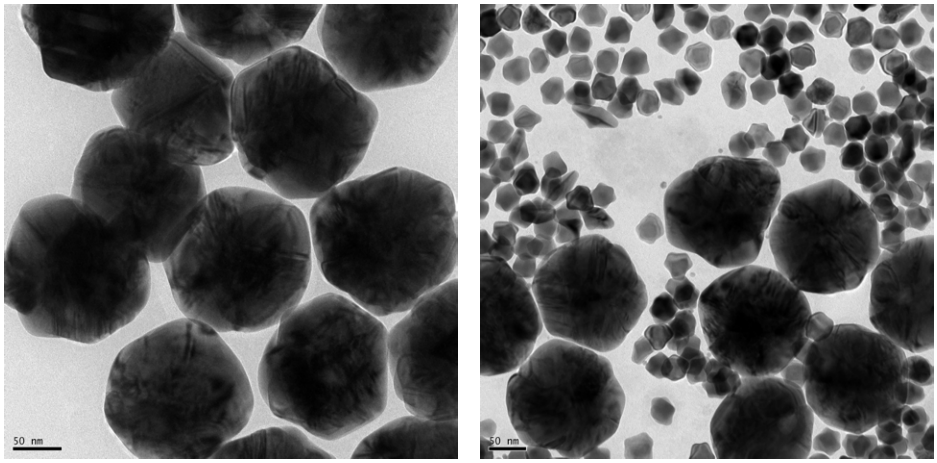

Figure A.12: TEM images of 150 nm Ag nanoparticles. Scale bar in bottom left is 50 nm.

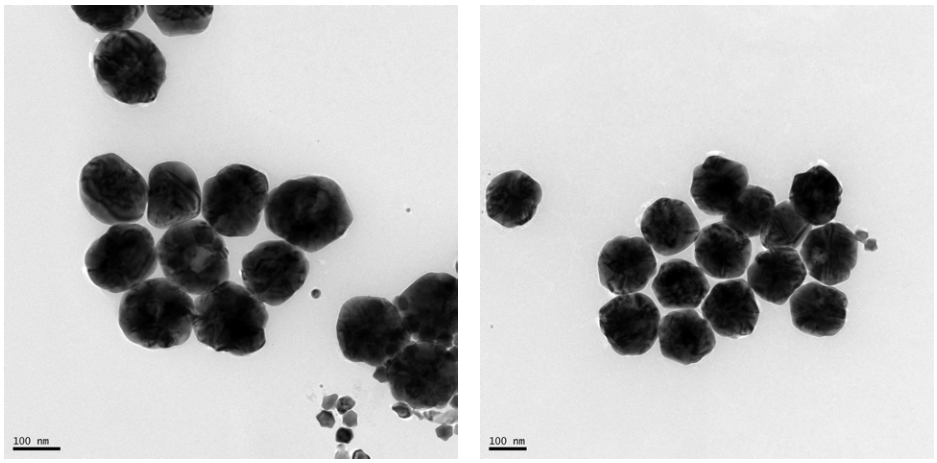

Figure A.13: TEM images of 150 nm Ag nanoparticles. Scale bar in bottom left is 100 nm.

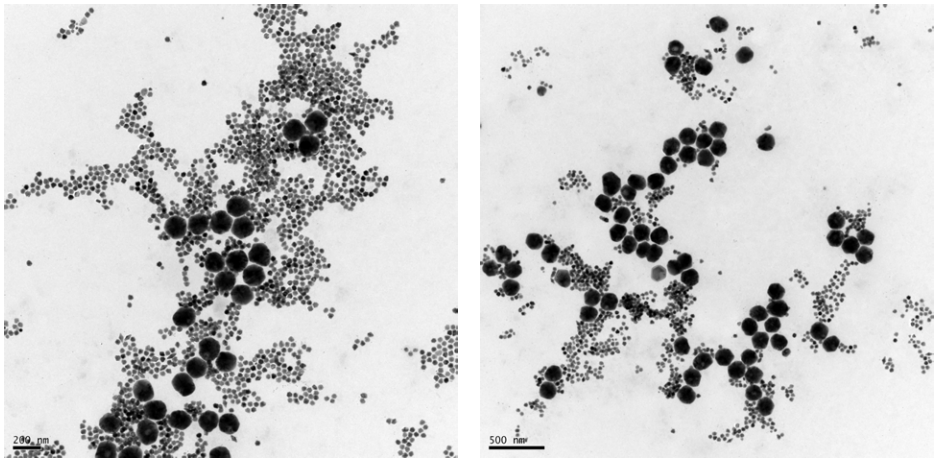

Figure A.14: TEM images of 150 nm Ag nanoparticles. Scale bar in bottom left of the left image is 200 nm. Scale bar in bottom left of the right image is 500 nm.

APPENDIX B

PYTHON FUNCTIONS FOR DATA ANALYSIS

B.1 Linking Rotational Motion of Nanoparticles using Trackpy

```
import string
import scipy
import Tkinter, tkFileDialog
import numpy as np
import pandas as pd
from scipy.spatial.distance import cdist
import matplotlib.pyplot as plt
import os
import sys
import re
import skimage.viewer
from PIL import Image, ImageDraw, ImageColor
import trackpy
import trackpy.predict
import gc
import glob

def trackpy_rot_motion_linker(data_frame, search_range, rot_velocity=0.0,
    memory=0, theta_lim_bias=[0,360], **kwargs):
    '''A wrapper for trackpy linking that includes a predictor for rotating
     particles

    :params data_frame: DataFrame containing all the particle position
    information
    :params search_range: Max distance a particle can move between frames
    :params rot_velocity: The bias (in degrees) that a candidate particle
    should be
    found at. This is positive for positive L's
    :params memory: The number of frames a particle can disappear for and
    still be
    considered the same particle.
    :params theta_lim_bias: The limits in degrees theta to apply the
    rotational bias.
    If a particle is outside this range then no bias is applied.
    :params kwrgs: Additional keyword arguments passed to trackpy.link_df
    '''

    # Find the particle locations in polar coords
    xf, yf, rf = least_sq_fit_circle(data_frame)
    polar_coor_data_frame(data_frame, xf, yf)

    # Generate the predictor function
    @trackpy.predict.predictor
    def predict(t1, particle):
        theta = calc_angle(particle.pos[0], particle.pos[1], xf, yf)
```

```
        r = calc_radius(particle.pos[0], particle.pos[1], xf, yf)
        if theta_lim_bias[0] < theta < theta_lim_bias[1]:
            new_theta = theta + rot_velocity * (t1 - particle.t)
            new_theta %= 360.0
            new_x = calc_x_from_polar(r, new_theta, xf)
            new_y = calc_y_from_polar(r, new_theta, yf)
            return np.array((new_x,new_y))
        else:
            return np.array((particle.pos[0], particle.pos[1]))

    # Track the data and restructure the resulting DataFrame
    trackpy.link_df(data_frame, search_range, memory=memory, pos_columns=['x pos', 'y pos'],
                    retain_index=True, link_strategy='numba', predictor=predict, **kwargs)
    data_frame['track id'] = data_frame['particle']
    del data_frame['particle']
```